Inkjet-Printed Conductive Electrodes: Design, Fabrication, and Characterization

Milad Ghalamboran

A DISSERTATION SUBMITTED TO
THE FACULTY OF GRADUATE STUDIES
IN PARTIAL FULFILLMENT OF THE REQUIREMENTS
FOR THE DEGREE OF
DOCTOR OF PHILOSOPHY

GRADUATE PROGRAM IN
ELECTRICAL ENGINEERING AND COMPUTER SCIENCE

YORK UNIVERSITY

TORONTO, ONTARIO

June 2024

Abstract

Conductive patterns for printed electronics can be printed by adding metal nanoparticles to a solvent with specific agents to improve printability and prevent particle agglomeration. Printed materials require drying to evaporate the solvent and solidify the material. Electrical conductivity is one of the most important properties of printed metal nanoparticle conductors. Conductivity should be the same irrespective of pattern design, size, substrate, location, or density of adjacent patterns. However, we demonstrate here that inconsistencies in the drying process for printed patterns with proximity cause resistivity variations. We studied these resistivity variations experimentally in arrays of printed square electrodes. This variation depends not only on the location of each electrode in an array but also on the number of electrodes. This means that for the same drying temperature and duration, the array with a larger number of electrodes shows higher resistivity variation. After drying, nanoparticles are sintered in a second post-treatment process to improve the electrical conductivity of the printed metal nanoparticle film. In the sintering process, metal nanoparticles melt and merge to form larger grains, so the modified morphology of the printed structure can improve the electrical conductivity. In order to achieve a uniform drying pattern, optimized intense pulsed light (IPL) sintering can be considered as a solution. However, our findings demonstrate that selective CO_2 laser sintering provides better control over patterns according to the pattern density. Additionally, when different materials or patterns are printed on

the same substrate, IPL sintering is not an ideal technique due to the varying parameters required for each material or pattern. Laser sintering, on the other hand, can be programmed to sinter different areas with specific parameters, thereby improving the resolution of the sintering process. Furthermore, frequency domain thermoreflectance (FDTR) measurements allow for local monitoring of the resistivity of complex patterns that cannot be analyzed with a four-point probe. Our study shows that resistivity variation in complex patterns, such as spiral patterns, can be reduced the most with laser sintering. Laser sintering is able to reduce the resistivity variation from 17% observed with thermal sintering and 5.4% with IPL sintering to around 3.2%.

Acknowledgments

I would like to express my truthful gratitude to my supervisor Professor Gerd Grau for his dedication to help me. His advice helped me to pass the obstacles I had confronted and accomplish this part of my life.

I also would like to thank my beloved wife, Parisa, for her continuous encouragement through my whole life. To those who indirectly contributed in this research, your kindness means a lot to me. Thank you very much.

I would like to thank Professors Amir M. Sodagar, Simone Pisana, and Alidad Amirfazli for helping to enhance my thesis with their valuable comments.

Finally, I appreciate my friends', Alireza Dabbaghian, Tayebeh Yousefi, Milad Akbari, Mahdi Nekoui Shahraki, Mohammad Kanan Idris, Paria Naderi, and Saifur encouragement and support during these five years for completing this task.

Contents

Tables

Figures

Chapter 1 Introduction

1.1 Introduction

Circuits and electrical devices may now be printed on a variety of surfaces due to functional inks that were previously limited to pictorial patterns. As a subset of additive manufacturing, printed electronics introduced a new technique for producing various electronic devices, including diodes, capacitors, resistors, and thin-film devices like solar cells, batteries, antennas, transistors and in general wearable applications [1] (shown in Figure 1-1). There are some valuable reasons for applying printing methods, which are the possibility of printing a large area, cost reduction, and rapid manufacturing. Still, another feature of this technique is now being considered as a great potential for the fabrication of wearable and flexible electronics as well, which is the use of biodegradable and recyclable solutions. For example, without the need for etching and masking,

additive manufacturing and printed electronics as a fabrication method reduce the number of materials in a fabrication line. This feature also helps to cut down on fabrication costs [2]–[4].

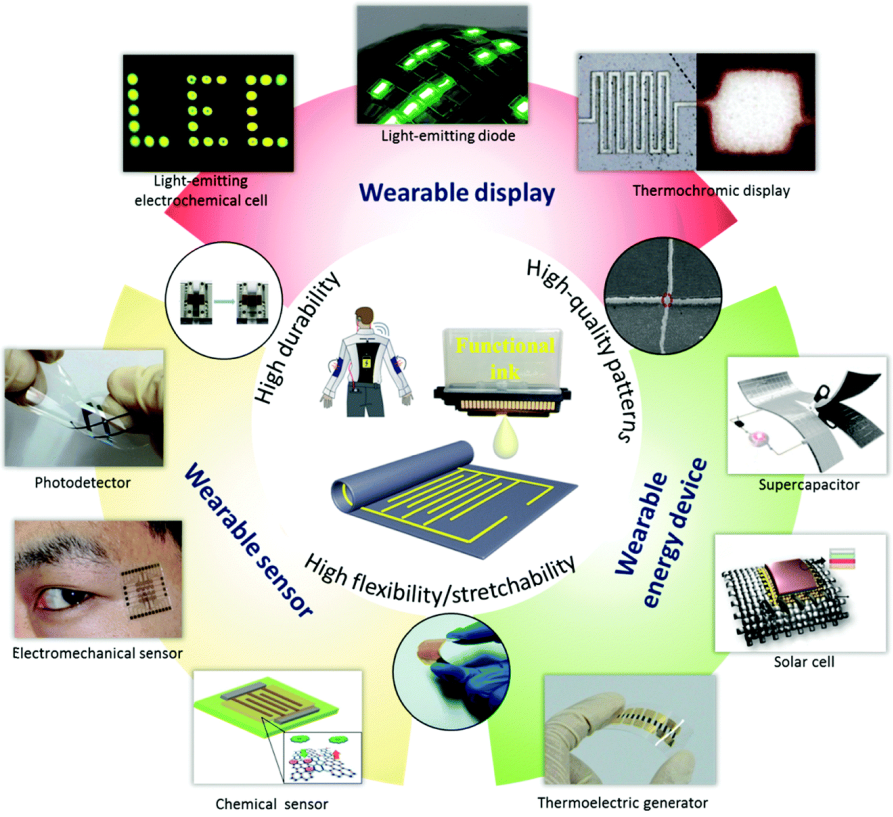

Figure 1-1 Wearable electronics applications using inkjet printing technique [1]

The method of printing conductive patterns near one another on a substrate is critical in the creation of electrical circuits. In a circuit, lines, electrodes, and coils would be printed near together, and they would be expected to have a consistent resistivity in order to be of excellent quality, which includes precise line definition, uniform conductivity, and minimal electrical interference between adjacent components. The printing process can be introduced as a viable option for electrical device manufacturing by controlling factors in printing to achieve a consistent thickness and then resistance.

In the introduction chapter, these topics will be considered:

- Printing
- Drying
- Sintering
- Selective Laser Sintering
- Electrical resistivity measurement

1.2 Printing

Printing techniques traditionally bring to mind visual images or concepts; more recently, 3D and 2D printing techniques have been used in a variety of applications ranging from civil to biomedical engineering. 3D printing uses filaments to create items, but 2D printing uses liquid-

based inks to create patterns on a substrate. The term “printing” in this work refers to any 2D printing technology. The two primary classes in printing procedures are non-contact and contact printing processes. Gravure, offset, flexography, screen, and pad are known as impact, whereas aerosol jet, inkjet, and electrohydrodynamic jet are known as non-impact. In impact printing methods, the design or template should be transferred from a mold to a substrate, while in non-impact methods, the design will be formed on a substrate by droplets by spray or nozzles.

In the realm of printed electronics, various printing techniques are employed, including screen printing [5], [6], gravure printing [7], [8], and flexographic printing [9]. Screen printing is widely used for its ability to deposit thick layers of ink, making it suitable for creating robust, conductive patterns. Gravure printing offers high-speed production and is well-suited for large-scale manufacturing. Flexographic printing, known for its versatility and speed, is commonly used in packaging and label printing [5]. However, each of these techniques has limitations in terms of resolution and the ability to print on delicate substrates. In contrast, inkjet printing stands out due to its non-contact nature, which enables high-resolution patterning on a variety of substrates without physical contact that could damage the material. This precision and versatility make inkjet printing particularly advantageous for producing fine, intricate patterns required in advanced electronic applications. Consequently, this thesis focuses on inkjet printing to leverage its resolution and adaptability for creating high-quality printed electronics [10].

1.2.1 Inkjet Printing

Inkjet printing technology, originating in the 19th century, has evolved from its early scientific foundations to become a prominent printing method in the publishing and graphics industries. Its versatility is valued for producing short runs with variable content, such as expiration dates and customized packaging. More recently, inkjet printing has gained attention as a manufacturing technique for depositing functional materials. Gerard [10] reviewed the development of inkjet technologies, the materials used, and the critical parameters for high-quality printing.

The history of inkjet printing dates back to 1833 when Felix Savart discovered that liquid jets break into repeatable drops governed by fluid dynamics. Subsequent studies by Plateau and Lord Rayleigh expanded on the understanding of jet and droplet formation. The first commercial inkjet device emerged in 1951, integrated into a medical recorder. In 1965, the first continuous inkjet (CIJ) printer was developed, which created uniform droplets for printing but had limitations due to ink degradation from recycling. An alternative, drop-on-demand (DOD) inkjet printing, emerged as a simpler method that generates droplets only when needed, eliminating the complexities of CIJ systems. This technology was initially developed for fax machines but did not reach commercial production [10]. When a computer sends a trigger signal to the thermal or piezoelectric actuator in the nozzle head, droplets are ejected. For the thermal actuator, the signal

heats components that create vapor bubbles, pushing droplets out of the nozzle. In the piezoelectric actuator, the deformation of the piezoelectric element causes the ejection of droplets. In continuous inkjet (CIJ) printing, the piezoelectric actuator sends an acoustic wave to the ink inside the nozzle, forming distinct droplets. These droplets are then directed to a substrate, while unwanted droplets are captured in a gutter a they pass through an electric field between two parallel poles [11]. These three types of inkjet printings are shown in Figure 1-2.

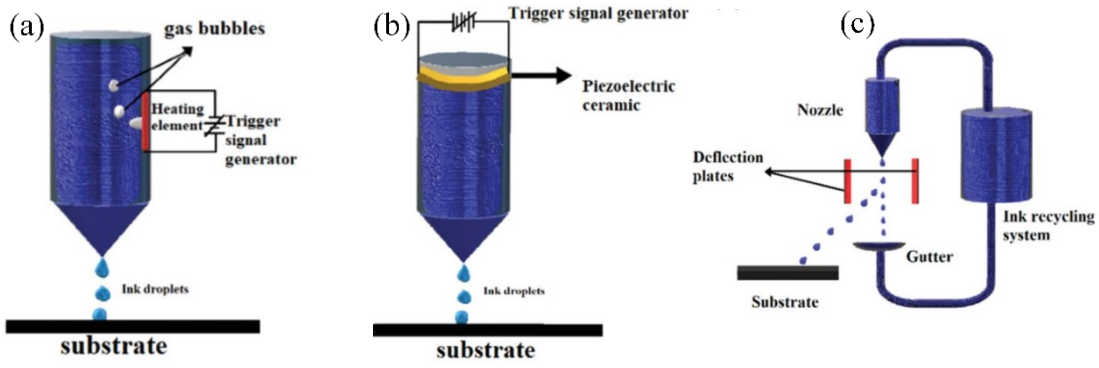

Figure 1-2 Types of inkjet printings a) thermal DOD, b) piezoelectric DOD, and c) CIJ [11]

Before selecting an ink for a reliable printing pattern, it is crucial to consider certain ink parameters that ensure the formation of stable droplets ejected from the nozzle. A well-defined jetting process should produce distinct droplets without long tails or satellite droplets, ensuring a consistent and accurate pattern. There are three dimensionless numbers, which can play an essential role regarding the ink's stability, Reynolds number (Re) (1.1) [12], Weber number (We) (1.2) [13], and Ohnesorge number (Oh) (1.3) [14]:

$$Re = \frac{\upsilon \rho \alpha}{\eta} \tag{1.1}$$

$$We = \frac{\upsilon^2 \rho d}{\gamma} \tag{1.2}$$

$$Oh = \frac{\sqrt{We}}{Re} = \frac{\eta}{\sqrt{\gamma \rho d}} \tag{1.3}$$

Where υ, α, ρ, η, and γ denote the velocity, drop diameter, density, viscosity and surface tension of the ink, respectively. We is known as a balance between the inertial force and surface tension, Re is the ratio of the inertial force to the viscous force, so it can be concluded that Oh number is related to the viscous force to the inertial force and surface tension. Printability of inks for drop-on-demand jets is studied numerically by Fromm [15], and characterized as Z number, which is Z = 1/Oh.

The Z number is a dimensionless parameter used in fluid dynamics to describe the printability of inks in inkjet printing. The Z number is influenced by several key parameters related to the fluid dynamics of the ink. These parameters include the viscosity (η) of the ink, where higher viscosity increases the Oh number and thus decreases the Z number. The surface tension (σ) of the ink also plays a critical role; higher surface tension decreases the Oh number, thereby increasing the Z number. Additionally, the density (ρ) of the ink affects both inertial and viscous forces, impacting the Oh number and subsequently the Z number. The characteristic length (l), such as the droplet diameter, is another crucial factor, as it is used in calculating the Reynolds number and Weber number, which are components of the Ohnesorge number. Finally, the velocity (v) of the ink ejected from the nozzle influences the Reynolds number, which is part of the Ohnesorge number calculation. Achieving an optimal Z number, typically between 1 and 10, is essential for stable and high-quality printing, as it affects the formation of satellite droplets and the overall printability of the ink.[16]. Another range is represented by Jang et al [17], after studying drop formation at the inkjet head, which is between 4 and 14, the ranges indicate the ideal conditions for achieving stable droplet formation, ensuring that the ink can be ejected smoothly without creating unwanted satellite droplets.

Drop spacing can be dependent on the speed of the nozzle movement and the frequency of ejection or different coordinates of droplets with a constant speed of nozzle. According to Figure

1-3, when droplet spacing reduces, the behavior of the lines may be classified as individual drops as well as scalloped, uniform, and bulging, as well as stacked coins. In certain cases, uneven wires might result in a portion of the cross-sectional area that is too tiny, causing a spike in sheet resistance to occur [18]–[20]. So, printing as the first step of device fabrication should result in high-quality patterns with uniform features such as thickness and width, and length in a line printing as an instance. After designing and printing the patterns, it is time to dry the printed ink on a substrate.

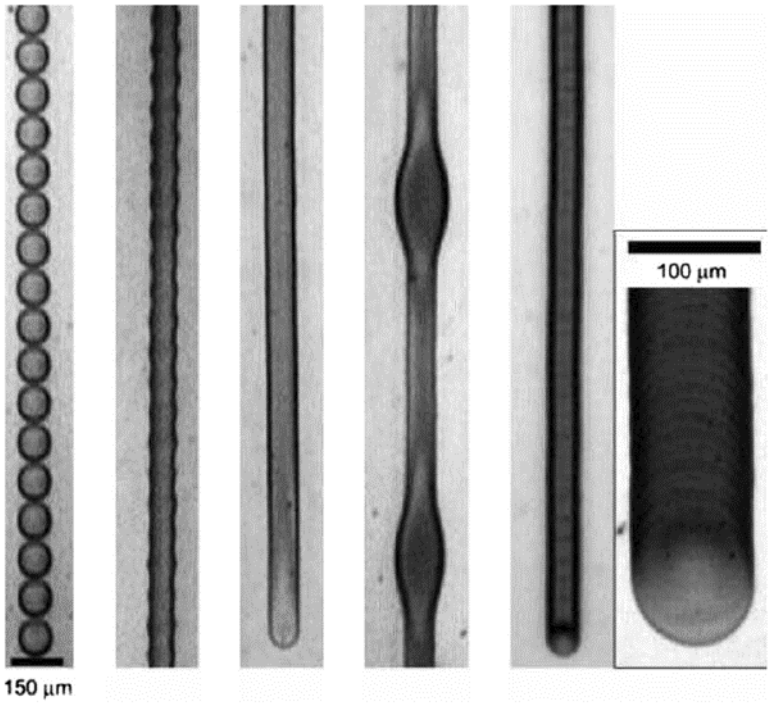

Figure 1-3 Printed line behaviors as a result of drop spacing decreasing from left to right [19].

Since a high resolution and consistent design enhances the uniformity of electrical characteristics, such as resistivity, as well as enables it to be created in less area, an outstanding pattern is necessary for device building. There are tens to hundreds of micrometers in feature size, and the thickness ranges from a few nanometers to several nanometers. The circuit pattern's resistance will be affected by the film's form at the macroscopic level. There are several variables that influence the printed line patterns, including the substrate's surface energy, the evaporation environment, the printing parameters, and others. Experts devote a lot of time and attention to their

research in order to reduce the number of surface flaws. The kinetic energy of a droplet is transformed into surface energy when it is sprayed onto a surface. Surface tension causes the droplets to compress and shake as they spread out over the substrate, releasing any surplus kinetic energy. The substrate on the bed of the inkjet printer goes back or forward while the nozzle is jetting the droplets, so the drops will join based on the drop spacing defined for the bed movement; a line will form on the substrate [18].

1.3 Printed Electronics Inks

Based on the function of an electronic structure, conductive, semiconductor, and dielectric inks may be printed on a suitable substrate. Several inks need to be printed and layered in various structures; in this situation, inks should be compatible with generating a homogenous layer. In general, inks are divided into two categories depending on their solute, which serve as the principal platform: organic and inorganic inks. Organic and inorganic inks play crucial roles in the development of printed electronics, each offering distinct advantages for various applications. Organic inks, often composed of conductive polymers such as poly(3,4-ethylenedioxythiophene) (PEDOT) or small molecules like tetrathiafulvalene (TTF), are prized for their flexibility, low-temperature processing, and compatibility with a variety of substrates, making them ideal for flexible displays, wearable electronics, and organic photovoltaics. In contrast, inorganic inks,

typically containing metal nanoparticles (e.g., silver, copper) or metal oxides, provide superior electrical conductivity and stability, which are essential for applications requiring high-performance interconnects, antennas for RFID tags, and printed circuit boards. Recent advancements have seen hybrid approaches, combining the flexibility of organic materials with the conductivity of inorganic components, to enhance the performance and expand the potential applications of printed electronic devices [21]–[23].

1.3.1 Conductor Inks

Conductor inks are the most often used inks for use as connectors in printed electronics, particularly in wearable electronics [24]–[26]. Furthermore, certain conducting materials, such as silver as a metal and carbon nanotube (CNT) as a carbon-based material, are employed as inks for inkjet printing. The essential qualities of metal nanoparticles or precursors ink are electrical conductivity and stability. Gold (Au) is recognized as the highest-ranking in terms of environmental stability among metal inks. However, it is not frequently used economically, while silver (Ag) offers almost the same qualities at a lower cost [1]. Metal nanoparticles or precursors may be dispersed in water or organic solvents, and various stabilizers are added to the inks to ensure proper stability and prevent agglomeration or condensation. Post-treatment, drying, and sintering are the following steps in employing such inks to create electrical conductivity. To get

the printed ink's electrical conductivity closer to bulk's electrical conductivity, these procedures are followed.

1.4 Inkjet Printing Method

The nozzle, ink reservoir, pressure pump and controller valve, computer interface, and camera are all components of an inkjet printing system. A glass tube with an aperture is inserted in a metal housing with a fluid fitting at the end, and a tube will link it to the filtered ink reservoir. Filtered ink can prevent nozzle obstruction caused by the aggregation of nanoparticles. Actuators can be controlled by heat or piezoelectric component inside the nozzle. Because a thermal actuator can evaporate the ink's solvent and clog the nozzle, a piezoelectric actuator is used in this system. A piezoelectric actuator is installed on the glass tube with two inner and outer electrodes powered by

two wires linked to the electrodes. A pressure valve pushes the ink through the tube to the nozzle, which controls the pressure. A schematic of the inkjet printing system is depicted in Figure 1-4.

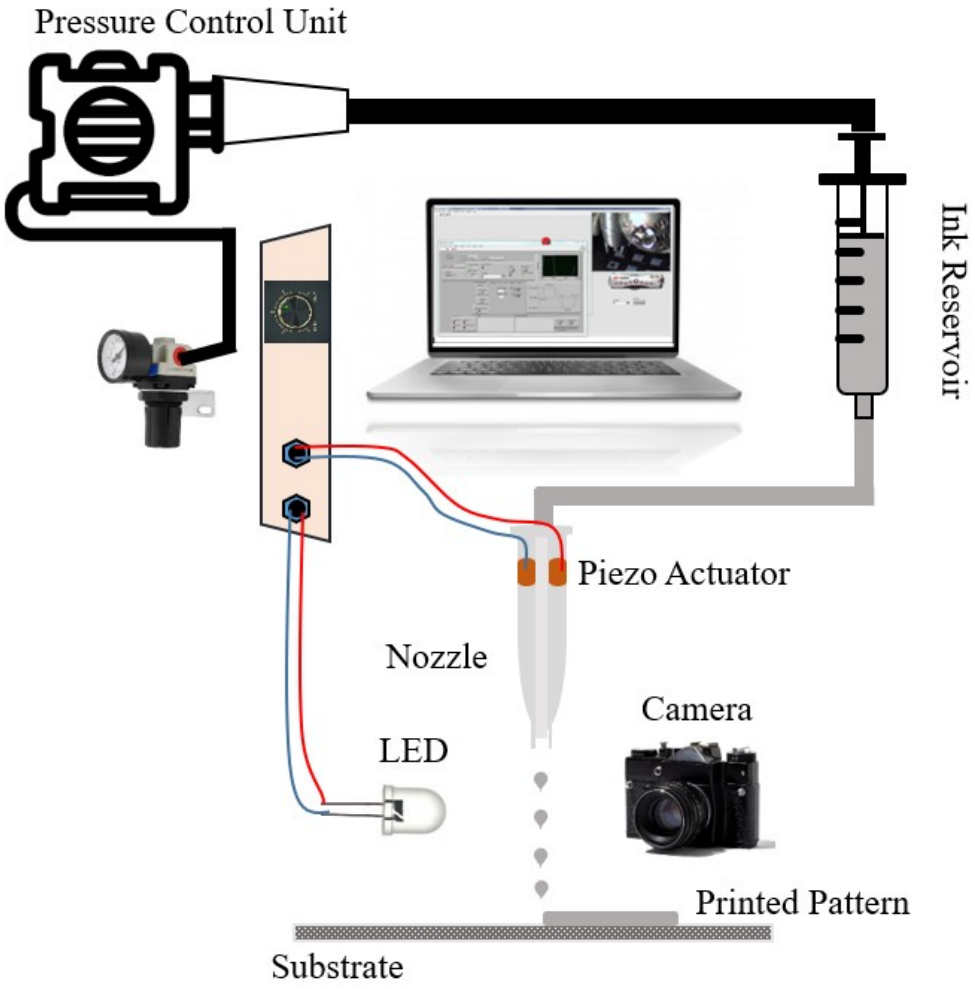

Figure 1-4 Inkjet printing setup

A piezoelectric actuator will provide positive and negative pressure to the ink within the glass tube. Depending on the voltage polarity, piezoelectric material can expand radially or axially. A signal will be applied to the actuator, and deformation will occur during the rise and fall times before terminating during the dwell period, when the voltage is constant. For controlling the ink flow, the trapezoidal waveform may be bipolar. A signal is shown in Figure 1-5.

Inkjet printing is a prominent technique in the fabrication of printed electronics due to its high precision and adaptability. Commercial inkjet technologies typically utilize nozzles with diameters ranging from 10 to 50 micrometers, enabling the deposition of fine lines and patterns. The jetting frequencies of these systems can vary widely depending on the specific application and printer model but generally up to ~10 kHz, allowing for rapid and efficient printing processes. Zhou et al. (2015) explored the potential of significantly enhancing the productivity of inkjet printing for printed electronics by employing jetting frequencies in the megahertz range. Their study demonstrated that by increasing the jetting frequency to this level, the productivity of the printing process could be boosted by approximately 100 times compared to traditional methods operating at kilohertz frequencies [27], [28].

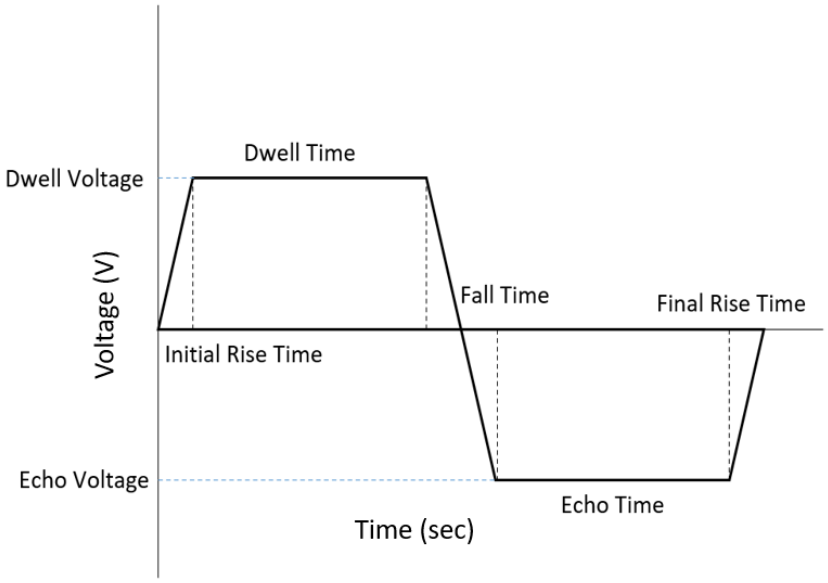

Figure 1-5 A bipolar actuating signal for controlling the jetting stability of an ink used in the inkjet printing system

A suitable rise time, fall time, dwell time, and echo time will ensure that droplets may be ejected from the orifice after finding a proper ink with particular characteristics, which will be detailed in printed materials. In order to print a design, a Cartesian code is written in a text file, and continuous jetting (Figure 1-6) is used to discover the necessary time parameters.

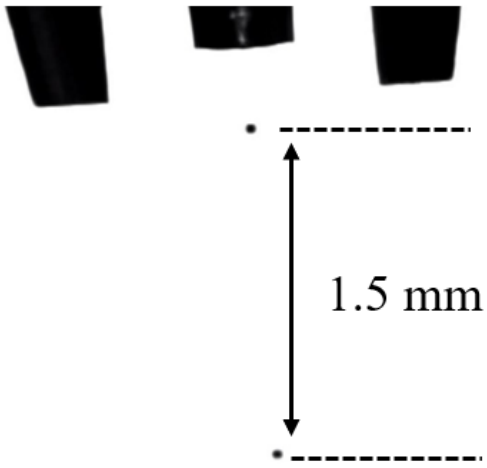

Figure 1-6 Stable jetting of a 60μm-diameter nozzle

1.5 Drying Process

The process of droplet evaporation on a surface is complex, influenced by factors like the Marangoni effect and the transfer of mass and heat. This process has wide-ranging applications in fields such as spray drying, DNA mapping [29], [30], and inkjet printing [31], [32]. In the transformation from fluid ink to a solid film on a substrate, ink undergoes multiple physical and chemical transitions. The drying process, which solidifies the ink, is a crucial step in this

transformation. The choice of drying technique is influenced by the specific properties of the ink's chemical composition and the substrate's characteristics. Given the printing industry's evolution, driven by environmental, health, and technological considerations, there has been a significant shift towards more sustainable drying processes.In recent years, to address concerns of energy consumption, cost, and environmental impact, alternatives such as UV curing and microwave drying have gained popularity over traditional thermal drying methods. While these modern techniques offer benefits, such as reduced energy usage and faster processing times, they also come with their own set of drawbacks. For instance, UV curing may not be suitable for all types of inks and substrates due to compatibility issues, and microwave drying can be limited by the uneven heating of inks containing different materials.

The advantages and disadvantages of these drying processes must be carefully weighed, particularly in terms of their operational efficiency, compatibility with various inks and substrates, and environmental footprint. [33].

1.5.1 Absorbtive Drying

There are some additives in the ink, which can be absorbed by the substrate depending on the porosity of the substrate, mainly the solvent would be absorbed but there are colorant, resin and binders mixed in the solvent that should be removed in electronic applications. Absorption refers

to the interaction between the ink and the printing substrate. In absorption drying methods, some parameters can change the drying speed, which are ink's carrier viscosity, binder, and substrate characteristics [33].

Paper, especially with a high ink-absorption capacity, can be applied for printed electronics due to the speed of drying , foldability, breathability and biodegradability [34]. The absorption strength of the ink has a significant influence on the printing color and glossiness of the printed information. If the paper's absorption of ink is too quick, the ink's penetratration will infiltrate the paper too deeply, leading to dull-looking printing output. Otherwise, inadequate ink-to-paper absorption would decrease the printing process's drying pace, which is not suitable for a production line. As the paper is known as a porous substrate, the ability of printing sheets to absorb ink is an essential quality indication [33], [35].

1.5.2 Evaporative Drying

When the ink is printed, solvents detach quickly from the ink and vaporize away. When the liquid phase evaporates, the remaining ink components are brought closer together, resulting in a single film. Consequently, the dried ink layer adheres to the print substrate. However, the first disadvantage of this approach is evaporation time; for example, when utilizing evaporation methods to dry water-based inks, evaporation speed will decrease compared to microwave drying

method. Furthermore, high temperatures may cause the substrate to change color or distort, while plastic substrates need moderate temperatures, lengthening the process [33].

1.5.2.1 Radiative Drying

Radiant heating is used in infrared (IR) drying, is a method that dries materials using IR radiation without the need for direct contact or mechanical impacts such as high-speed hot-air jets. Large quantities of energy may be transferred quickly using IR light. The wet ink film is heated directly with the energy generated by IR light. The ink coating absorbs enough IR light energy in this arrangement to create heat energy. When subjected to high temperatures, all of these processes speed up. It is possible to dry deposited layers in minutes using IR technology. Reduced system cost (around 1:10) and lower operating expenses over intense pulsed light (IPL) are the key advantages of this approach. Other advantages include a simple and resilient setup, simple resizing (e.g., large area emission), and high compatibility with layer stack processing. The IR method, like the IPL approach, may be used to treat temperature-sensitive polymer substrates since it is a selective technique. A rise in temperature is caused by the activation of molecular bonds by IR irradiation. Drying was also employed in roll-to-roll (R2R) printing with IR technology (shown in Figure 1-7). When it comes to R2R processes, IR is also used for sintering, such as the sintering of TiO_2 on metal surfaces [4]. The difference between the drying and sintering stages when using

an IR system depends on the time and energy applied. In the drying stage, which requires a shorter duration and lower energy, we aim to evaporate the solvent and solidify the ink. In contrast, the sintering stage involves a longer duration and higher energy to fuse the nanoparticles and enhance the conductivity of the printed material. After drying, the solid part needs to be characterized electrically or thermally.

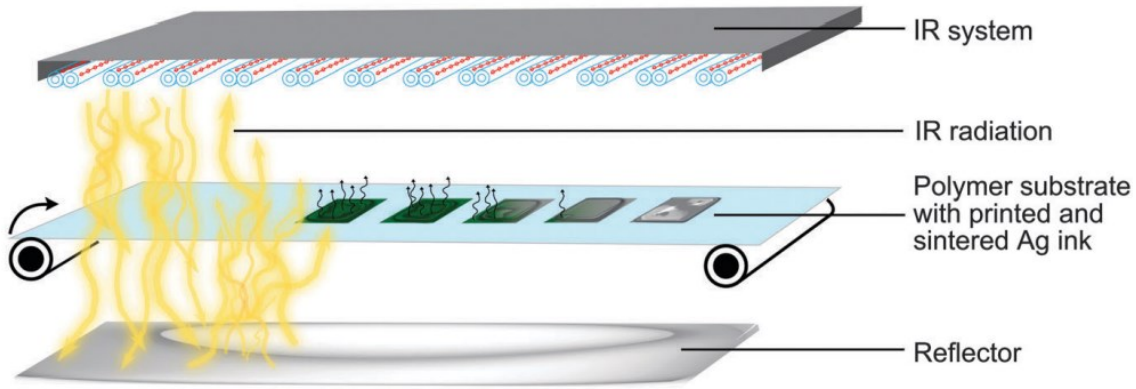

Figure 1-7 R2R drying schematic using IR radiation [4]

1.6 Drying Challenges

As the ink begins to dry, the viscosity will increase, decreasing the evaporation speed. In addition, the ligands and binders that encapsulate the nanoparticles to suspend them in solution limit the electrical conductivity of the printed thin-film pattern. These components should be

decomposed during the sintering process. This process not only deteriorates the organic components but also fuses the nanoparticles, improving the printed pattern's electrical conductivity. Achieving uniform evaporation in inkjet-printed electronics poses challenges, including the coffee-ring effect leading to non-uniform thickness [36], [37]. Researchers investigate the evaporation kinematics of a single drop on a smooth surface. The important parameters, which are base radius, contact angle, and height, are calculated experimentally and theoretically; the results show that their responses are extremely nonlinear. Induced flows in solution droplets containing suspended particles or colloidal polymers are a result of non-uniform evaporation (at the same time) [41].

Evaporative flux J(r) (1.4) is introduced by Deegan,

$$J(r) \propto \frac{1}{(R-r)^{1/2}} \tag{1.4}$$

In the coffee-ring effect observed during evaporation in a droplet with a fixed contact line, the radius of the droplet's base is denoted as R, and the radial distance from the center is r. This phenomenon is characterized by a radial liquid flow that moves toward the droplet's periphery, causing particles within the droplet to be transported by capillary flow to the edge, resulting in a ring-like deposit of particles at the boundary. [38]. The coffee-ring effect, shown in Figure 1-8,

caused a concave shape where the edges are three times thicker than the center. Uniform droplet deposit is required in many applications, especially in electronic fabrication. When it comes to final deposit formation during evaporation, some treatments are required to regulate the final deposit form to overcome the boundary restrictions due to the pinning and depinning of the deposited drops [39]–[43].

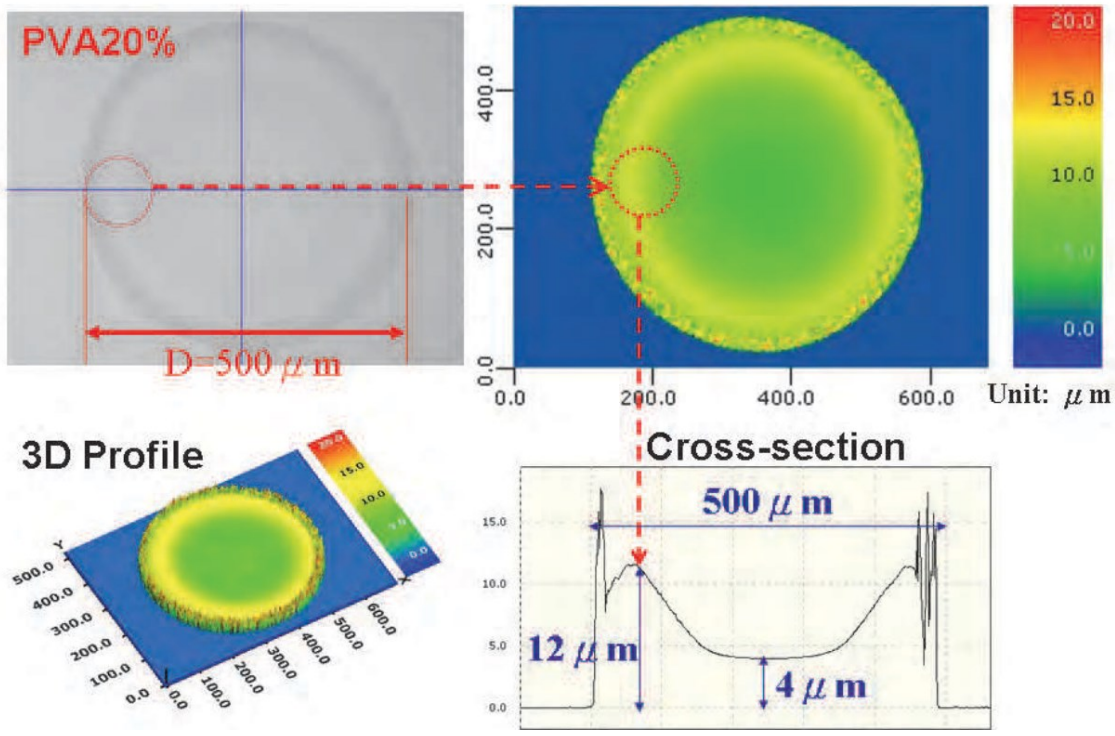

Figure 1-8 Coffee ring effect of an aqueous PVA 20% droplet [38].

Jung's research [44] reveals the influence of variations in ink solvents on the layer thickness variations of dried inkjet-printed layers on non-porous substrates. Layers printed on substrates like standard glass often exhibit non-uniform thickness, commonly attributed to the coffee-ring effect, where the thickness at the edges can be up to four times higher than at the center due to extended evaporation rates at the edges [45]–[47]. Another observed deviation is particle agglomeration in

the center, linked to Marangoni Convection driven by thermal gradients. Both deviations are prevalent in functional printing applications using low-viscosity inks with a high solvent content, potentially leading to issues in subsequent processes. The primary goal of Jung's research is to identify a parameter for controlling the uniformity of such printed structures, focusing on understanding the influence of solvents, evaporation, and drying conditions. Model inks composed of ethylene glycol (EG), 1-butanol, and the colorant solvent black 29 are printed on glass substrates (shown in Figure 1-9), and the drying mechanism is observed using a confocal microscope. The study investigates the impact of solvent composition on final film uniformity, revealing insights into the drying process and introducing a measure called three-phase contact line movement [48] to quantify pinning or unpinning. The results, based on 3D images, indicate that the ratio of solvents significantly affects layer thickness uniformity, with the Coffee-Stain Effect observable in both pinned and unpinned contact line movement, while Marangoni Convection has a lesser impact [49].

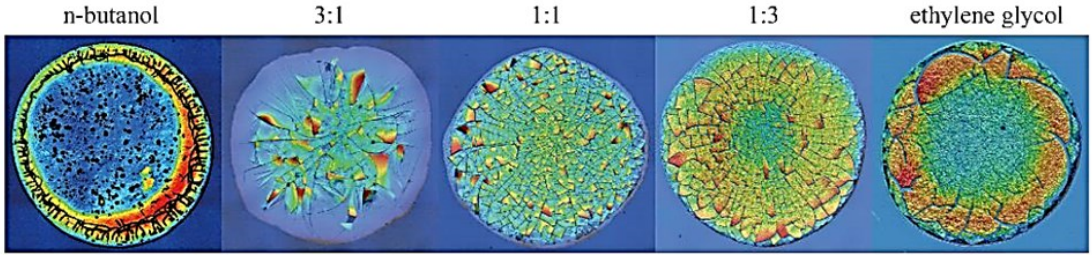

Figure 1-9 Examination of height profiles on glass resulting from varying mixtures of 1µl butanol and ethylene

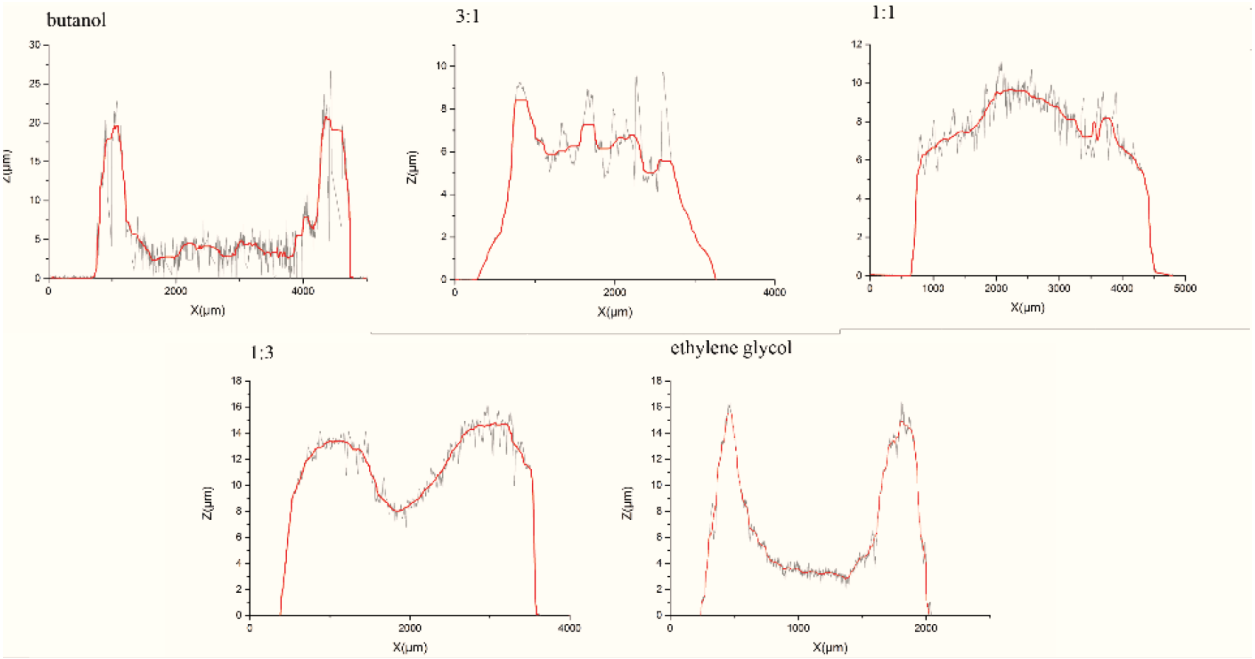

glycol. The Coffee-Stain Effect is evident in the 1:3 ratio of 1-butanol to ethylene glycol, while aggregation occurs at the center in the 3:1 ratio. A uniform profile is achieved in the 1:1 ratio [49].

The substrate can be sensitive to the drying temperature; for example, polymer-based substrates such as polyethylene terephthalate (PET) cannot be placed on a hot plate with a temperature beyond 150 °C; in this case, short-wave or medium-wave IR technology would be a better approach for drying printed inks as the substrate does not absorb the IR irradiation. It is a fast-drying method that can increase the temperature of the ink by vibration excitation of the molecular bonds [50]. This method is applied to silver nanoparticles printed on glass and paper substrates. IR drying can be used to control the sintering time and substrate's temperature; it shows that the IR method dries the ink for 3 min, resulting in the same resistance (3.8 μΩ.m) after sintering compared to the conventional drying with a longer time (5 min, 200 °C) [51]. In most the studies, IR is applied for roll to roll (R2R) printing, where the intensity of irradiation, exposure time, the distance between the printed patterns and the emitters, and the speed of roll movement under the IR can be considered as the parameters of IR drying [50].

Lopes et al. [52] indicates that the properties of the substrate, including its thermal conductivity, can greatly affect the rate of evaporation. Furthermore, three distinct evaporation modes for sessile drops have been identified [53]–[55], each with unique characteristics regarding the contact angle and line, which are constant contact line mode, constant contact angle mode and stick-slip mode (which is more common for liquids with the presence of nanoparticles [43]–[45]). Simulating the evaporation of droplets numerically is challenging due to the interaction between heat and mass

transfer processes and the changing free surface. Therefore, a deep understanding of droplet evaporation is essential for tackling issues related to non-uniform drying and other relevant applications.

Non-uniform drying can be an important issue in printed electronics, which is not studied yet, the drying pattern can be seen in printed electronics with important consequences, as demonstrated in this thesis. In research work, the behavior of a single water droplet and multiple droplets deposited alongside, on a substrate with the same condition is studied and revealed that the single drop evaporates faster than the center drop surrounded by six drops which show there is an interaction between drops (shown in Figure 1-10). As the drops around the central drop start to evaporate, the relative humidity of the air around the central drop will increase and reduce the evaporation of the center drop. It is calculated experimentally that the lifetime of the center drop is 51% longer than the single drop due to the explained interaction [59]. Therefore, the only concern in the literature for the drying step of printed patterns is considered the coffee-ring effect. In terms of drying patterns and their effect on resistivity, there is no study. After drying, metal nanoparticles should be in contact with each other, and the boundaries should decrease to improve the electrical conductivity; this process will be explained in the sintering section.

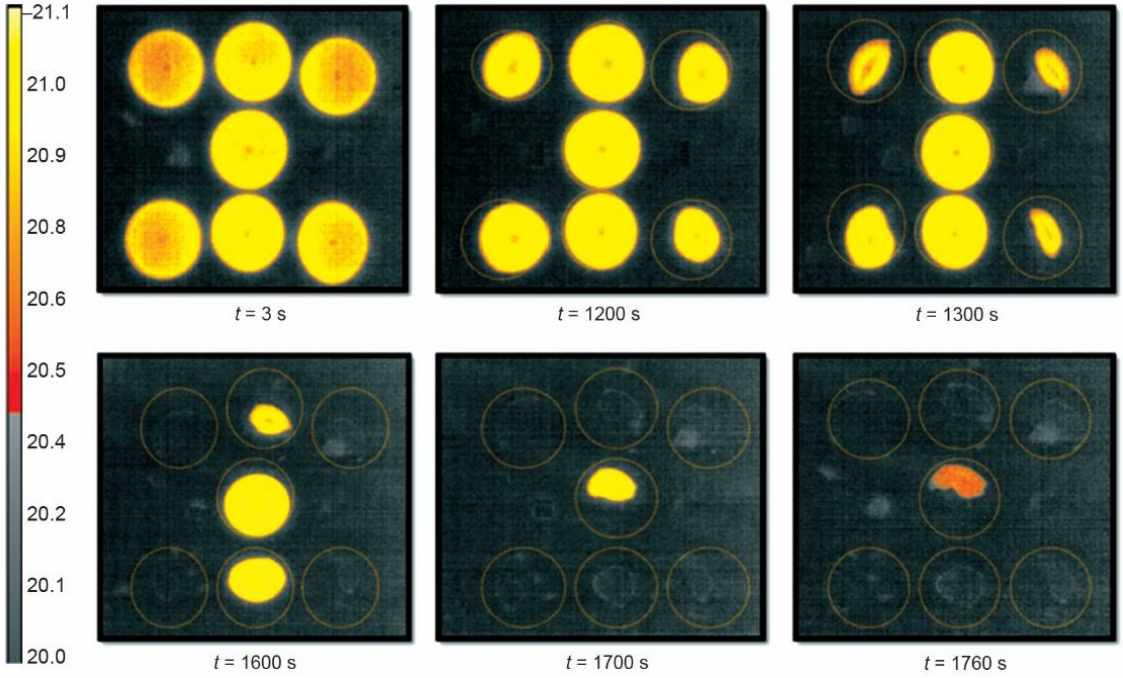

Figure 1-10 IR images of seven water droplets evaporation over time on a substrate at room temperature (21 °C) and humidity of 50% [59].

1.7 Sintering Process

After the ink layer has been successfully deposited onto the substrate, the solvent's evaporation is required to solidify the printed pattern; however, the pattern is not conductive due to the organic components such as stabilizing agents (added to the ink for metal nanoparticles aggregation prevention) and other nonvolatile agents, which are similar to a barrier between nanoparticles to be connected to each other. Sintering is a process of decomposing the organic components and merging the nanoparticles under their melting points to improve the electrical conductivity of the whole printed pattern; in addition, the sintering process can improve the adhesion of the printed pattern to the substrate [50], [51]. Yung studied the effect of a camera flash on sintering of silver nanoparticle inks on different substrates.

Printed electronics play an important role in developing flexible and wearable devices due to their compatibility with various substrates and cost-effective manufacturing processes. One critical aspect that influences the performance of printed electronic components is the resistivity of the printed structures. Low and uniform resistivity is essential to ensure reliable and efficient operation of devices such as sensors, antennas, and circuits. Variations in resistivity can lead to significant performance degradation, including increased energy losses and reduced efficiency. For instance, in flexible RF systems, the quality factor (Q-factor) of printed coils is highly sensitive to resistivity

variations, impacting overall system performance. Additionally, consistent resistivity is crucial for the reliability of printed devices, as variations can cause uneven electrical properties, leading to performance issues. Optimizing sintering processes can achieve lower resistivity in printed conductors [60], [61].

1.7.1 Thermal Sintering

There are some sintering techniques for improving the electrical conductivity of metal nanoparticles, the most frequent of which is thermal sintering, carried out with the help of a hot plate and for some specific materials in the reducing atmosphere [53]–[56]. Metal nanoparticle synthesis is usually halted before reaching a critical radius by introducing an organic stabilizer to the mixture. These stabilizers permeate the colloid and bind to the nanoparticle surfaces, preventing further absorption of metal ions. There are two main reasons for keeping the nanoparticles small. Firstly, to avoid blockages in the print nozzle and enhance print quality, the nanoparticle size must be under 50 nm [62], [63]. Secondly, nanoparticles have a high surface-to-volume ratio, and the self-diffusion of metal nanoparticles is more than the bulk metal, which causes a lower melting point for metal nanoparticles. This results in a reduced sintering temperature needed for the nanoparticles to form a continuous, densified structure post-printing [64]. Electrical conductivity reduction and oxidation of metal nanoparticles can be the results of

the prolonged exposure to air and the high temperatures used in the typical thermal sintering method, which would be a motivation for using other sintering methods.

1.7.2 Intense Pulsed Light (IPL) Sintering

IPL sintering is one of the most attractive methods for sintering metal nanoparticles. When Kinney and colleagues published their historical patent in 1969, they started to use the IPL technique for sintering nanoparticles, and it now is applied to printed materials for electronic devices [57]. The invention provides the possibility of sintering nanoparticles on a sensitive substrate to the temperature, which can be achieved by using a xenon lamp. It is feasible to do so without causing harm to the heat-sensitive polymer. For the first time in history, IPL irradiation was used to treat a substrate [58]. Low-temperature IPL irradiation was used to create patterns on polymer substrates. Schroder and colleagues published their findings in 2006. The first IPL sintering machine of the research type was marketed in order to sinter metal nanoparticles, according to their conference paper. Following the publication of these earlier findings, several investigations on IPL were conducted. Substantial research was carried out using newly built IPL equipment and processes [58]–[63]. In one study [65], inkjet printing of silver nanoparticle inks with four distinct properties on a polymer-based substrate was investigated, followed by the application of three different sintering techniques: oven sintering at 150 °C, IR sintering for 15

minutes, and varying parameters of IPL sintering. The surfaces were optically observed both as printed and after sintering, revealing a variety of structures due to the different sintering methods and conditions. For example, in Figure 1-11 (a, b, and c), the surfaces appear smooth, but bulging occurs at the edges.

Inks with a high carbon content (shown in Table 1-1), which are nonpolar and oil-based, tend to have a slower evaporation rate during sintering due to their higher boiling points. As a result, it is often challenging to completely eliminate all hydrocarbons from these inks. In contrast, inks based on polar solvents like ether and alcohol can be sintered at lower temperatures due to their lower boiling points. One ink, for instance, formed an inhomogeneous surface with a coffee ring after drying, which indicates a larger nanoparticle size compared to other inks (shown in Figure 1-11 (d, e, and f)). Another ink formed a dark layer due to higher surface roughness but resulted in smooth layers as shown in Figure 1-11 (g, h, and i). Both oven and IR sintering yielded similar results, while IPL sintering caused some burning. The quality of the patterns, which is crucial for electronic device fabrication, can be affected by the type of sintering method. An examination of sheet resistance revealed significant differences between the various inks and sintering techniques. Additionally, the work function (WF) was measured and found to depend on both the sintering technique and the type of silver ink. UV sintering, for instance, provided comparable WF values

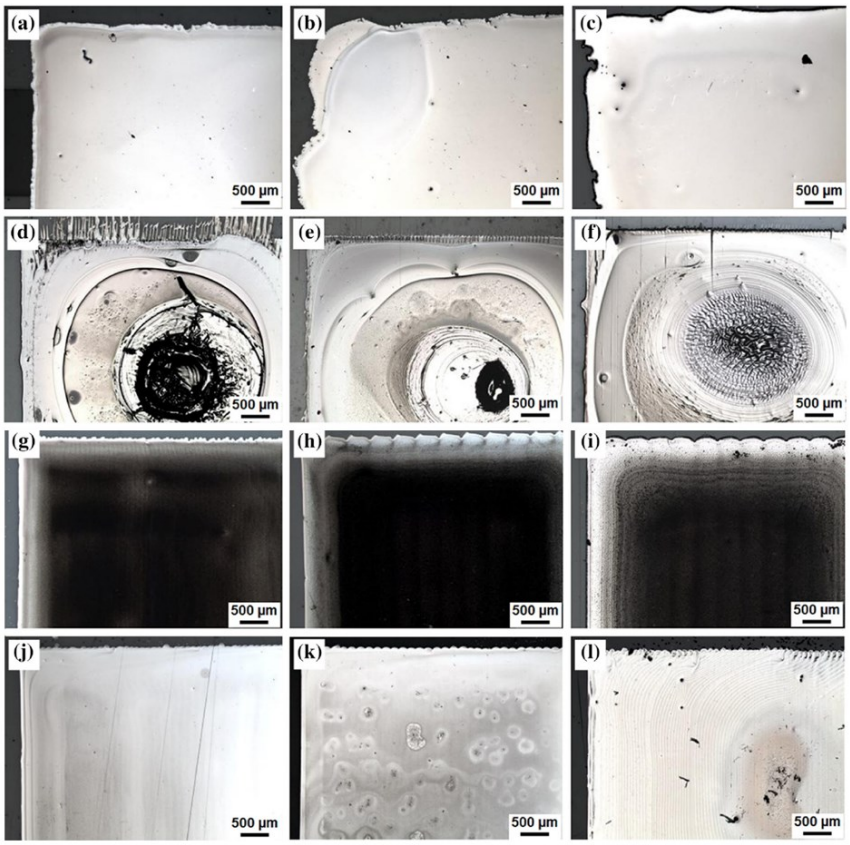

Figure 1-11 Images taken under a microscope of several silver inks that have been processed with various sintering procedure, (a)-(c) nonpolar ink at 150 °C; IR 15 min; IPL 0.82 J/cm2; (d)-(f) nonpolar ink at 150 °C; IR 15 min; IPL 0.955 J/cm2; (g)-(i) polar ink at 150 °C; IR 15 min; IPL 0.955 J/cm2; (j)-(l) polar ink at 150 °C; IR 15 min; IPL 1.096 J/cm2[65].

ranging from 3.7 to 4.3 eV, close to the bulk value of silver. It was also noted that different WF values were achieved for the same silver ink when using different sintering procedures.

Table 1-1 Examples of silver nanoparticle inks [65]

Company	Product name	Main solvents	Particles size (nm)
UT Dots, Inc.	UTDAgIJ1 (nonpolar)	Organic solvents (trade secret)	~ 10
Xerox	XCM-NS32 (nonpolar)	Decahydronaphthalene + hydrocarbons	< 12
PV Nano Cell Ltd.	Sicrys I30EG-1 (polar)	Ethylene glycol	70-115
ANP Co. Ltd	DGP-40LT-15C (polar)	Triethylene glycol monoethyl ether	<50

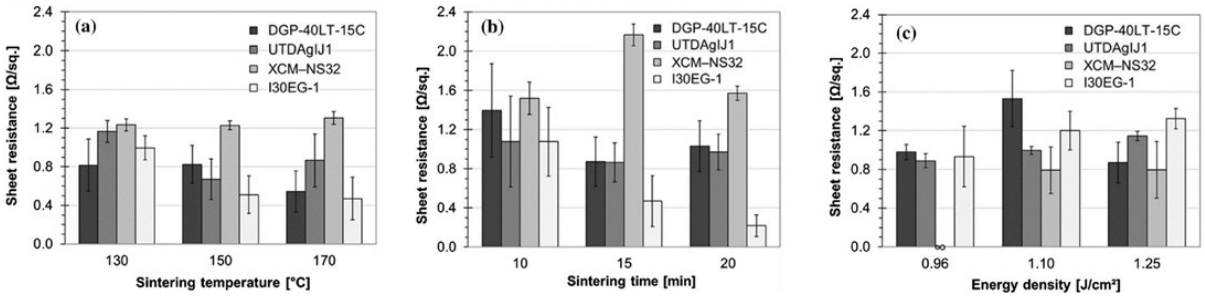

Figure 1-12 Graphs illustrating the relationship between the sheet resistance of the four silver inks and the sintering temperature [65].

In exploring alternative sintering processes, research has demonstrated the efficacy of IPL sintering for metal nanoparticles, particularly silver. Kang et al. (2011) employed IPL to sinter silver nanoparticle inks, achieving an increase in particle size and a reduction in resistivity to 4.9

± 0.3 μΩ.cm [64]. This process allowed for rapid heating of printed patterns to 500 °C using an energy density of 50 J/cm². Niittynen et al. further investigated IPL sintering alongside plasma and laser sintering, finding that IPL sintering outperformed other techniques in terms of mechanical performance and electrical conductivity [66]. They reported that the resistivity of silver nanoparticles after IPL sintering was nine times greater than that of thermally sintered films in under five seconds, compared to thermal sintering for six hours at 130 °C [67].

Chung et al. studied the IPL sintering of metal nanoparticles on flexible substrates with in-situ monitoring and observed that electrical conductivity improvement ceased after four pulses. The resulting sheet resistance of IPL-sintered silver nanoparticles was 0.95 Ω/sq, twice as effective as thermal sintering, without damaging the PET substrate due to the short sintering period [68].

However, a challenge arises when considering the sintering of various printed patterns and shapes necessary for different electronic devices. Kim et al. found that sintering characteristics depend on the printed shapes and patterns, leading to potential issues with resistance homogeneity when using multi-size patterns [68]. This indicates that while IPL sintering offers significant advantages, its application must be carefully considered in the context of the specific requirements of electronic device fabrication. In their work, finite element simulation of Cu patterns in terms of heat transfer is considered for studying the cause of the varied sintering processes depending on

the pattern dimensions. A similar energy density of IPL is applied in the simulation. As seen in Figure 1-13(a), temperatures rose fast for 5 J/cm^2 energy density. When the spacing between the Cu patterns was broader than 200 µm there were no discernible variations in the highest temperature observed. In contrast, it was discovered that decreasing the gap between the Cu patterns from 200 to 50 µm resulted in a rise in the maximum temperature. The highest temperature climbed from 489.1 to 500.6 °C when the pattern's spacing fell from 1000 to 50 µm (see the inset in Figure 1-13 (a)) [69].

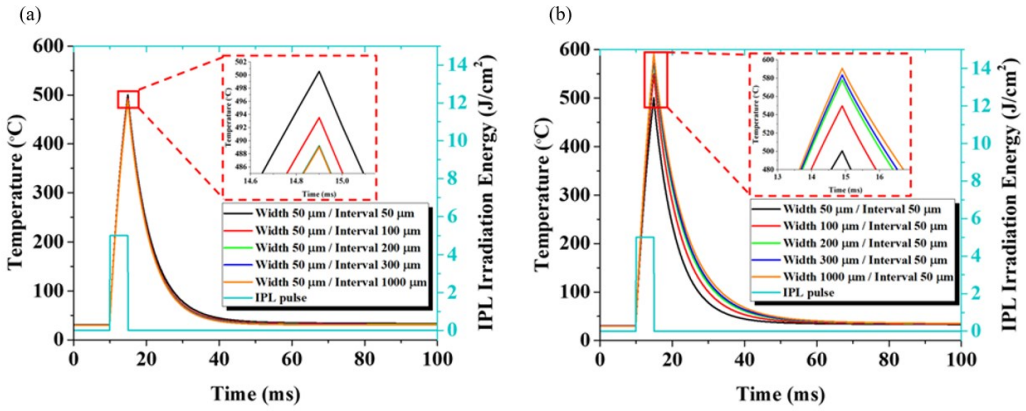

Figure 1-13 Heat distributions of Cu patterns with the same width (a) and interval (b) of 50 µm and varied intervals (a) and width (b) (50, 100, 200, 300, 1000 µm) [69].

The temperature versus time result (Figure 1-13 (b)) was also used to determine the temperature history, which was based on the widths of the Cu patterns. In Figure 1-13(b), the

maximum temperature climbed from 500.6 to 590.8 °Cas the width of the pattern expanded from 500.6 to 1000 μm with a constant spacing (50 μm) [69]. Using the same patterns between digitizers during IPL sintering was their solution regarding controlling the heat distribution in patterns, resulting in consistent line resistance that could be measured over the full digitizer pattern. It has been shown that even sintering of different sized electrodes is attainable if the heat production temperature can be calculated based on the size of the Cu pattern [69].

According to the literature review on metal nanoparticle sintering, the results presented here can provide a view of conventional and IPL sintering, but in the case of different inks printed on a substrate with different absorption coefficients, different IPL parameters should be applied to each part of the printed ink, which is impossible. Selective sintering then can be considered in the case of using laser sintering as a solution. In the next part, some studies regarding sintering using a laser are reviewed. Another problem that IPL sintering can cause is the non-uniform heat distribution where the density of printed patterns can play a role, and it is discussed in the last part of this section, so also laser sintering can be applied to the different parts of the printed patterns to improve the uniformity of the heat distribution.

1.7.3 Laser Sintering

Laser sintering has been studied due to its advantages such as fast sintering, control over size and resolution, and prevention of oxidation [70]. When using laser sintering, three parameters must be adjusted optimally: the scanning interval, the scanning speed, and the output power. Pulsed laser sintering is able to make high-resolution shapes on different substrates while causing minor thermal side effects. Fast pulsed laser sintering has some advantages; it has been proved that fine Ag NP patterns with line widths of several hundred nanometers can be created with resistivity around 20 μΩ.cm [71]. In another study [72], physical aspects of femtosecond laser sintering are considered to investigate the melting, merging, and balling of the thin-film silver nanoparticles by controlling laser fluence, pulse number, and layer thickness (shown in Figure 1-14). In addition, the resistivity versus laser fluence for two different numbers of pulses are studied, and the results are depicted in Figure 1-15. These SEM images show the possibility of controlling the position of patterns using laser sintering, which would be a solution for improving the resistivity variation, discussed in detail in the next chapter.

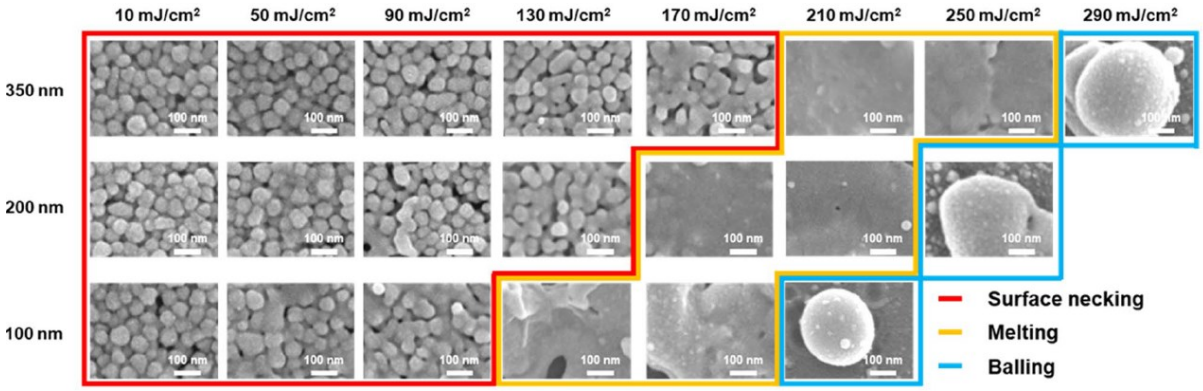

Figure 1-14 SEM images of spin-coated Ag NP after laser sintering with different fluence and thicknesses [72].

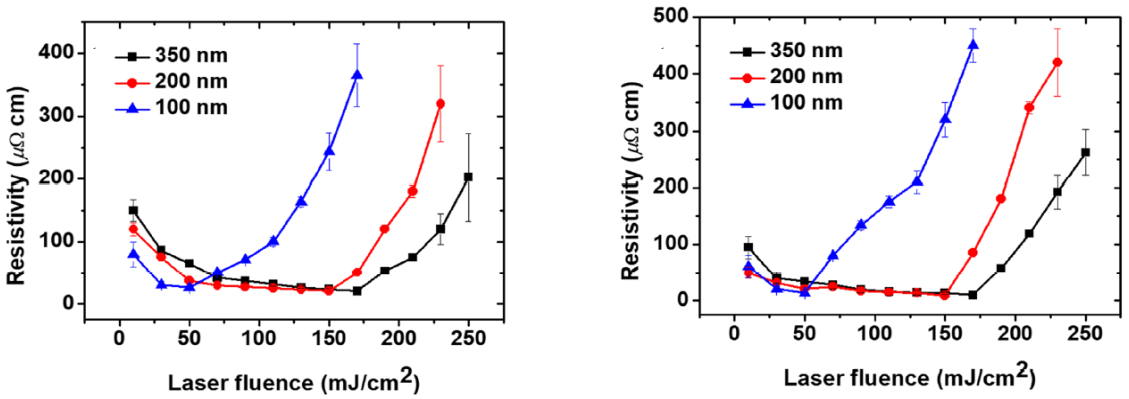

Figure 1-15 Resistivity versus laser fluence for the number of pulses: a) 1000, and b) 10000 [72].

CO_2 laser sintering has emerged as a versatile technique for the fabrication and patterning of metal nanoparticles in various applications. This method has been successfully applied to liquid metal nanoparticles for creating reconfigurable electronic devices, where laser-sintered patterns

enable the formation of resistive and capacitive elements without permanent substrate patterning[73]. Similarly, CO_2 laser-assisted sintering has been used to pattern and sinter titanium dioxide nanoparticles on substrates, preserving the anatase phase and achieving enhanced morphological properties and optical transmittance in the sintered TiO_2 patterns[74]. Localized laser sintering of silver nanoparticles have been employed to reduce bulk resistivity and improve the efficiency of silicon based solar cells, demonstrating the potential of CO_2 laser sintering in reducing fabrication costs and conductivity improvement[75]. These studies collectively highlight the applicability of CO_2 laser sintering in achieving precise patterning, enhanced electrical and optical properties, and cost-effective fabrication in various electronic and energy-related devices.

1.8 Electrical Resistivity Measurement

Electrical characterization is the last step in inkjet printing of conductive inks. The electrical conductivity of a sintered metal nanoparticle film is the essential parameter for determining the film's overall quality. Therefore, it is vital to measure electrical conductivity throughout the development of new processes and during production. As a well-known direct method, the Van Der Pauw technique is used for sheet resistance and resistivity of the thin films printed on the

various substrates. There is a variety of empirical characteristics that have been carried out using this method, including thermal resistivity investigations, due to its adaptability in profiling materials with any shapes and configurations. Here a square shape sample is considered for the VDP technique to take sheet resistance with four-point probes shown in Figure 1-16. The VDP approach would be applied with some assumptions; the most important ones here are thin samples and small contact points on the edge of samples, which are hard to make in real experiments.

1.8.1 Van Der Pauw Technique

VDP technique is explained using Figure 1-16; in this example, the sample is a square with thickness t and length L. The voltage measurement between D and C is taken while a steady current is maintained across the other two connections. $R_{s,exp}$ can be calculated as empirical sheet resistance using Eq. (1.5); four resistance (R_1, R_2, R_3, and R_4) will be calculated in different settings of the probes on the sample, to make sure that the current distribution over the sample is uniform and an average is required to reduce the local inhomogeneity in a sample. We would like to remind the reader that the van der Pauw technique is based on the following assumptions:

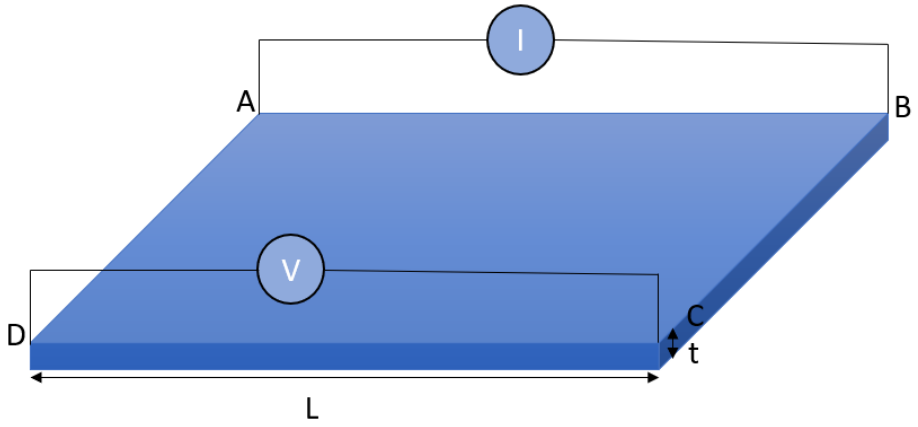

Figure 1-16 Schematic of Van Der Pauw sheet resistivity measurement.

(1) thin thickness, (2) measurement contacts are placed around the sample, in the corners, (3) small contacts compared to the area of the sample, (4) no thickness variation, and (5) no holes on the sample. Most of the time, shapes with a symmetrical axis are used for VDP measurements, but it is possible to be applied to any other shape. For symmetrical shapes, measured R_1, R_2, R_3, and R_4 would be equal, so Eq. (1.5) turned to Eq. (1.6) [76]

$$\exp\left(-\frac{\pi(R_1+R_2)}{R_{s,exp}}\right)+\exp\left(-\frac{\pi(R_3+R_4)}{R_{s,exp}}\right)=1 \tag{1.5}$$

$$R_{s,exp}=\frac{\pi}{\ln(2)}\frac{V}{I} \tag{1.6}$$

1.8.2 Frequency Domain Thermoreflectance (FDTR)

Electricity-based testing requires the creation of contact connections, as well as the use of probes that are potentially damaging to a material's surface and take a long time to align properly. Using sintered films as an example, laser-based thermoreflectance measurements may be used to quantify thermal conductivity, which is closely related to electrical conductivity in sintered films and can be measured using thermoreflectance measurements [77]. A wide range of applications for this rapid and contactless probing method exist, including process monitoring in a manufacturing environment. When compared to fundamental reflectivity, thermal conductivity is a significantly more direct measure of electrical conductivity. One of the important features of deposited nanoparticles is thermal conductivity, and it is also a characteristic that should not be underestimated. When modelling and optimizing sintering parameters, it is vital to understand how thermal conductivity changes as sintering progresses in order to make informed decisions. This is especially true for recent sintering methods such as flashlight sintering, which are currently being developed [78]. Continuous wave laser sintering is ideal for ink printed on temperature-sensitive substrates since it minimizes substrate damage by directing most of the laser energy into the printed ink. As previously mentioned, temperature plays a crucial role in the sintering of metal nanoparticles, influencing the surface morphology through the formation of necks, networks, and grain growth. However, in situ monitoring of continuous wave laser irradiation on printed ink is

challenging. An alternative method is numerical temperature estimation, though its accuracy requires improvement. Understanding the transient thermal conductivity of the laser-sintered ink can enhance the precision of temperature estimations. [79]. The transient resistivity of a conductive nanoparticle ink line is assessed through a furnace sintering process using forced-convection heat transfer at temperatures of 150°C, 200°C, and 250°C for various durations. After each sintering phase, the resistance of the conductive line is measured at room temperature with a multimeter. Additionally, the cross-sectional profile of the conductive ink line is evaluated using a profiler set to a fine scanning speed and resolution, covering the sample width. Multiple points along the sample line are scanned to enhance the accuracy of the cross-sectional area measurement. [80].

In another publication[81], the specifics of the FDTR thermal conductivity measuring apparatus are described in further detail. Figure 1-17 depicts a schematic representation of the measurement setup. It is based on two continuous waves (CW) lasers that operate at wavelengths of 515 nm (pump) and 785 nm (splitter), respectively (probe). When an analog signal is modulated into the pump laser, the probe laser stays unmodulated. The pump laser is focused onto the sample with the use of a 40X objective. In order to avoid back reflections into the lasers, optical isolators are utilized on both beams of light. The absence of a transducer layer on top of the sample was possible because the observed signal amplitude coming from the naked silver sample was sufficient for the experiment to be carried out. The beam from the modulated pump is absorbed by

the sample, causing periodic temperature changes on the surface, which include an additional thermal phase known as thermal phase 1. In FDTR measurements, the thermal phase signal is isolated to obtain more accurate results by analyzing the probe beam ($\theta 1 = \theta\_thermal + \theta\_optical + \theta\_electrical + \theta\_reference$). The pump beam serves as a reference, measured as ($\theta 2 = \theta\_optical + \theta\_electrical + \theta\_reference$). Since both the electrical and optical beams travel the same distance, the thermal phase is determined by the difference: $\theta\_thermal = \theta 1 - \theta 2$. The laser power is kept below 100 μW to prevent any significant temperature rise on the sample's surface. Using Fourier's Law, the thermal conductivity of the thin layer is then calculated by fitting the data to a model[78], [81]. The FDTR method is one of the electrical resistivity measurement methods used in this study and is a non-distructive and high-resolution measurement technique.

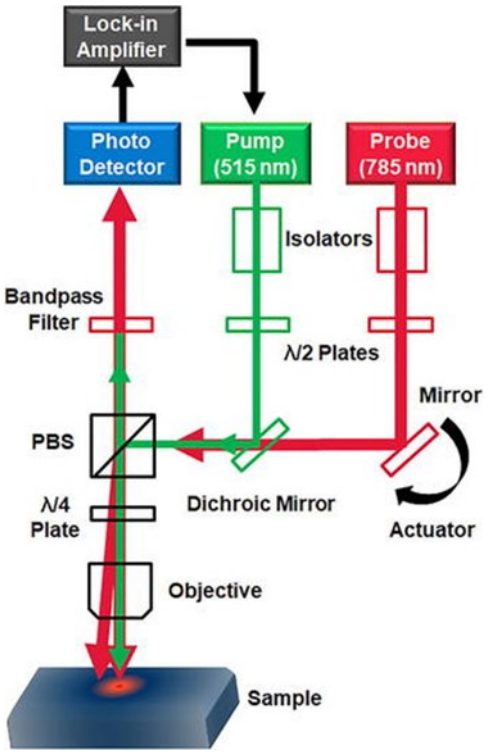

Figure 1-17 An FDTR setup is used, in which a pump laser warms up a spot on a periodic basis while a probe laser is reflected off this point with an added thermal phase. The beams are guided and focused with the help of the reflectors and goal. Collected probe signals are converted to electrical signals using a bandpass filter and photodetector, which are both employed in this application [81]

1.9 Thesis Structure

This thesis is structured into six chapters to systematically explore the challenges and advancements in resistivity uniformity for printed electronics which have mostly been published in [82]:

1- Introduction: This chapter provides a comprehensive literature review on printed electronics, focusing on materials, drying, sintering, and the characterization of printed patterns concerning electrical conductivity. Initially, it discusses various printing techniques used in the industry, highlighting their strengths and limitations. The drying process is then explored, emphasizing the critical factors that influence electrical conductivity during drying and sintering, such as solvent evaporation and ink solidification. Furthermore, advanced sintering techniques, such as laser sintering and IPL sintering, are reviewed for their ability to enhance conductivity and uniformity in printed patterns. The chapter also covers key characterization methods, including the VDP technique and FDTR, which are employed to measure and analyze the electrical properties of printed electronics. These methods are crucial for understanding the impact of various processing parameters on the final electrical performance. By identifying the key factors influencing electrical conductivity during the drying and sintering processes, this chapter

sets the stage for the detailed experimental and theoretical analyses presented in subsequent chapters. The literature review aims to provide a solid foundation for the research conducted, ensuring a comprehensive understanding of the current state and future directions in printed electronics.

2- Drying: Investigates the methods of drying inkjet printed patterns, considering the impact of time, temperature, and the arrangement of adjacent printed electrodes on the drying process and the uniformity of resistivity over inkjet printed electrode arrays.

3- Sintering: Examines sintering as a post-drying process to improve the electrical conductivity of printed electrodes and how it can enhance the uniformity of resistivity across a printed electrode array.

4- Complex Patterns: Studies the non-uniform resistivity issue over more complex patterns applicable in electronic device fabrication, such as spiral patterns, and measures the resistivity of these patterns using the FDTR method.

5- Laser Sintering: Explores the use of diode and CO_2 lasers for fast and selective sintering to improve the uniformity of resistivity over printed electrode arrays and complex patterns.

6- Results and Conclusion: Presents the findings of the research, discussing the implications for printed electronics and future research directions.

1.10 Motivation and Contribution

The motivation for this thesis stems from the increasing importance of printed electronics in additive manufacturing and its application in various electronic devices, such as transistors. A critical aspect for circuit designers is the uniformity of resistivity, which directly impacts the performance of their circuits. However, the drying and sintering processes of printed circuit patterns are often non-uniform, leading to variations in resistivity. This thesis aims to address this challenge by studying the parameters affecting resistivity variations and providing post-drying solutions to reduce non-uniformity. This thesis contributes to the field of printed electronics by providing new insights and methods to improve the uniformity of resistivity in printed circuits. It introduces design rules alongside drying and sintering processes as parameters that can be considered by circuit designers for the first time in this project. The study reveals that the number of printed electrodes in an array, the gap distance between them, and the drying time play significant roles in resistivity variation. It demonstrates that selective sintering can be applied to electrodes to better control the energy required for sintering based on electrode's location in the array. These findings offer valuable guidance for improving the performance of devices fabricated using printed electronics.

Chapter 2 Inkjet Printing and Drying Process

2.1 Introduction

This chapter delves into the processes of inkjet printing with silver and copper-based nanoparticles and the critical drying step necessary for solidifying printed conductors. Conductive, dielectric, and semiconductor patterns are formulated by dispersing nanoparticles into a solvent with agents to enhance printability and prevent agglomeration. The drying process then evaporates the solvent and solidifies the printed material. Regardless of the drying method used, this process is essential for each inkjet printing operation. Controlled by time and temperature, effective drying ensures the solidification of printed materials. The motivation behind this thesis is a novel methodology in printed electronics aimed at achieving high and uniform electrical conductivity across diverse patterns. .

One of the important parameters for printing conductors is the electrical conductivity of the printed metal nanoparticle film. The conventional expectation is that conductivity should remain consistent regardless of variations in pattern design, size, substrate, location, or the density of adjacent patterns. However, our research sheds light on a critical challenge – the presence of

inconsistencies in the drying process leading to resistivity variations. This challenge is particularly pronounced when dealing with patterns in close proximity. To clarify, our experimental investigation in this chapter focuses on arrays of printed square electrodes, revealing resistivity variations dependent not only on the spatial location of each electrode within an array but also on the total number of electrodes present. Under similar drying conditions in terms of temperature and duration, arrays with a larger number of electrodes exhibit higher resistivity variations. This phenomenon underscores the complexity of achieving uniform electrical conductivity in proximity, presenting a significant challenge in the realization of reliable printed electronics.

In addressing these challenges, it becomes apparent that the drying step plays an important role in determining the ultimate electrical conductivity of the printed metal nanoparticle film. In summary, the motivation driving this chapter lies in advancing the understanding of these challenges and proposing novel solutions to pave the way for the realization of high-performance printed electronics.

2.2 Methods

A square pattern (1 mm × 1 mm) is printed individually and in arrays of 9, 25, and 49 squares on borosilicate glass substrates (Fisher Scientific) using two different commercial inks: silver

nanoparticle ink (ANP DGP 40LT-15 C, Advanced Nano Products, Co., Sejong, Korea) and copper nanoparticle ink (Metalon CI-005, NovaCentrix, Austin, TX). Their properties are shown in Table 2-1. The solvent of the silver and copper nanoparticle inks are triethylene glycol monoethyl ether (TGME) and glycol ether respectively. The printed copper and silver electrodes are dried in a vacuum oven and on a hot plate at 60 °C, respectively.

Table 2-1 Silver and copper nanoparticle ink properties (DGP 40 LT-15C and Metalon CI-005)

	Silver	Copper
Solid Content (%)	30~35	26
Viscosity (cPs)	10~17 (adjustable)	13
Surface Tension (mN/m)	35~38 (adjustable)	30
Solvent	TGME	Glycol ether
Washing Solvents	Polar Solvents: Ethyl Alcohol, IPA, etc.	Acetone, IPA
Curing temperature (℃)	Standard convection ovens 120~150 °C, 30 minutes	Standard convection ovens and vacuum ovens at 60°C, 30 – 60 minutes
Specific Resistivity (μΩ.cm)	11~12	9

2.3 Inkjet Printing

The initiation of the printing process involves the jetting of the ink. Initially, manual adjustments to the air pressure are made to facilitate the ink's entry into the nozzle. Once the appropriate printing settings are configured, the controlled formation of droplets and a consistent jetting process enable us to print on the designated substrate.

Drop spacing is a printing parameter that should be considered for a specific ink and specific substrate together. The substrates for this printing are thin Fisher glasses, which must be cleaned and dried prior to use. So, glasses are placed in a glass jar filled with boiling deionized (DI) water, and three drops of Helmanex are added. The jar will be sonicated for 5 minutes, after which the glasses will be rinsed with boiling DI water and sonicated for 5 minutes with isopropanol (IPA) before being washed twice more and dried with compressed air.

In establishing the optimal printing conditions, a drop spacing of 135 μm was identified for both silver and copper to print a continuous line. Any variation in printing speed and nozzle height was observed to compromise the stability and quality of the printed line shape. Initially, attempting to create a square electrode by printing lines in a raster mode resulted in gaps within the square (refer to Figure 2-2 (a)). An alternative approach using a spiral design with a constant drop spacing

also presented some defects (Figure 2-2 (b)). After optimizing parameters such as drop spacing and gap distance between each line, the final spiral design is illustrated in Figure 2-1. This design successfully addressed previous issues, resulting in a final printed electrode without gaps (Figure 2-2 (c)). The individual electrodes were printed on the glass substrate and subsequently characterized electrically.

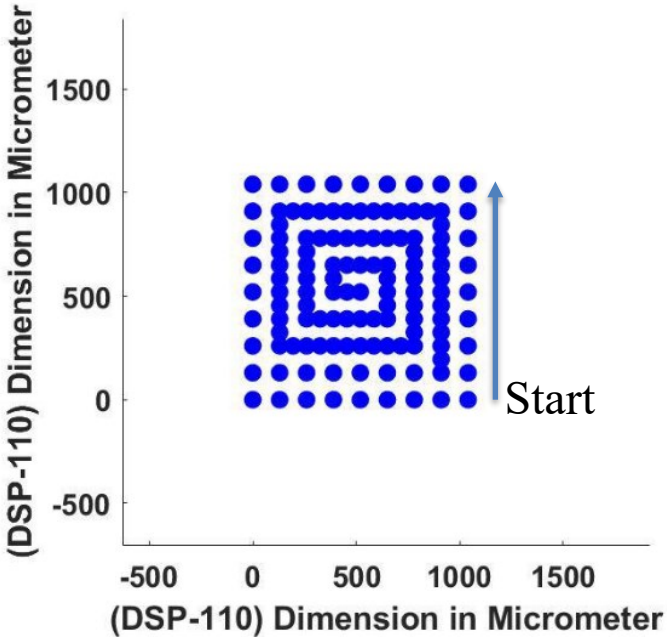

Figure 2-1 Schematic of spiral printing with a modified drop spacing in each round.

The same process was then replicated for copper electrodes. This iterative approach ensured the achievement of precise and reliable conductive patterns on the glass substrate for both silver and copper.

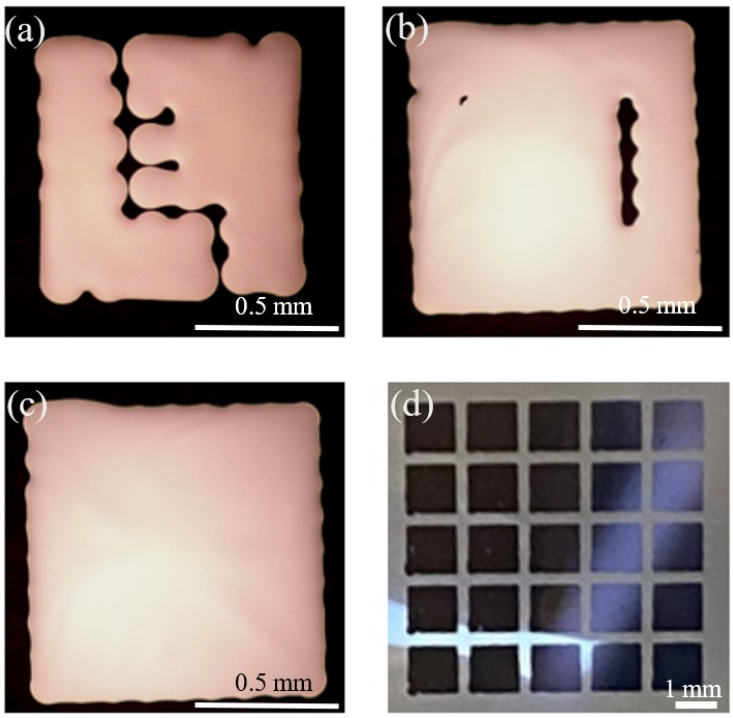

Figure 2-2 Printed square (all electrodes are 1mm×1mm) (a) raster printing with all lines printed next to each other, (b) spiral square with constant drop spacing (130 μm), (c) spiral printing with varying drop spacing, (d) electrode array

The thickness of the printed square electrodes was measured post-drying using a KLA D600 stylus profilometer. The electrodes were printed on glass and dried at 60°C to ensure the evaporation of the TGME solvent. In the thickness measurement of the square-shaped electrode, the method used involved integrating and averaging over the width of the square shape, followed by averaging across multiple samples. The graph presented in Figure 2-3 is an example of the thickness profile of a thick sample.

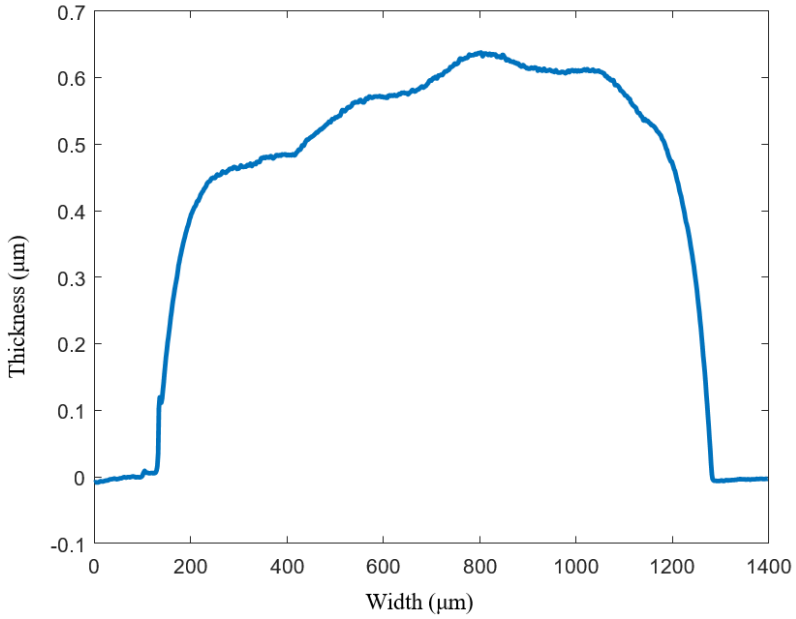

Figure 2-3 Thickness measurement of an individual electrode using stylus profilometry

2.4 Drying

Each sample has one individual electrode printed in the top-left corner of the glass substrate as an indicator and reference electrode for four-point probe resistivity measurement. The first electrode array is printed with nine square shapes (1mm×1mm) electrodes on the glass in a 3×3 arrangement (shown in Figure 2-4) with a gap distance of 100 µm. When measuring resistivity, the electrodes are labeled 1 through 9, and the particular electrode should always be in the top-left

position to ensure a valid set of readings and the resistivity of the individual electrode is measured at 70 ± 6 μΩ.cm.

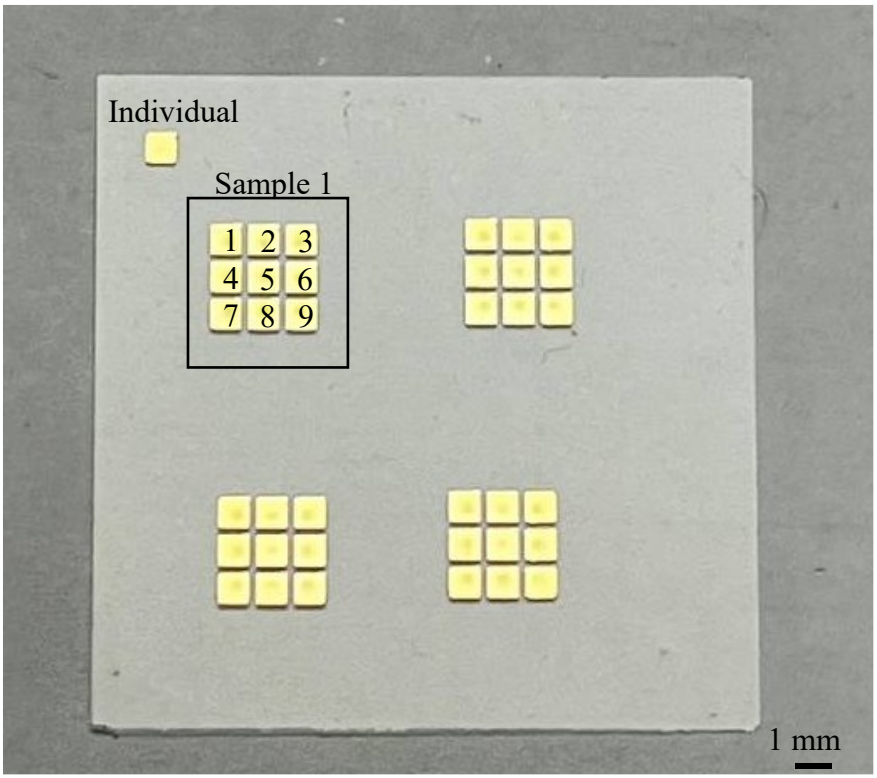

Figure 2-4 Nine electrode arrays printed with individual on glass substrate

To identify the optimal drying time for electrode arrays on the hot plate, we captured images at different intervals. As depicted in Figure 2-5 for silver and Figure 2-6 for copper, non-uniform drying is evident. An individual electrode dries after 5-6 minutes and after 10 minutes a 3x3

electrode array is fully dried, while 5x5 and 9x9 arrays still contain wet electrodes. This non-uniform drying contributes to resistivity variations within the electrode arrays.

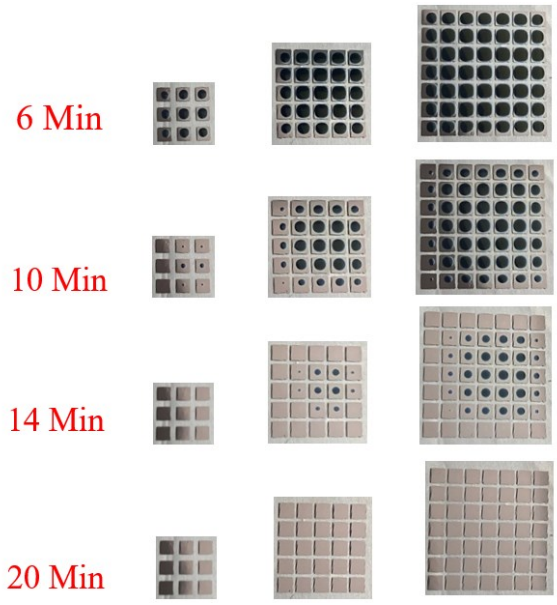

Figure 2-5 Drying pattern of different arrays after 6, 10, 14, and 20 minutes (size of the square electrode is 1mm x 1mm).

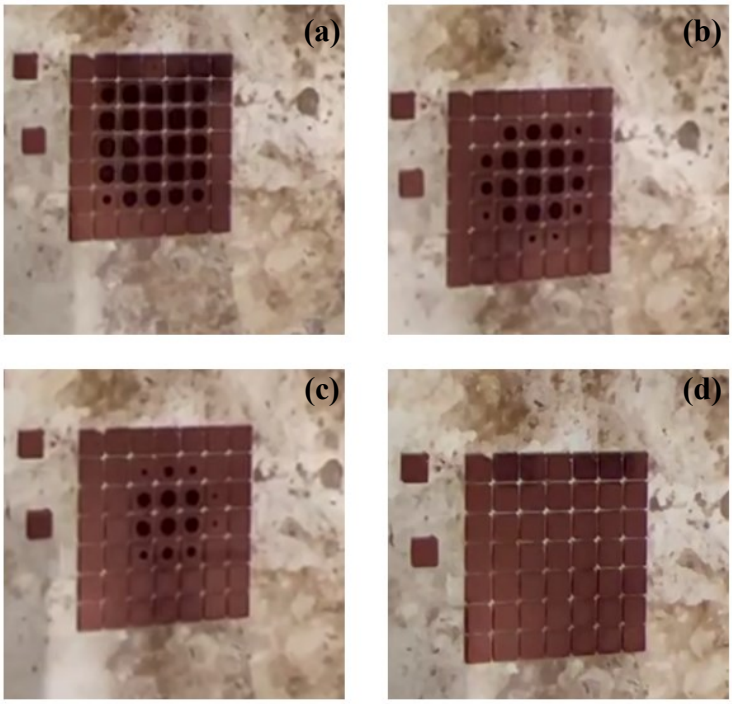

Figure 2-6 Cu printed electrodes (1mm x 1mm) on glass substrate after a) 2 minutes, b) 2:30 minutes, c) 2:50 minutes, and d) 3:10 minutes, drying time.

The drying progression follows a pattern, with individual electrodes in 9, 25, and 49 arrays drying first, followed by the corners, and eventually the center electrode. Figure 2-7 illustrates the resistivity variation for the center electrode in 9, 25, and 49 electrode arrays after the same drying time. In studying the resistivity variations across different electrode arrays, an increasing pattern occurs as the number of electrodes increases. When the electrode count is increased from 9 to 25, a 50% increase in resistivity is observed, suggesting a correlation between electrode density and

resistivity. This trend is further exemplified as the electrode count rises to 49, at which point the resistivity exhibits a 125% increase from the baseline established at 9 electrodes. These findings imply that the resistivity of the center electrode is significantly influenced by the number of electrodes in the array. It is important to consider these variations for the accurate calibration and application of these electrode arrays in practical situations, particularly when uniform current distribution and thermal stability are critical for the intended use. The consistent increase in resistivity underscores the need for design considerations in denser electrode configurations to control the resistive effects observed.

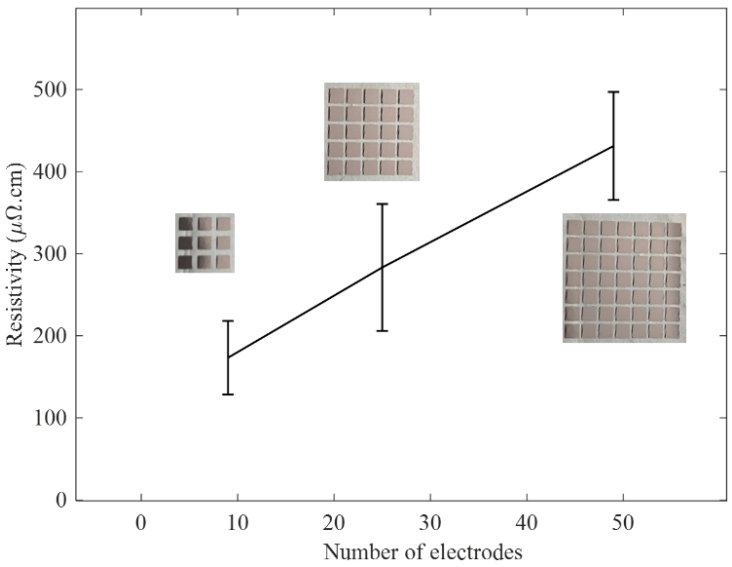

Figure 2-7 Resistivity variation for center electrodes in 9, 25, and 49 electrode array (with 250 μm gap distance) after drying at 60℃ for 30 min on a hot plate (the error bar represents standard deviation).

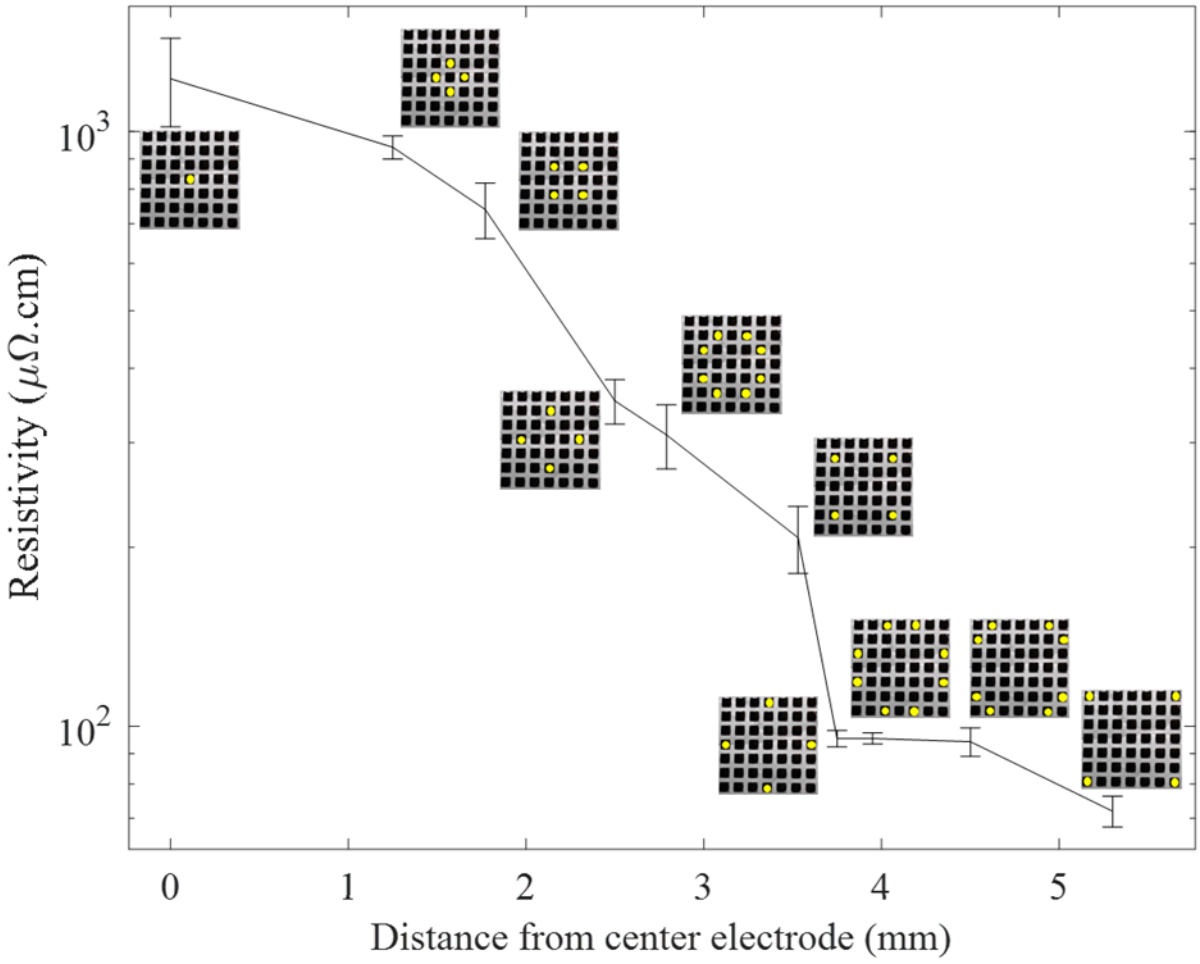

Figure 2-8 Resistivity versus distance from the center for 49 electrodes.

Figure 2-8 reveals the relationship between the spatial positioning of electrodes within a 7x7 array and their corresponding resistivity values. As indicated by the plotted data, there is a discernible trend of decreasing resistivity with increasing distance from the central electrode. The

central electrode, marked by one yellow dot, exhibits the highest resistivity, which systematically diminishes as one moves towards the corner of the array. The trend is non-linear, with a more pronounced drop within the initial millimeters from the center, gradually flattening as the distance extends. This suggests that the electrical resistivity near the center of the electrode array is significantly different from that at the corner, potentially due to the non-uniform drying pattern that is mentioned above. The decrease in resistivity with distance reflects drying earlier than the center electrode. The observed resistivity gradient underlines the importance of positional awareness when taking electrode array measurements, especially for applications that rely on precise electrical characterizations, such as in sensor devices.

To gain an understanding of these variations, resistivities of corner and center electrodes in arrays consisting of 9, 25 and 49 electrodes were measured in 3x3, 5x5 and 7x7 configurations, respectively. Results are shown in Figure 2-9. The error bars represent the standard deviation of measurements from four samples.

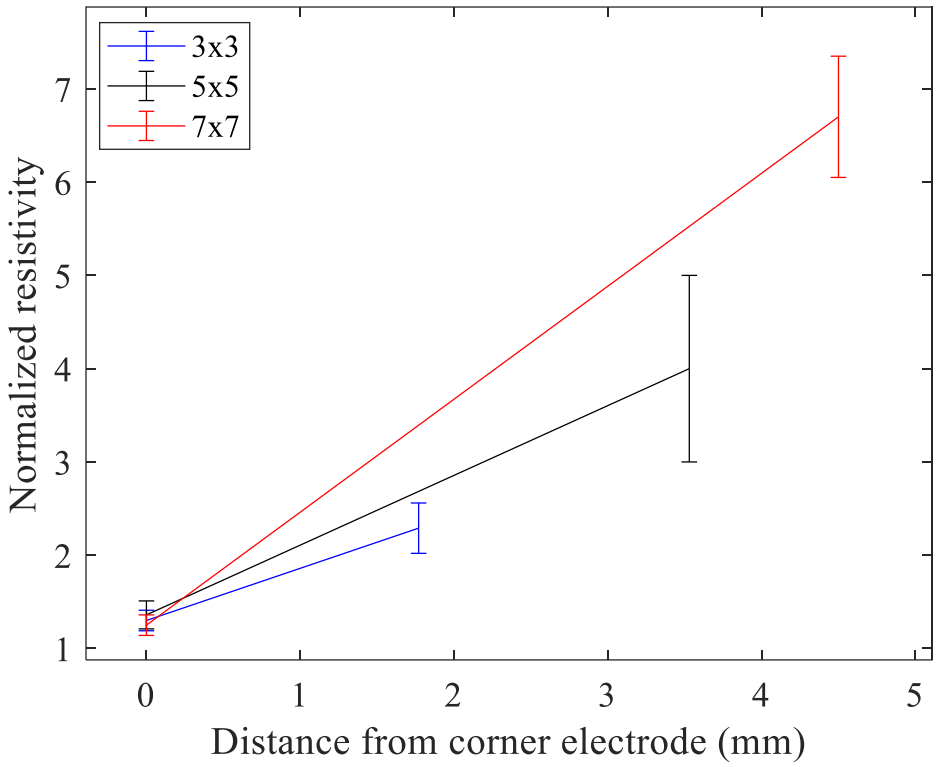

Figure 2-9 Normalized resistivity of corners and center electrodes to individual for 9, 25 and 49 electrode arrays

Studying the normalized resistivity across varying electrode array sizes reveals significant trends. For the 3x3 arrays, which serve as the baseline for comparison, the center electrodes manifest a resistivity that is approximately 86.7% higher than that of the corner electrodes. This difference becomes more pronounced in the 5x5 arrays, where the center electrodes display a resistivity that is nearly 194.1% greater than their corner and 67.4% higher than the center

electrodes in the 3x3 arrays. The trend continues with the 7x7 arrays, where the center electrodes' resistivity rises to 436% above that of the corner electrodes, and a 180.3% increase from the 3x3 center electrodes. These observations show a consistent pattern where the center electrodes exhibit higher resistivity relative to the corners as the array size increases, as well as a significant resistivity increase in the center electrodes themselves as the array size expands.

In order to confirm the generality of this issue for other inks, in Table 2-2, we present the resistivity characteristics of copper ink for corner, center, and individual electrodes, subjected to different post-printing treatments. Although the sintering process will be explained in detail in the next chapter, it is worth noting that, in this case, the copper ink was not conductive after drying. Therefore, a post-drying process, IPL sintering, was applied. Following the drying processes on a hot plate and in a vacuum oven, both maintained at 60°C for one hour, the samples underwent IPL sintering with the application of three pulses at 2600 V and a 3 ms on/off time duration. The central electrode exhibits higher resistivity compared to the corner and individual electrodes, a trend that aligns with observations from silver ink experiments. After drying, the variation between the corner and center electrodes is 145.5% for hot plate drying and 121.4% for vacuum oven drying. A comparison between individual and center electrodes under identical conditions reveals variations of 170.9% and 125.7%, respectively.

Table 2-2 Resistivity of corner, center, and individual electrodes after drying on a hot plate and in a vacuum oven followed by sintering (Copper)

	Hot Plate-Resistivity (μΩ.cm)	Vacuum Oven-Resistivity (μΩ.cm)
Corner 1	71.53 ± 0.35	52.3 ± 0.23
Corner 2	77.42 ± 0.78	46.94 ± 0.54
Corner 3	86.93 ± 0.87	53.21 ± 0.67
Corner 4	77.68 ± 76	45.15 ± 0.76
Center	192.49 ± 34.87	109.38 ± 2.57
Individual	71.05 ± 0.03	48.47 ± 0.08

2.5 Vapor Density Effect

In order to control the vapor density, drying in the vacuum oven would be a potential candidate and was studied using silver ink. After drying 49 silver electrodes at 60 °C in the oven for 30 minutes, the average of corners is 14.4 ± 0.98 μΩ.cm, and the center is 16.42 ± 0.97 μΩ.cm, which is about 14 % variation, so the vacuum drying can improve the uniformity, but the vacuum process would take time and decreases the manufacturing throughput..

Another method for lowering resistivity variation is to create a saturated atmosphere using the solvent TGME. To do this, numerous droplets were dripped on four glass slides and placed next to the printed samples, then covered the whole setup with a glass lid, which created a small

saturated atmosphere (shown in Figure 2-10). The drying process with TGME takes 45 minutes, which is 2.25 times longer than regular drying, with a resistivity variation of 25.15 % between individual and center. Compared to normal drying (556.7 %), this test demonstrates that raising the overall vapor density of TGME improves resistivity uniformity; nevertheless, the images demonstrate that there is still some non-uniform drying as the corners dry first, and the drying duration also plays a role. Another variable that affects uniformity is the array's location on the glass substrate; it is evident that the top of the electrodes, which is the farthest from the TGME slide, dried quicker than the bottom, right, and left. The measurements back up that claim: corner 1 in the top-left is 18.01 μΩ.cm, while corner 4 in the bottom-right is 23.27 μΩ.cm. This approach seems to be quite sensitive to the TGME vapor density and array location, which gives additional factors to adjust the uniformity. As shown in Table 2-3, the ratio of corner to corner resistivity in ambient atmosphere is around 13%, while in saturated TGME atmosphere is 33%. Without added TGME vapor in a regular drying process (a comparison between saturated atmosphere and atmospheric conditions in terms of resistivity variation between corners and center is shown in Table 2-3), as the evaporation of corner electrodes starts, the vapor density in the proximity of the gas-liquid interface of the center electrode increases, therefore reducing the evaporation at the gas-liquid interface of the center electrode, which causes a ratio of 705% under atmospheric conditions and 395% for a saturated environment for center electrode over corner electrode.

Table 2-3 Comparison between saturated atmosphere and atmospheric conditions

	Corner to Corner	**Corner to Center**
Saturated atmosphere	33.3%	395%
Atmhosperic condition	12.8%	705%

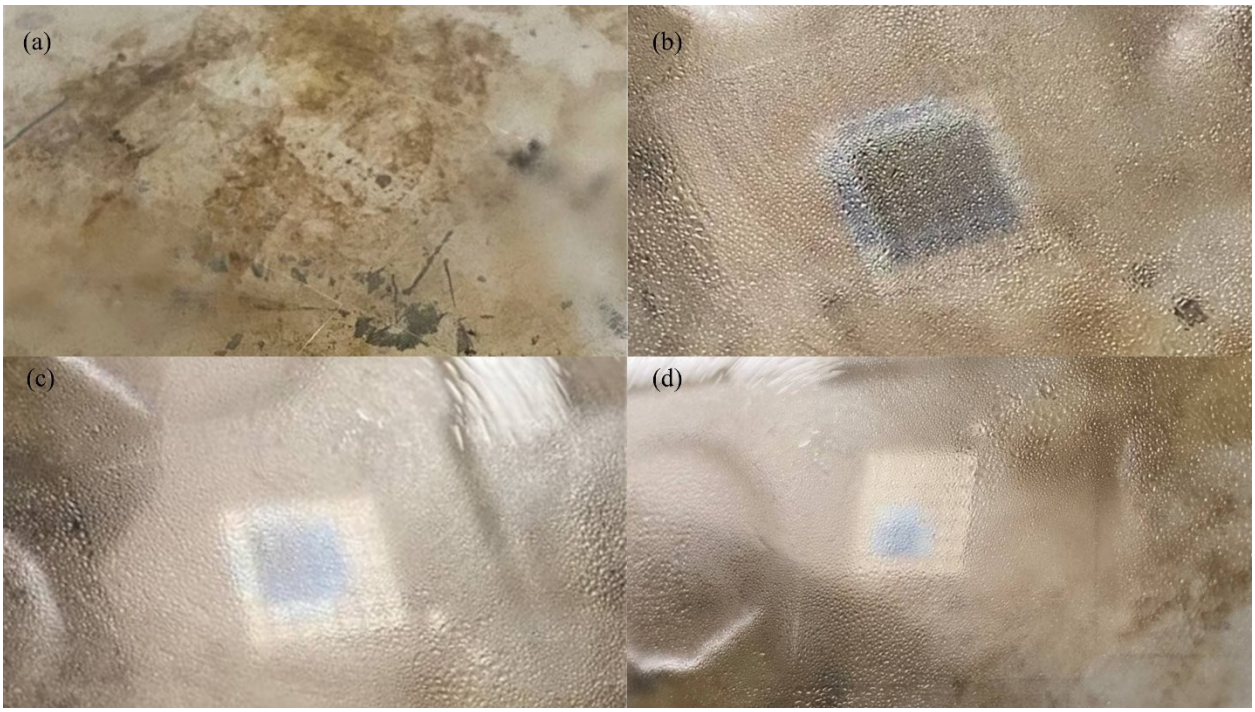

Figure 2-10 The saturated atmosphere with TGME for drying of 49 electrodes on a glass substrate, surrounded by four glass slides containing TGME drops, a) saturated atmosphere before putting a sample on the hot plate and under the glass cap, b) 10 min, c) 20 min and d) 30 min after the start of drying on the hot plate.

2.6 Complex Pattern Drying

The pattern-dependent drying is studied here by printing various line patterns with different geometries, including square wave shapes, wide U shapes, straight lines, narrow U shapes, and

spirals (refer to Figure 2-11 (a)). These line patterns share the same length and width but exhibit varying local densities and numbers of corners. During the drying step, the solvent's vapor density is higher around patterns characterized by increased local pattern density.

The printed patterns are dried at 60 °C for 25 minutes. All the shapes are printed with the same total amount of silver ink, which is 1,288 drops, and the same linewidth. By controlling the total amount of silver ink (1,288 drops) and maintaining the same linewidth, we ensured that variations in ink quantity per unit length and trace thickness as well as overall trace length were not contributing factors to the observed resistivity differences between different shapes. The only difference between the patterns is the number of corners and the local density of the pattern. To calculate resistivity from resistance measurements for the different patterns, microscope images of the printed patterns were imported into COMSOL Multiphysics with the average thickness of each pattern obtained from profilometry, and the current and voltage distributions were calculated. The results show a clear trend of increasing resistivity after drying with increasing pattern density in Figure 2-11 (b). The spiral design with the closest printed features, i.e. adjacent lines, shows the highest resistivity after drying compared to other shapes (57% larger than the line shape with the lowest density). The wide U shape and narrow U shape are two examples of the same fundamental shape to study the effect of pattern density. The narrow U shape shows a higher resistivity after drying compared to the wide U shape (26.8% higher). These experiments show that drying is

dependent on the pattern geometry and compact designs with small gap distances dry more slowly than less dense designs resulting in a higher resistivity for the same drying time.

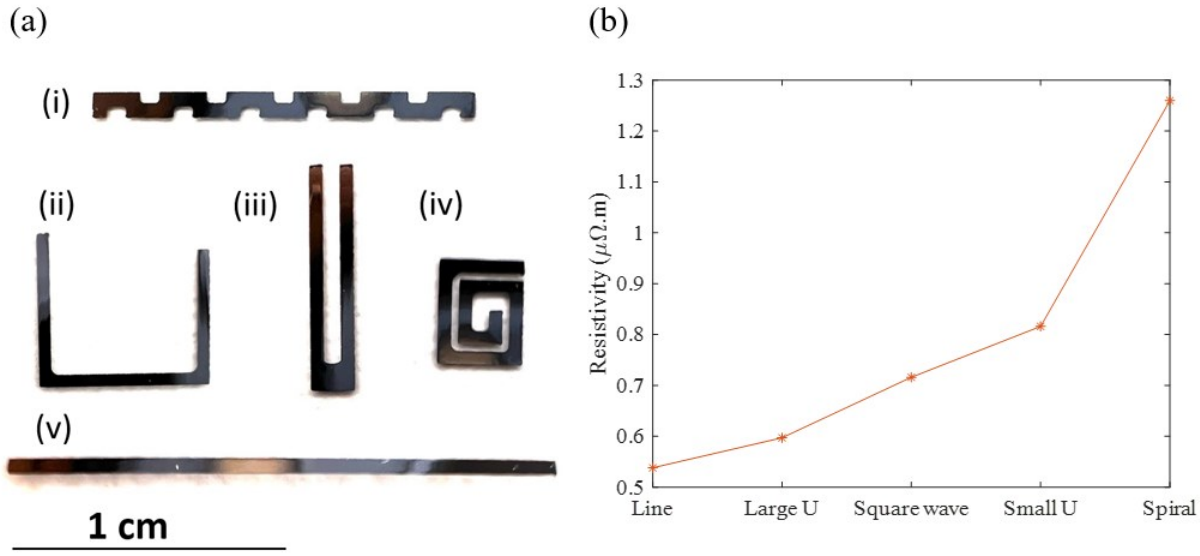

Figure 2-11 a) Different pattern geometries that were studied after drying and sintering: (i) square wave, (ii) Wide U shape, (iii) Narrow U shape, (iv) spiral pattern, and (v) straight line. b) Resistivity of these patterns after drying and sintering, which shows an increasing trend from line to spiral pattern.

2.7 Non-Symmetrical Drying

Another challenge in the nonuniform drying of electrodes is the inconsistent drying of different corners within each array. To study this non-symmetrical drying behavior, three different samples were prepared: one with 49 electrodes and two individuals at one corner of the array (a), another with four individual electrodes located at each corner of an array (b), and a third with the array positioned at the center of the glass (c), as depicted in Figure 2-12. Based on Figure 2-12 (a) and (b), it is evident that the individual electrodes surrounding the array do not significantly influence the drying process as the individuals are printed far from the array. However, the electrode array printed at the center of the glass exhibits symmetrical drying. In terms of resistivity variation, as shown in Table 2-4, the standard deviation between each set of corners in configurations a, b, and c is in a range between 0.93 μΩ.cm to 5.68 μΩ.cm, while the standard deviation between average of corners and average of centers is around 754.45 μΩ.cm, which is considerably larger than the standard deviation between corners, so the non-symmetrical drying can be considered as a small measurement error. Shifting the position of the electrode array on the substrate and also the position of individual electrodes around the array do not have any significant effect on the drying pattern and resistivity variation.

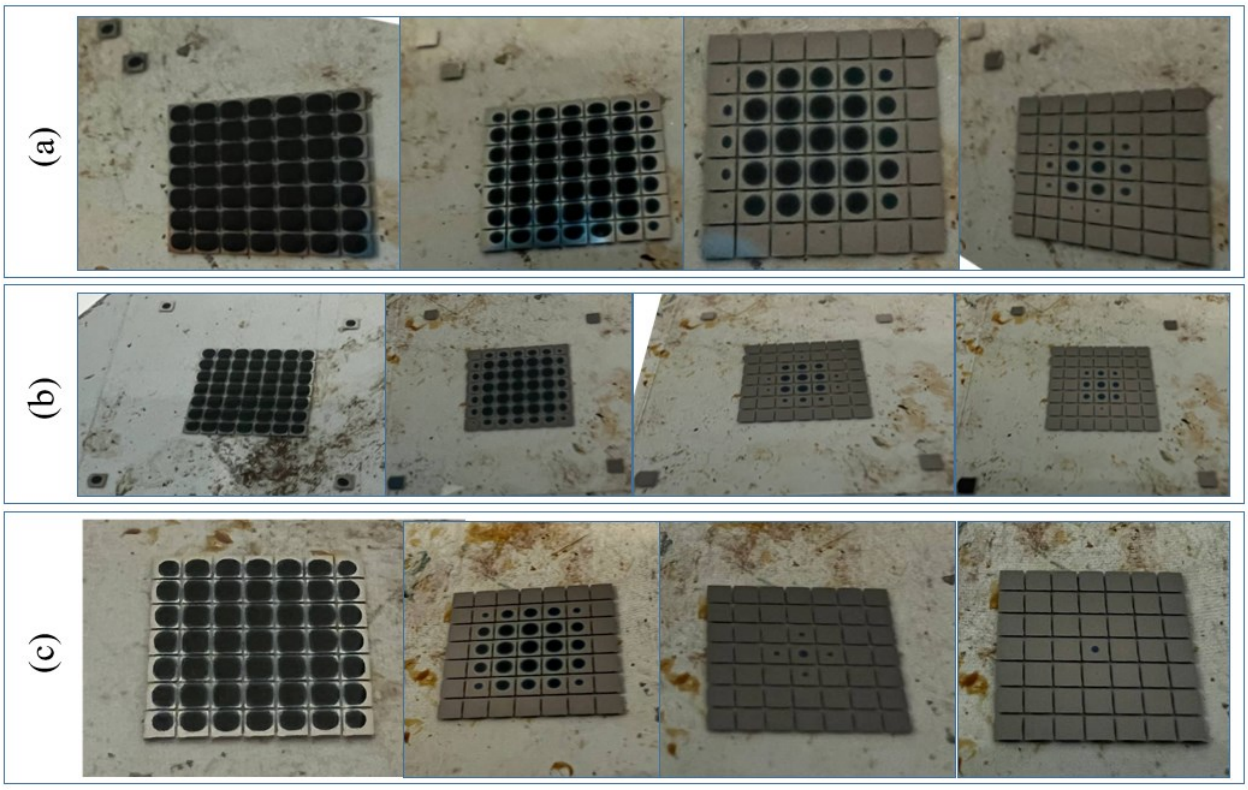

Figure 2-12 Three different configurations of printing 7x7 electrode array on glass substrate in terms of its location and the individual electrodes location , a) two individuals in one corner of the array, b) with four individual electrodes, one in each corner of the array, and c) printing the array in the center of glass substrate.

Table 2-4 Electrical resistivity of corner and center electrodes after drying in three different configurations of electrode array.

	Resistivity (μΩ.cm)				
Sample	Corner 1	Corner 2	Corner 3	Corner 4	Center
(a)	76.43	78.65	74.35	76.98	1129.22
(b)	86.54	79.67	74.45	78.23	1187.38
(c)	73.21	74.54	76.37	71.67	1112.57
Corner to Corner/Center Standard Deviation	5.68	2.22	0.93	2.84	754.45

2.8 Scanning Electron Microscopy (SEM) and X-ray Photoelectron Spectroscopy (XPS) Characterization

The reason for resistivity variations between individual, corner and center electrodes in arrays after hotplate drying could be different amounts of carbon-based materials (binders, surfactants, ligands, and residual solvent) that remain in the electrodes. In order to study the residual ink after 30 minutes of drying on a hot plate at 60 °C, XPS is used for individual, corner, and center electrodes of a 7×7 electrode array with a gap distance of 100 μm. The results are shown in Table 2-5 and confirm that after drying of the electrodes, the residual amount of carbon-based materials is dependent on the position of electrodes in an array, which causes resistivity variations. SEM images of individual, corner, and center electrodes (Figure 2-13) show the morphology of the printed films after drying and IPL sintering. After drying before sintering, SEM images show individual particles and no significant difference in morphology because particles are not sintered yet. Differences in resistivity can be explained by the differences in carbon content from XPS (Table 2-5). After sintering, the images reveal distinct crack patterns, with fewer cracks in the individual electrodes, more in the corner electrodes, and the highest number of cracks in the center electrodes. These observations align with our XPS analysis, indicating that the presence of cracks correlates with the residual carbon residual content after drying and resistivity.

Table 2-5 Atomic percentages of dried electrodes from XPS showing more residual ink inside of arrays.

XPS	C1s	Ag3d	S2p	O1s
Electrode Position	Rel.At.%	Rel.At.%	Rel.At.%	Rel.At.%
Individual	33.4	42.6	19.5	4.5
Corner	42.3	35.0	15.3	7.4
Centre	45.5	32.9	13.0	8.7

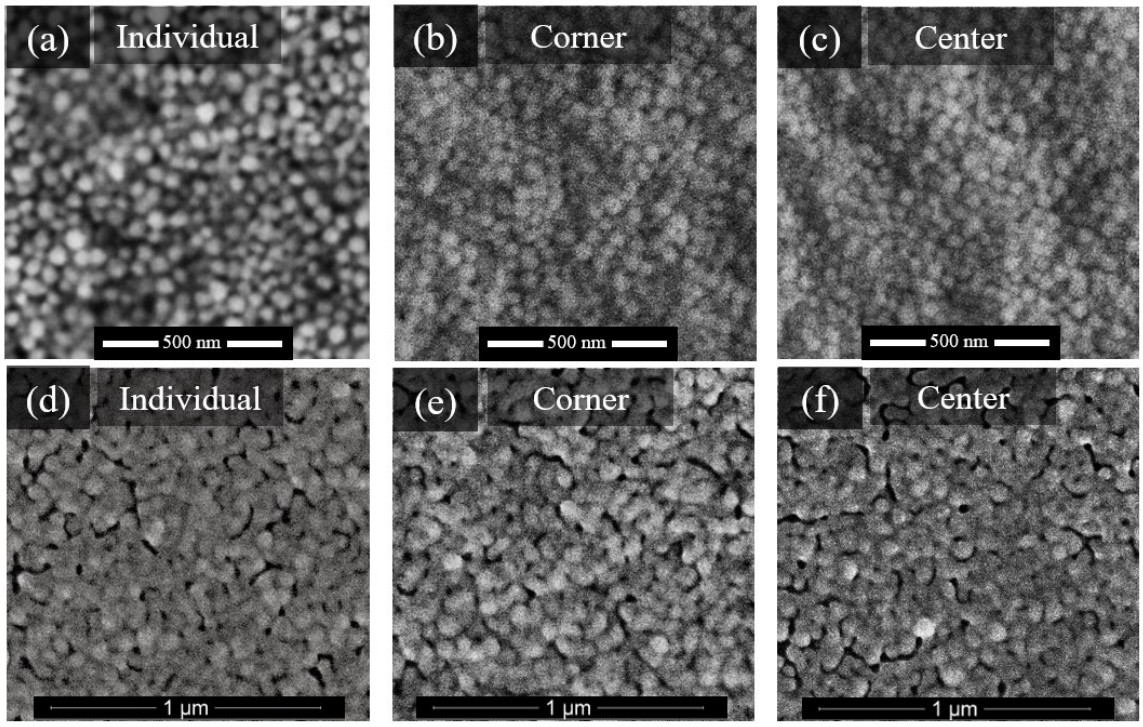

Figure 2-13 SEM images of a) individual, b) corner and c) center electrodes of a 7×7 array after drying at 60 °C for 30 minutes and after IPL sintering (d, e, and f) at 1,020 J/cm2.

2.9 Conclusions

In conclusion, this chapter has demonstrated and studied a significant challenge in the fabrication of printed conductive electrodes: nonuniform drying. It has been demonstrated that the primary cause of this nonuniformity in closely spaced printed patterns is the variation in vapor density of the solvent in the ink. This variation leads to a higher vapor density in the center compared to the corners, resulting in a slower evaporation rate for the inner electrodes compared to the outer ones. Consequently, this nonuniform drying directly impacts the electrical conductivity of the electrodes. Also, the study reveals that the variations in resistivity among individual, corner, and center electrodes in arrays after hotplate drying are attributable to the different amounts of residual carbon-based materials, as confirmed by XPS analysis. The morphology of the printed films, as observed in SEM images, further supports this finding, with the presence of cracks indicating the absence of residual carbon content, which correlates with resistivity variations even after sintering using IPL method. In the following chapter, we will further explore the sintering process as a potential solution for different electrode arrays and examine the electrical resistivity post-sintering.

Chapter 3 Sintering Process

3.1 Introduction

Sintering is a post-drying process that enhances the electrical conductivity of printed electrodes. This chapter explores two main sintering methods: thermal sintering and IPL. The focus is on assessing their impact on the electrical resistivity of printed electrodes, particularly in arrays with varying numbers of electrodes and gap distances. In the context of printed electronics, sintering is essential as it addresses the challenge posed by carbon-based ingredients such as ligands and binders in metal nanoparticle inks. These components, which are vital for making the ink printable, act as barriers to electrical conductivity. The sintering process melts and fuses nanoparticles, thereby reducing electrical resistivity and enhancing conductivity.

The relevance of this chapter to the overall theme of the thesis lies in the examination of IPL sintering as a method to improve resistivity uniformity. IPL sintering can increase the temperature of central electrodes more than those at the corners, acting as a feedback mechanism for uniformity enhancement. However, this process involves a trade-off to avoid oversintering, which is determined by the parameters of IPL sintering, such as the number of pulses and voltage (energy

density). The specific objective of this chapter is to show how adjustments in IPL parameters can lead to improved resistivity uniformity in printed electrode arrays. The chapter begins with an overview of thermal sintering, highlighting its limitations in terms of sintering time and resistivity uniformity. The main focus then shifts to IPL sintering, where the effects of varying energy densities on resistivity uniformity are thoroughly investigated.

3.2 Thermal Sintering

The electrical resistivity of a 7×7 electrode array with a gap distance of 100 μm is studied using a hot plate at different temperatures (60 °C to 160 °C) with a sintering time of 30 minutes. The resistivity of three different electrode locations (individual, corner, and center electrodes) after thermal sintering are shown in Figure 3-1. It shows an improvement in electrical resistivity of all electrodes with increasing sintering temperature and also less variation from center to corners compared to before sintering. However, after sintering at 160 °C, a 17% resistivity variation remains between center and corner and 27% between individual and center.

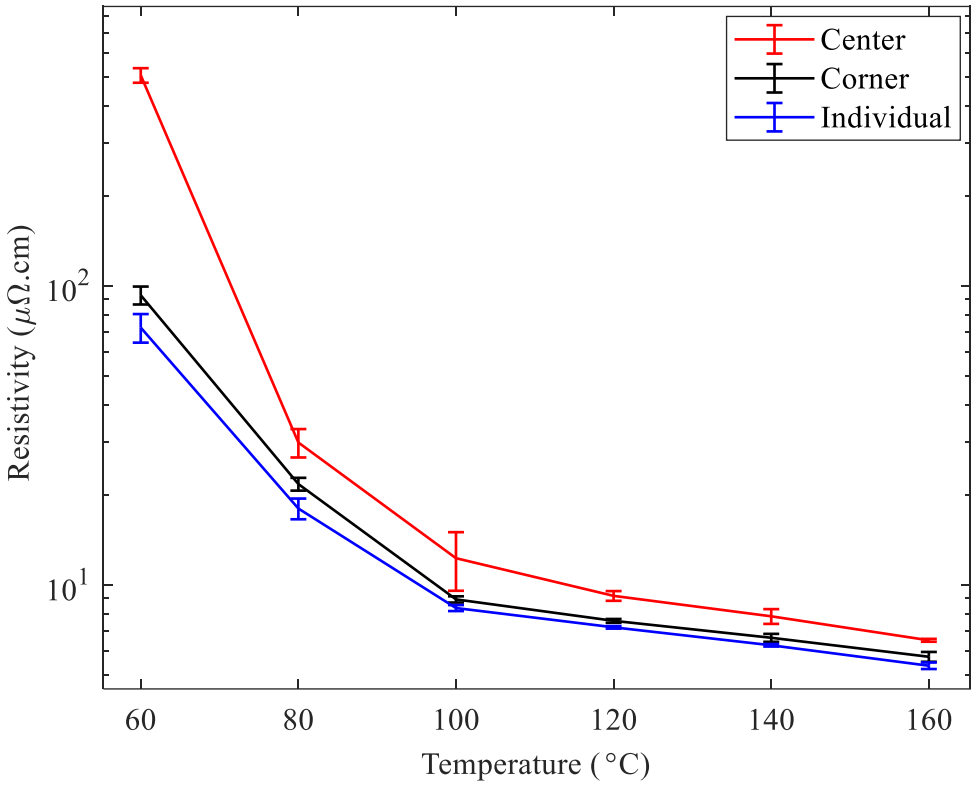

Figure 3-1 The resistivity of corner, center, and individual electrodes in 49 electrode array in different temperatures ranging from 60 to 160 °C for 30 minutes

3.3 IPL Sintering

The prepared films undergo a drying process at 60 °C for 30 minutes prior to IPL sintering, using the X-1100 system from XENON Corporation, Wilmington, MA. The IPL sintering is adjustable through the number of pulses, on and off times, and voltage, which determines the energy density. To identify the optimal sintering parameters, the number of pulses for individual elements and arrays varies between 20 and 180, with voltage settings ranging from 2000 to 3000 volts, while maintaining constant On and Off times of 2 milliseconds. During all IPL sintering experiments, the samples were positioned approximately 2.54 cm away from the lamp's surface.

IPL sintering is applied to all arrays (3×3, 5×5, and 7×7) with the same gap distance (100 μm) with different numbers of pulses and energy densities. During IPL sintering, the voltage is kept constant at 2500 V for a range of 5 to 150 pulses. However, after 150 pulses, the resistivity no longer changes. To continue the sintering process, the voltage is increased to 3000 V and 180 pulses are applied to the electrodes. The resistivity of the individual electrode is shown separately in Figure 3-2 (a), and all the results for arrays are shown in Figure 3-2 (b)-(d). The resistivity of as dried individual electrodes reduces 22 times after initial sintering at 22.5 J/cm^2 (from 66.19±4.27 μΩ.cm to 2.99±1.69 μΩ.cm), while it is 16 times for corner (79.89±3.57 μΩ.cm to 4.99±0.48 μΩ.cm) and 65 times for center electrodes (431.25±65.75 to 6.61±0.62 μΩ.cm) in a 7×7 array.

Increasing energy density to 1,020 J/cm^2 improves the resistivity to 1.85±0.05 μΩ.cm, 2.05±0.09 μΩ.cm, and 2.16±0.06 μΩ.cm for individual, corner and center electrodes, respectively. With increasing number of electrodes, the variation in resistivity from the corner to center electrodes increases after drying. After sintering at 22.5 J/cm^2, corner and center of electrodes in an array with a large number of electrodes still show a higher resistivity than smaller arrays. The resistivity after IPL at 1,020 J/cm^2 does not depend on array size. The resistivity of the center electrode in 3×3, 5×5, and 7×7 arrays is decreased by a factor of 82.12, 136.17, and 199.65 respectively after sintering at 1,020 J/cm^2, which is the best energy density for the lowest variation (less than 6 %) between corner and center as well as the lowest resistivity overall. Conversely, the lowest variation after thermal sintering at 160 °C for 30 minutes on a hot plate is still 17 %.

Oversintering of electrodes after applying pulses with 1,224 J/cm^2 causes a resistivity increase for all electrode arrays and is therefore the limit for increasing the energy density. The SEM images in Figure 3-2 (e and f) show sintered nanoparticles in a corner electrode in a 7×7 array with a gap distance of 100 μm. After sintering at 1,020 J/cm^2, the image (Figure 3-2 (e)) shows a continuous and even silver surface, but after oversintering at 1,224 J/cm^2 some holes can be seen in Figure 3-2 (f), which increases the resistivity.

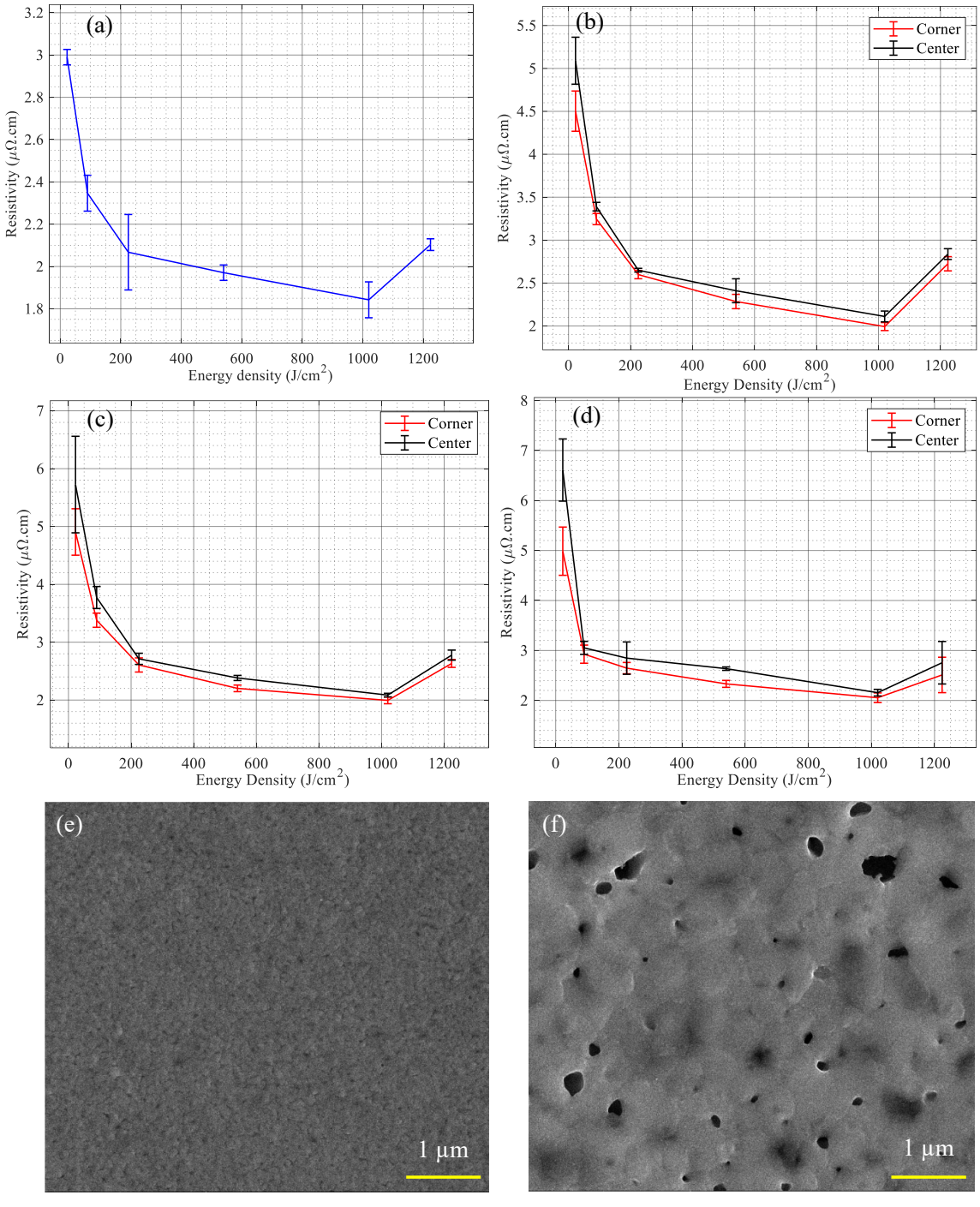
(a)
Resistivity (μΩ.cm)
Energy density (J/cm2)
(b)
Corner
Center
Resistivity (μΩ.cm)
Energy Density (J/cm2)
(c)
Corner
Center
Resistivity (μΩ.cm)
Energy Density (J/cm2)
(d)
Corner
Center
Resistivity (μΩ.cm)
Energy Density (J/cm2)
(e)
1 μm
(f)
1 μm

Figure 3-2 Change in resistivity as a function of energy density for a) individual electrode, corners and centers of b) 3×3, c) 5×5, and d) 7×7 arrays. Note, the y-axis scales are different in these graphs as larger arrays generally exhibit larger resistivity, e) SEM imgage of acorner electrode after sintering at 1,020 J/cm^2 and, f) after oversintering 1,224 J/cm^2.

As discussed for the drying step, another parameter for controlling the resistivity variation in electrode arrays is the gap distance between the printed electrodes. Three different gap distances are studied for a 7×7 electrode array, and the resistivity of electrodes are normalized to the individual electrode as shown in Figure 3-3. Figure 3-3 (a) shows a descending trend for resistivity with increasing gap distance after drying. The resistivity of the center electrode is 6.7 and 5.4 times larger than the individual and corner electrodes, respectively, with a gap distance of 100 µm. This decreases to 1.7 and 1.6 times for a gap distance of 1,050 µm. After IPL sintering with an energy density of 540 J/cm^2, the difference in resistivity of center electrodes between different gap distances decreases significantly (shown in Figure 3-3 (b)). The difference becomes 8.3 % from 100 µm to 500 µm gap distance, and 17 % from 100 µm to 1,050 µm (shown in Figure 3-3 (b)). As mentioned previously, after sintering at 1,020 J/cm^2, overall resistivity is minimized, corners and center have the lowest variation, and the difference between different gap distances is the lowest value as shown in Figure 3-3 (c). Beyond 1,224 J/cm^2, the descending trend with increasing gap distance becomes stronger again and all resistivity values are increased (Figure 3-3 (d)). This means that for a lower gap distance such as 100 µm, oversintering causes a larger resistivity, while

for a larger gap distance such as 1,050 μm the resistivity increase is less pronounced, and it is similar to the resistivity of the same electrodes after sintering at 1,020 J/cm^2 (Figure 3-3 e-g). Also, Figure 3-4 shows the non-normalized resistivity variation of corner and center after sintering at 1,020 J/cm^2 and 1,224 J/cm^2.

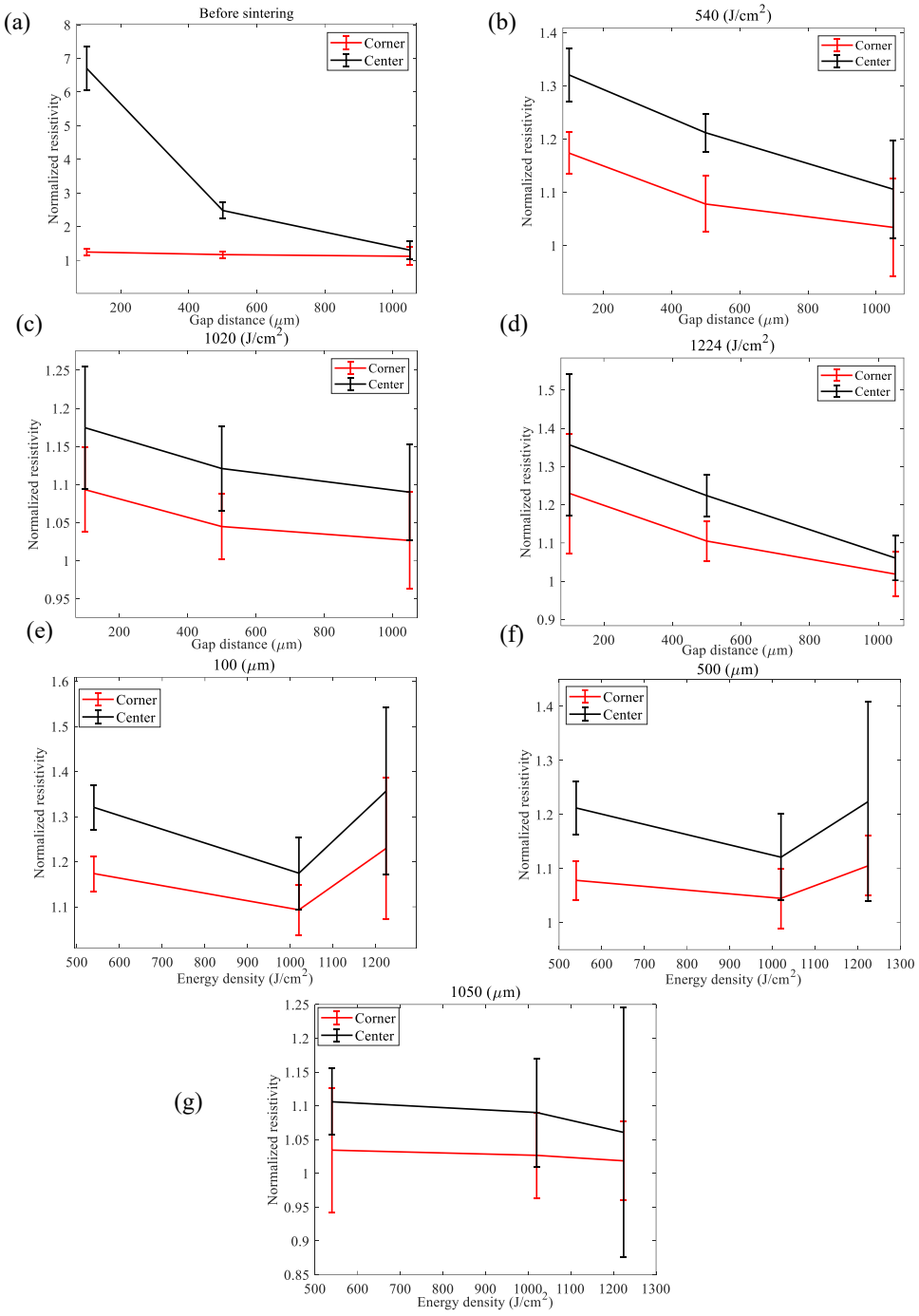
(a)
Before sintering
Corner
Center
Normalized resistivity
Gap distance (μm)
(b)
540 (J/cm2)
(c)
1020 (J/cm2)
(d)
1224 (J/cm2)
(e)
100 (μm)
Energy density (J/cm2)
(f)
500 (μm)
(g)
1050 (μm)

Figure 3-3 Average resistivity of corner and center electrodes in a 7×7 array with three different gap distances normalized to the individual electrode a) after drying, b) after IPL sintering at 540 J/cm2, c) 1,020 J/cm2, d) 1,224 J/cm2, and normalized resistivity of corner and center electrodes for different energy densities at a gap distance of e) 100 µm, f) 500 µm, and g) 1,050 µm. (The error bar represents standard deviation).

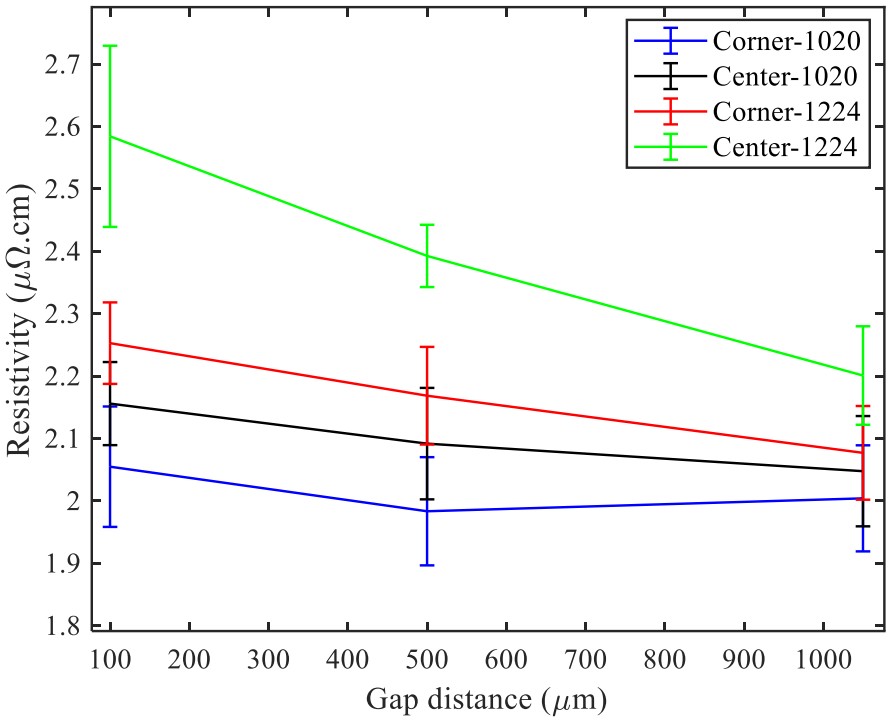

Figure 3-4 Resistivity variation of corner and center electrodes after sintering at 1,020 J/cm^2 and 1,224 J/cm^2.

3.4 IPL Sintering Simulation

The thermal processes during IPL sintering are simulated to gain more insights into the heat and temperature distribution over the printed electrodes on the glass substrate. A time-dependent 3D COMSOL Multiphysics model is created based on the built-in heat transfer models. The model simulates the heat distribution of the IPL on the silver electrodes and solves the heat transfer equation for three main boundary conditions. General inward heat flux on the top surface of electrodes is used to simulate the energy density of IPL sintering. Convective cooling heat flux is applied for both electrodes and glass substrate. Surface to ambient radiation is only used for electrodes. The pulse width and energy density are chosen based on experiments, and a 2 ms pulse with 4.6 J.cm-2 is applied to the 9 (3×3), 25 (5×5), and 49 (7×7) electrode arrays. Only a quarter of each array is simulated using symmetry to reduce the computational volume.

The temperature difference between corner and center at 2 ms is around 200 K and it is not dependent on the gap distance. However, after the end of the light pulse during cooling, the temperature variation is different for different gap distances. At 40 ms, the temperature variation for arrays with 50 μm, 100 μm, 250 μm, and 500 μm gap distance are 42 K, 37 K, 25 K, and 20 K, respectively (Figure 3-5 (a-d)).

This simulation illustrates the temperature distribution over electrode arrays with different gap distances. Printed electrodes with smaller gap distance show a higher resistivity after drying compared to a larger gap distance but the temperature distribution during IPL leads to a higher resistivity reduction factor compared to the larger gap distance. Moreover, the electrodes with smaller gap distance oversinter at a lower energy density compared to the larger gap distance due to the higher temperature difference that also lasts for a longer time for smaller gap distance. The temperature variation is not dependent on the number of electrodes, while it is dependent on the gap distance. For the same gap distance but different number of electrodes, temperature variations are similar. This is also observed experimentally in Figure 3-3 (b-d) where the lowest resistivity and the resistivity after oversintering are the same for different numbers of electrodes with a constant gap distance. This means the gap distance between electrodes plays the most important role, which is shown in Figure 3-6 and Figure 3-7.

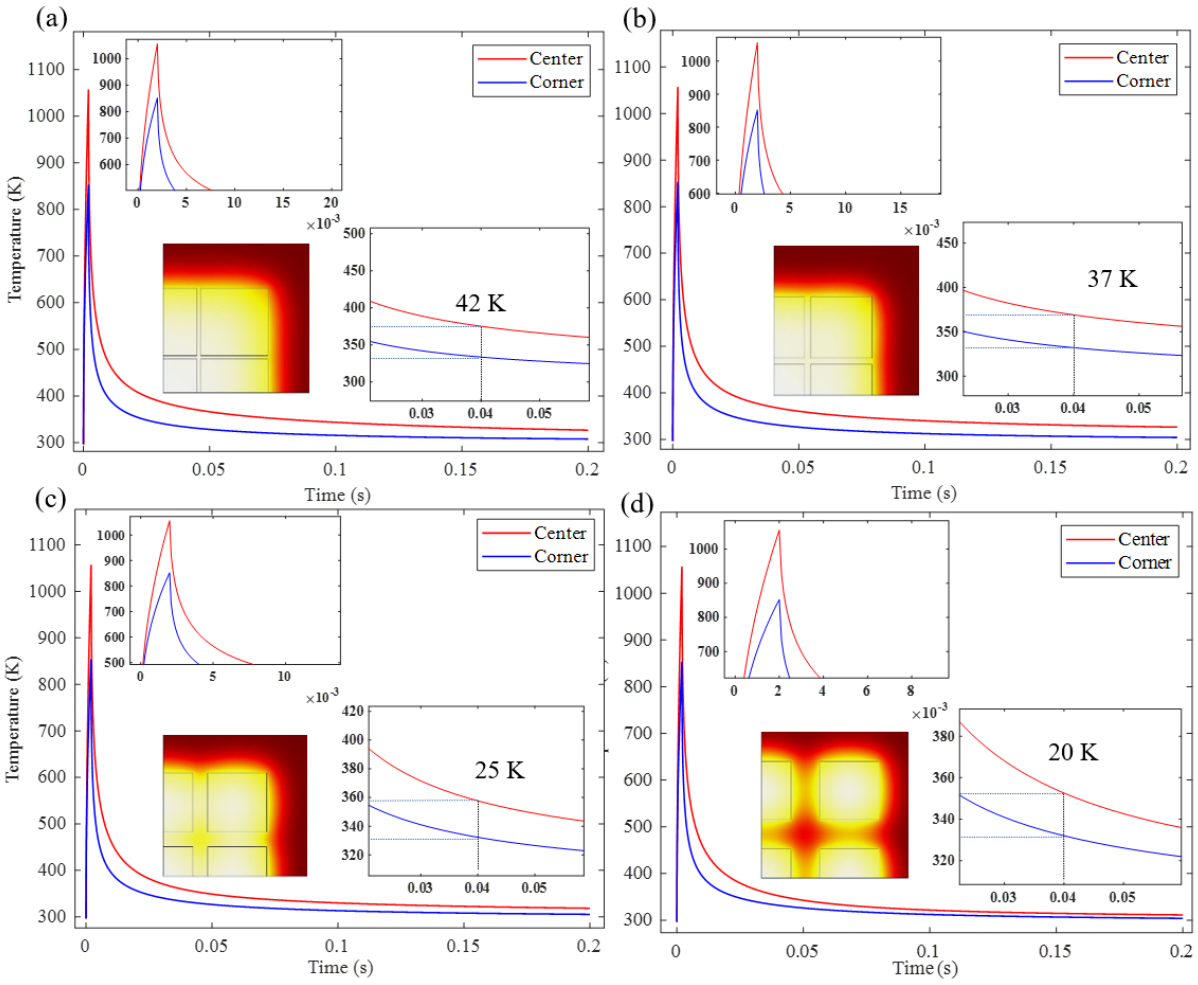

Figure 3-5 Temperature variation during IPL sintering of a 3×3 electrode array with a single pulse of 4.6 J/cm^2 with a) 50 µm, b) 100 µm, c) 250 µm, and d) 500 µm gap distance.

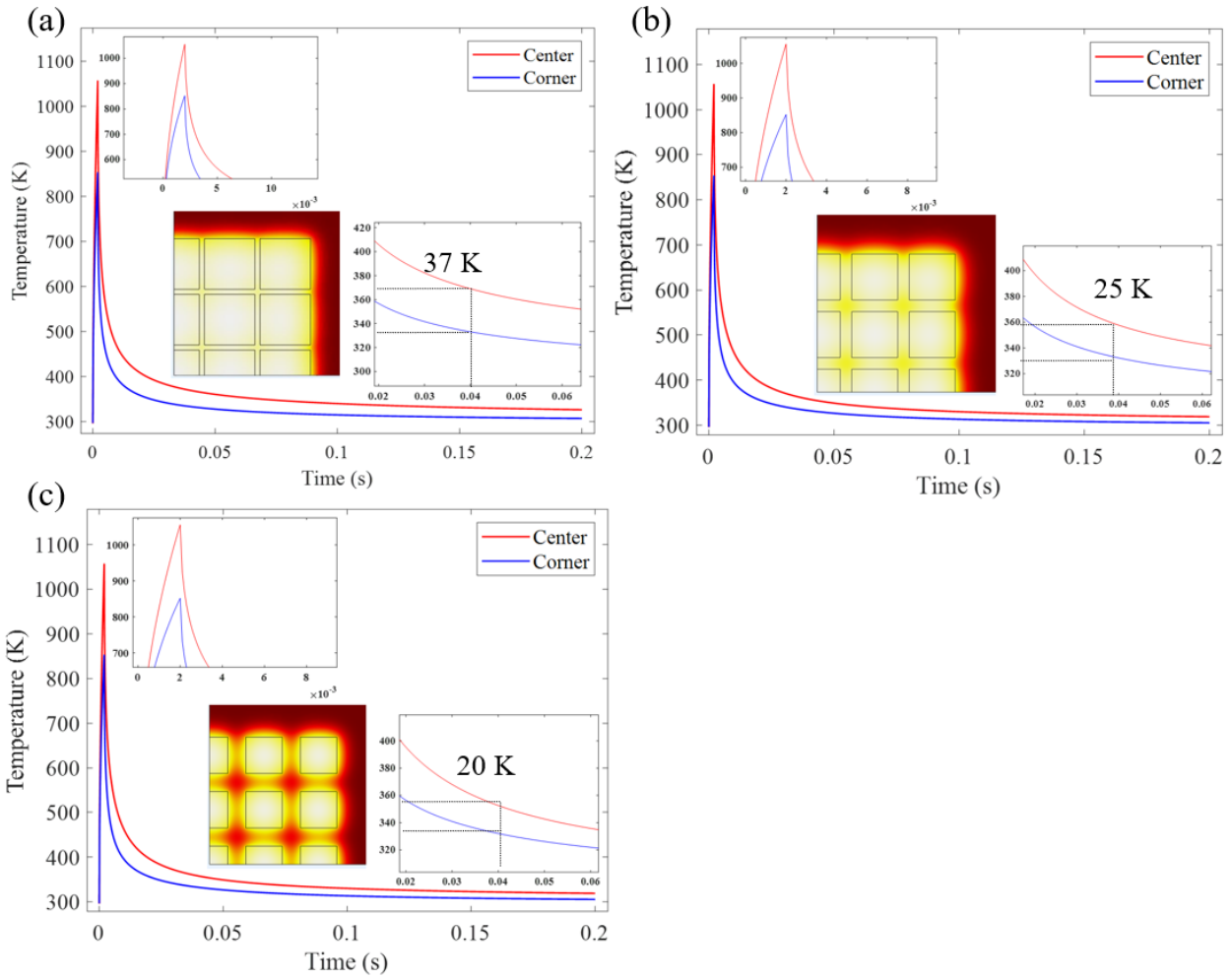

Figure 3-6 Temperature distribution after one pulse at 4.6 J/cm2 for three different gap distances of an array of 5×5 electrodes, a) 100 µm, b) 250 µm and c) 500 µm.

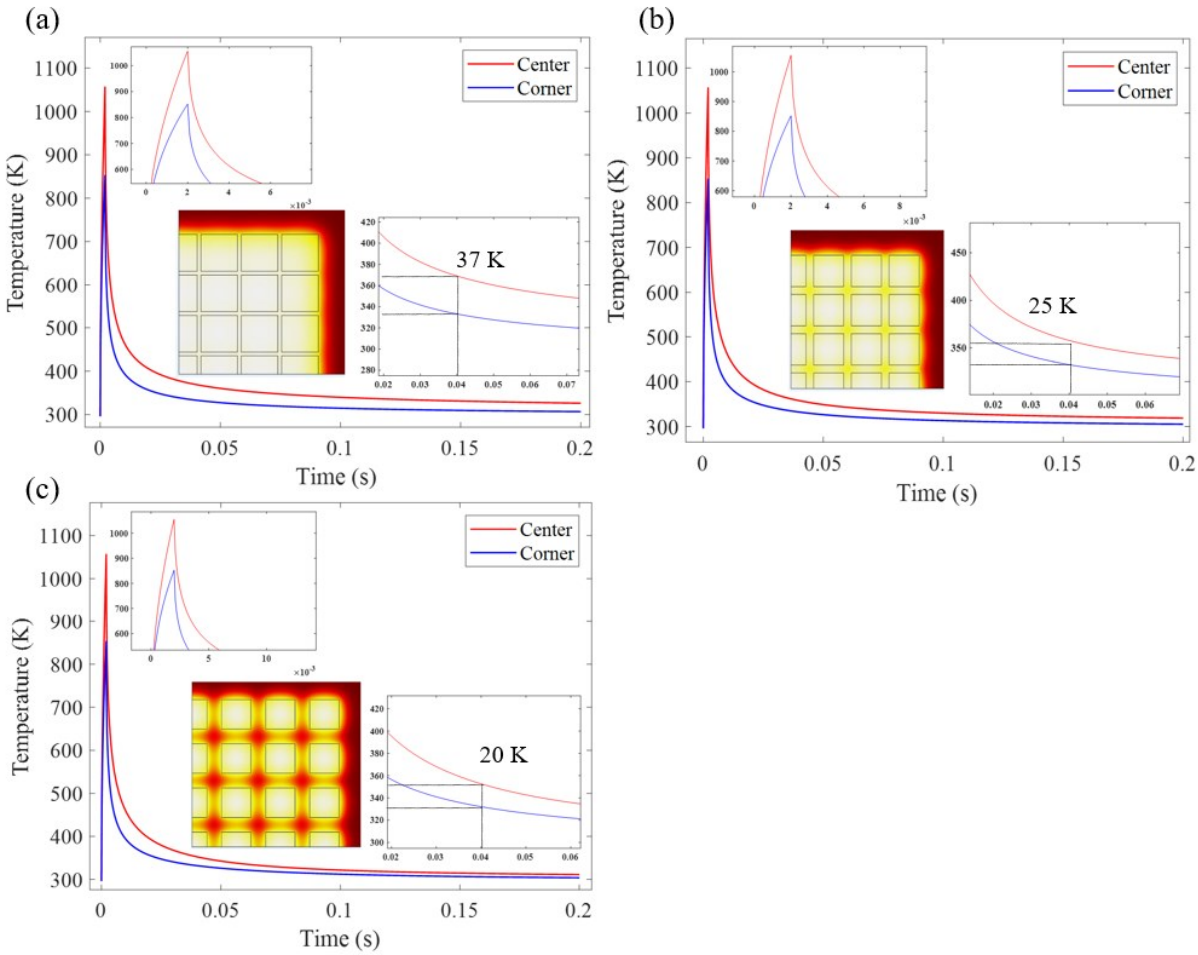

Figure 3-7 Temperature distribution after one pulse at 4.6 J/cm2 for three different gap distances of an array of 7×7 electrodes, a) 100 µm, b) 250 µm and c) 500 µm.

3.5 Conclusions

In conclusion, this study demonstrates the impact of sintering methods on the electrical resistivity of printed silver nanoparticle electrodes. Thermal sintering on a hot plate results in improved resistivity with increasing temperature, but still exhibits a notable variation between center and corner electrodes. IPL sintering, on the other hand, offers a more uniform reduction in resistivity across different electrode locations and array sizes. The optimal energy density for IPL sintering is identified as 1,020 J/cm², which minimizes resistivity variation and achieves the lowest overall resistivity. Visual inspection of the electrodes post-sintering revealed that, regardless of the sintering method employed, all electrodes initially exhibited a consistent silver color with no distinguishable differences, indicating a similar initial surface condition across all methods. The simulation of thermal processes during IPL sintering using a 3D COMSOL Multiphysics model provides valuable insights into the temperature distribution across silver electrode arrays on a glass substrate. The results highlight the significant impact of gap distance on temperature gradients and resistivity changes during sintering, with smaller gap distances leading to higher resistivity reduction and a greater risk of oversintering at lower energy densities. This chapter highlights the importance of considering pattern geometry and sintering parameters in the development of printed electronics processes, as these factors influence circuit performance.

Chapter 4 Complex Patterns

4.1 Introduction

In this chapter, we explore the relationship between pattern geometry and the drying and sintering processes in inkjet-printed electronics, specifically focusing on its impact on the electrical resistivity of silver nanoparticle-based patterns. The drying step is a critical phase in the fabrication of printed devices and circuits, as it directly influences the final electrical properties of the printed patterns. We investigate how different pattern geometries, characterized by varying local densities and numbers of corners, affect the drying process and, consequently, the electrical resistivity of the printed patterns.

To systematically study this phenomenon, we have selected a set of line patterns with distinct geometries, including square wave shapes, wide and narrow U shapes, straight lines, and spirals. Despite having the same length and width, these patterns exhibit different local densities and numbers of corners, which are expected to influence the drying behavior. By keeping the total amount of silver ink and linewidth constant across all patterns, we ensure that any observed

differences in resistivity are attributable solely to the pattern geometry rather than variations in ink quantity or trace thickness.

In addition to the investigation of pattern-dependent drying, this chapter also introduces the application of the frequency-domain thermoreflectance (FDTR) method for tracking the resistivity variation within different patterns. The FDTR method, a non-contact optical technique, enables the detailed mapping of thermal properties at the microscale, which can be correlated with resistivity variations in printed patterns. By employing the FDTR method, we aim to gain deeper insights into the resistivity distribution within the spiral, narrow U, and square wave patterns and individual, corner and center electrodes of a 49 electrode array, and identify areas of non-uniformity.

4.2 Drying and Sintering of Complex Patterns

During the drying step, the solvent's vapor density is higher around patterns characterized by increased local pattern density. In contrast, during the subsequent sintering step, there is a higher temperature rise for higher local pattern density, as schematically represented in Figure 4-1.

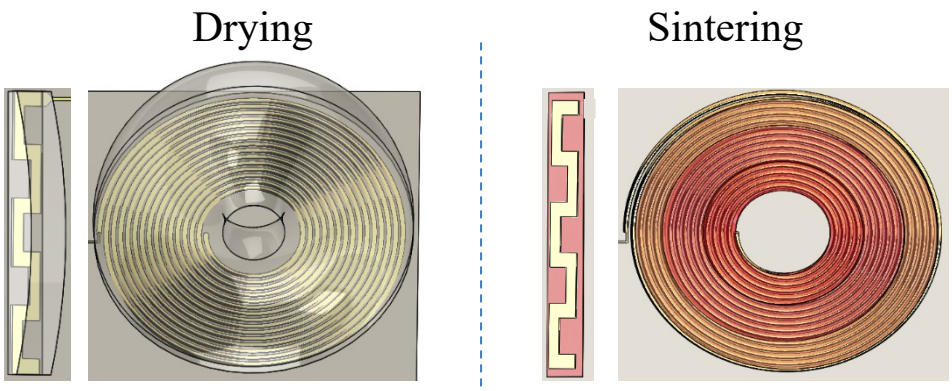

Figure 4-1 a) On the left, two inkjet printed shapes are shown during the drying step, with the spiral exhibiting a denser pattern and, consequently, a higher vapor density compared to the square wave, which has a less dense pattern and lower vapor density. This visual representation makes it evident how pattern density influences vapor density during drying. On the right, we depict both shapes during the sintering step. Here, the denser pattern of the spiral results in a higher temperature at the center and lower temperature at the outer part of the shape. In contrast, the square wave shape exhibits a more uniform temperature distribution during IPL sintering. This visualization effectively highlights how differences in pattern density impact temperature distribution during the sintering process.

The printed complex line patterns are shown in Figure 4-2 (a) This elevated temperature leads to a more substantial reduction in resistance, contributing to a higher resistance reduction factor compared to patterns with lower local density geometries, as depicted in Figure 4-2 (b).The printed patterns are dried at 60 °C for 25 minutes and IPL sintered with 15 J/cm^2. All the shapes are printed with the same total amount of silver ink, which is 1,288 drops, and the same linewidth. By

controlling the total amount of silver ink (1,288 drops) and maintaining the same linewidth, we ensured that variations in ink quantity per unit length and trace thickness as well as overall trace length were not contributing factors to the observed resistance differences between different shapes. The only difference between the patterns is the number of corners and the local density of the pattern. To calculate resistivity from resistance measurements for the different patterns, and to account for the shape of the patterns including corners, microscope images of the printed patterns were imported into COMSOL Multiphysics with the average thickness of each pattern averaged over different locations obtained from profilometry (shown in Figure 4-3), and the current and voltage distributions were calculated. The results show a clear trend of increasing resistivity after drying with increasing pattern density in Figure 4-2 (b). The spiral design with the closest printed features, i.e. adjacent lines, shows the highest resistivity after drying compared to other shapes (57% larger than the line shape with the lowest density). The wide U shape and narrow U shape are two examples of the same fundamental shape to study the effect of pattern density. The narrow U shape shows a higher resistivity after drying compared to the wide U shape (26.8% higher).

After IPL sintering, the spiral design with the highest local pattern density shows the highest resistivity reduction by a factor of 2.47 but its resistivity after sintering is still 29.4% times larger than the line shape. These experiments show that drying is dependent on the pattern geometry and compact designs with small gap distances dry more slowly than less dense designs resulting in a

higher resistivity for the same drying time. Conversely, after IPL sintering, compact designs with small gap distances show a larger resistivity reduction factor than less dense designs due to the more concentrated temperature distribution over the designs with denser local pattern density.

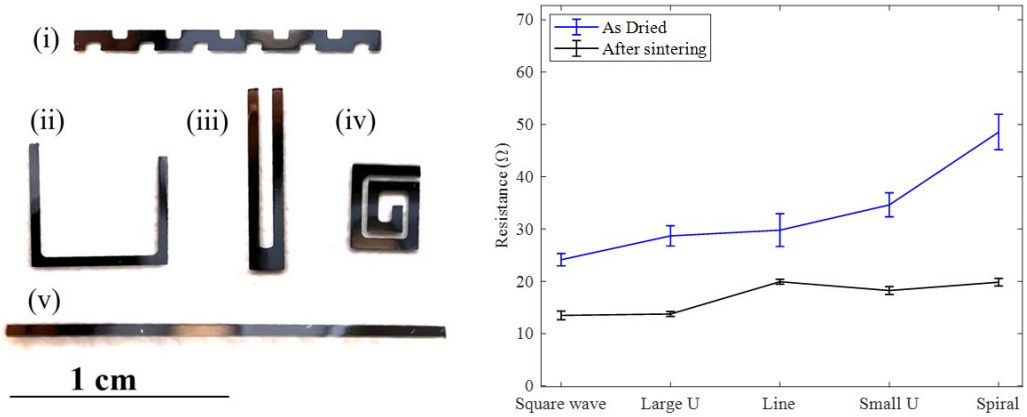

Figure 4-2 . a) Different pattern geometries that were studied after drying and sintering: (i) square wave, (ii) wide U shape, (iii) narrow U shape, (iv) spiral pattern, and (v) straight line. b) Resistivity of these patterns after drying and sintering, which shows an increasing trend from line to spiral pattern.

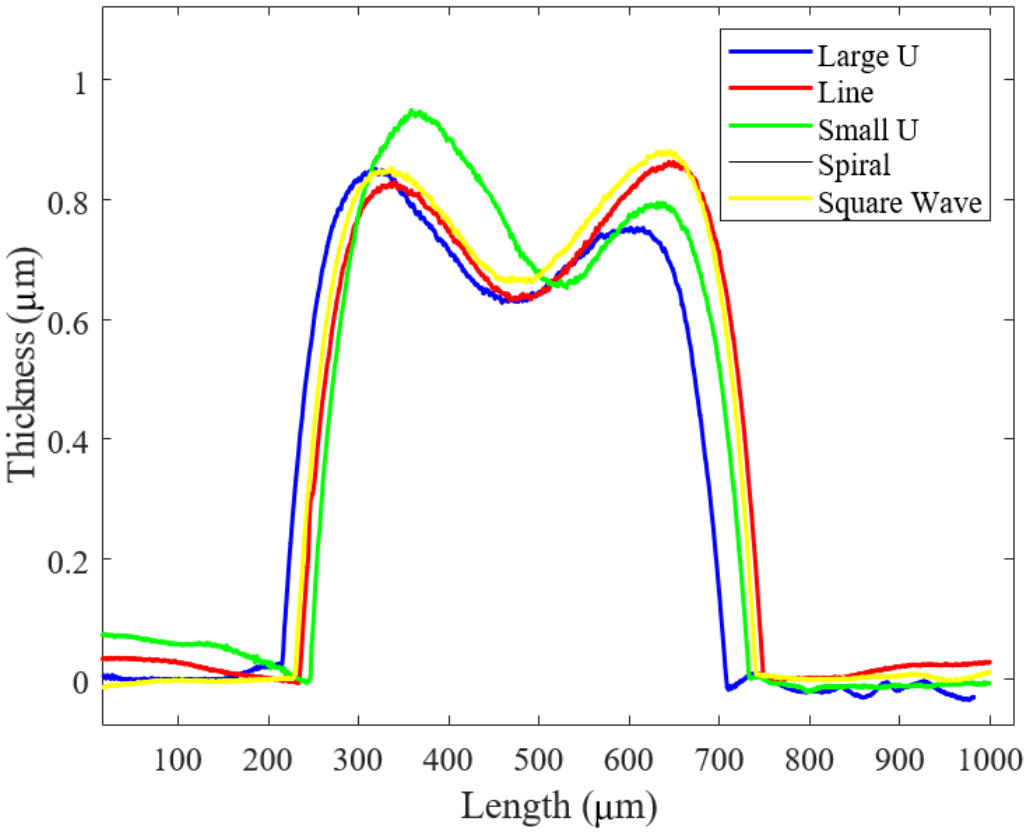

Figure 4-3 The thickness profile of complex designs (wide U, line, narrow U, spiral, square wave).

4.3 Local Resistivity Measurements at Discrete Points

The investigation of printed complex patterns reveals that variations in electrical resistivity are not exclusive to specific forms of printed electrodes, such as electrode arrays, but rather depend on the overall pattern density. Additionally, it has been observed that IPL sintering itself can introduce some degree of non-uniform resistivity, a factor for circuit designers to consider. However, traditional methods like the four-point probe VDP measurement are inadequate for accurately tracking resistivity variations within a complex pattern. Consequently, the focus shifts to FDTR as a more effective technique for this purpose.

FDTR is a non-contact optical method that measures the thermal properties of materials with high spatial resolution. It is particularly suited for evaluating the thermal conductivity of thin films and nanostructured materials. In the context of printed electronics, FDTR can be instrumental in detecting resistivity variations within a pattern by measuring the thermal conductivity. Since electrical conductivity is closely related to thermal conductivity through the Wiedemann-Franz law [77], FDTR provides a unique approach to assess the electrical behavior of printed patterns indirectly. By employing FDTR, we can gain a deeper understanding of how resistivity variations manifest within different designs, enabling more precise control and optimization of printed electronic circuits. This approach not only enhances the accuracy of resistivity measurements but

also offers valuable insights for improving the reliability and performance of printed electronic devices. Here, in equation (4.1), the resistivity is correlated with in-plane thermal conductivity using Wiedemann-Franz law, where k is thermal conductivity, σ is electrical conductivity from sheet resistance, T is room temperature, and L is the Lorentz number, which is 2.37 x 10^{-8} WΩ/K^2 for silver.

$$\sigma = \frac{1}{\rho} = \frac{k}{L \times T} \tag{4.1}$$

The FDTR technique is employed here to examine the thermal and electrical conductivities of spiral, narrow U-shaped, and square wave patterns post-drying These patterns were sintered using IPL sintering with 20 pulses at an energy density of 22.5 J/cm². Figure 4-4 depicts the thermal phase as a function of frequency across four distinct regions of the spiral pattern, progressing from the periphery toward the center. The presented data indicates that the peripheral segments of the spiral pattern exhibit greater electrical and thermal conductivity compared to its central region. Specifically, the FDTR measurements suggest that the conductivity increases by a factor of approximately 2.34 from the innermost point to the outer segments, as demonstrated in Figure 4-4 (a-d). This increase in conductivity from the center to the edges is attributed to pattern density. In the analysis of the pulse wave pattern, FDTR measurements were systematically conducted at three strategic locations: two along the edges, representing the outer portions, and one at the center of

the pattern. The findings, illustrated in Figure 4-5 (a-c), reveal that the resistivity at the outer points are 14.07±1.32 μΩ.cm and 15.85±0.93 μΩ.cm.

In contrast, the central point exhibits a higher resistivity of 22.84±0.86 μΩ.cm. This central resistivity surpasses that of the outer regions by a factor of 1.53±0.1, indicating an increase toward the center of the pattern.Furthermore, the narrow U-shaped pattern was subjected to FDTR analysis at four points, chosen to represent a gradient from the pattern's higher density region at the center to the lower density at the base and top. The results, detailed in Figure 4-6, confirm a consistent trend correlating pattern density with resistivity. Specifically, the resistivity at the center of the U-shaped pattern is measured at 16.11±1.75 μΩ.cm, diminishing to 9.79±0.89 μΩ.cm at the pattern's lower part. This represents a resistivity variance factor of approximately 1.67±0.33. These observations are crucial as they clearly demonstrate the influence of pattern geometry on the resistivity of sintered materials. The systematic increase in resistivity from the outer edges to the center in all patterns indicates that even after IPL sintering, the variations in pattern density can cause a resistivity variation within the printed patterns.

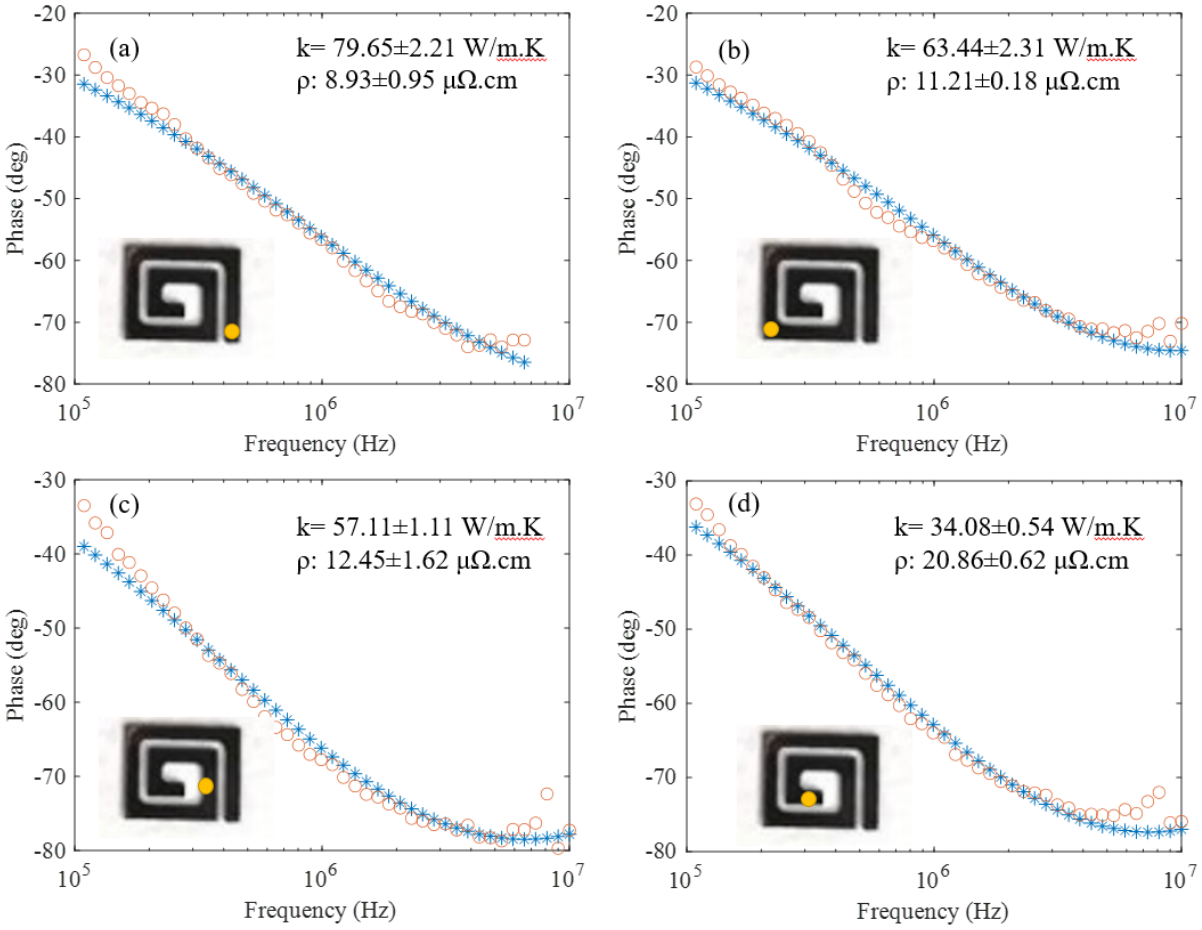

Figure 4-4 Thermal phase vs. frequency for a spiral pattern from outer to inner parts. The blue line is a fit using a diffusive thermal model, illustrating good agreement with the measured data.

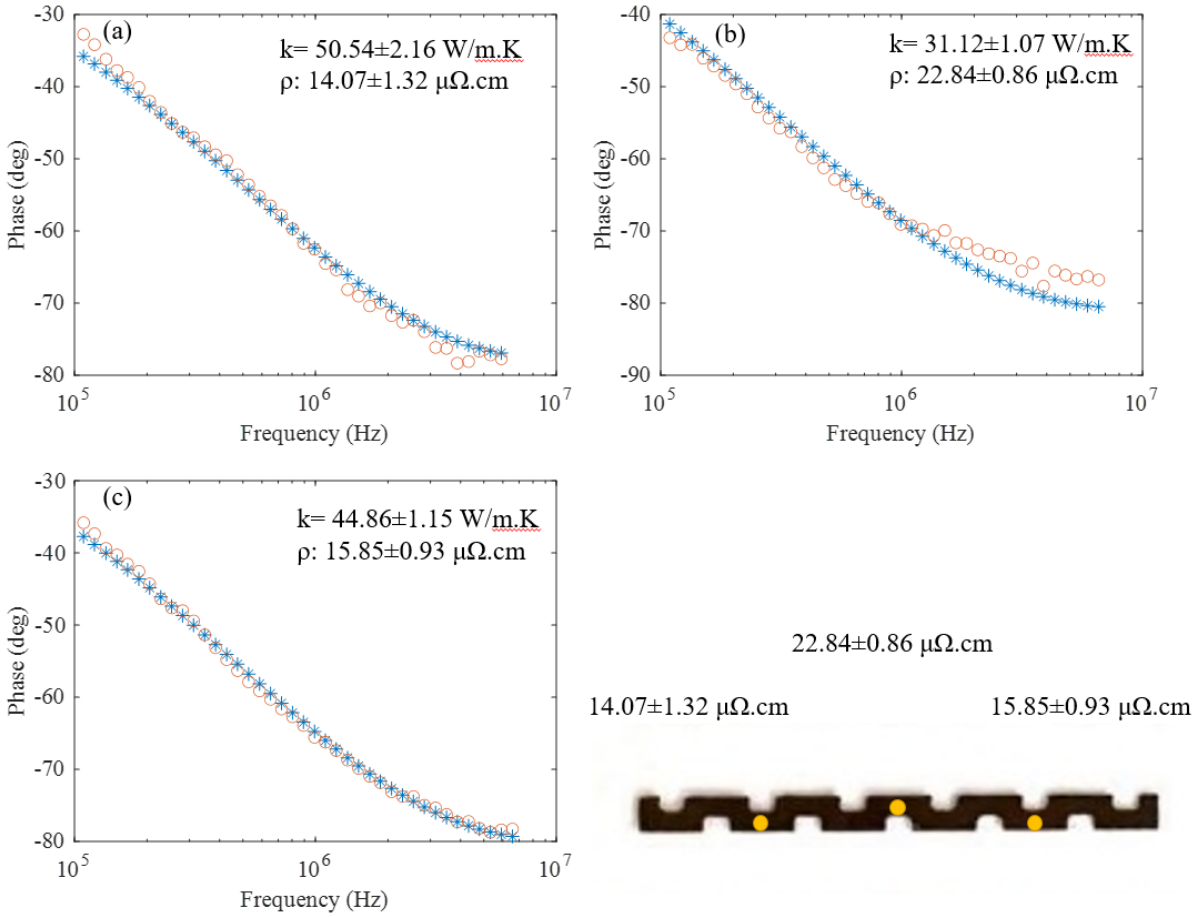

Figure 4-5 Thermal phase vs. frequency for a spiral pattern from outer to inner parts. The blue line is a fit using a diffusive thermal model, illustrating good agreement with the measured data.

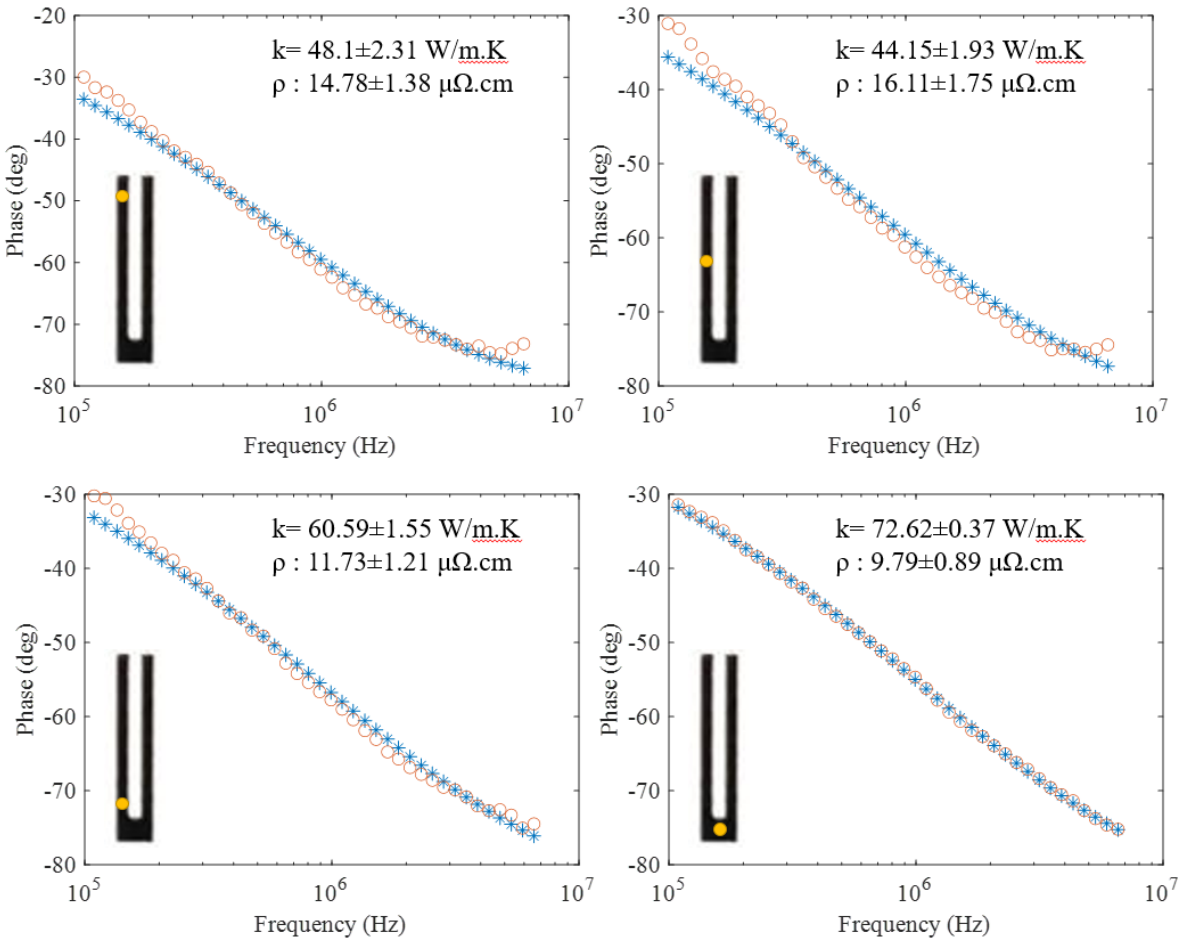

Figure 4-6 Thermal phase vs. frequency for a spiral pattern from outer to inner parts. The blue line is a fit using a diffusive thermal model, illustrating good agreement with the measured datai.

To further study this effect, a 7x7 electrode array was fabricated via inkjet printing on a glass substrate, and subsequent thermal sintering was conducted at 60 °C for 3 hours. The resistivity distribution within electrodes in the array was evaluated employing the FDTR technique, traversing from one corner to the opposing one (shown in Figure 4-7 (a)), bisecting through the center electrode in the array. This analysis aimed to discern the resistivity variations not only within individual electrodes but also among the electrodes comprising the array.

Figure 4-7 (b-d) illustrates the resistivity profile of an isolated individual electrode situated away from the array. The measurement reveals a significant gradient in resistivity, with an initial value of 11.48±0.87 μΩ·cm at one corner that increases by 46.5% towards the center, reaching 16.82±0.87 μΩ·cm. The resistivity subsequently decreases to 10.87±0.63 μΩ·cm towards the opposite corner. This bidirectional trend of resistivity—ascending towards the center and diminishing as it extends to the opposing corner mirrors the behavior observed within larger electrode arrays, wherein corner electrodes demonstrate lower resistivity relative to the center electrode.

Further, resistivity measurements for a corner electrode, represented in Figure 4-7 (c), exhibit a substantial increment from the outermost corner of the electrode, with an initial reading of 7.2±0.92 μΩ·cm, to a peak of 16.7±0.25 μΩ·cm as it approaches the opposing corner—a rise of

approximately 132%. This variation within a single corner electrode is analogous to the resistivity variation from the array's periphery towards the center. The center electrode of the array exhibits a similar, albeit more pronounced, pattern compared to the individual electrode. Starting at 7.71±0.9 μΩ·cm at the periphery, resistivity increases by 229% to a peak of 25.36±0.7 μΩ·cm at the center. This marked variation underscores the significant spatial resistivity variation across the electrode array.

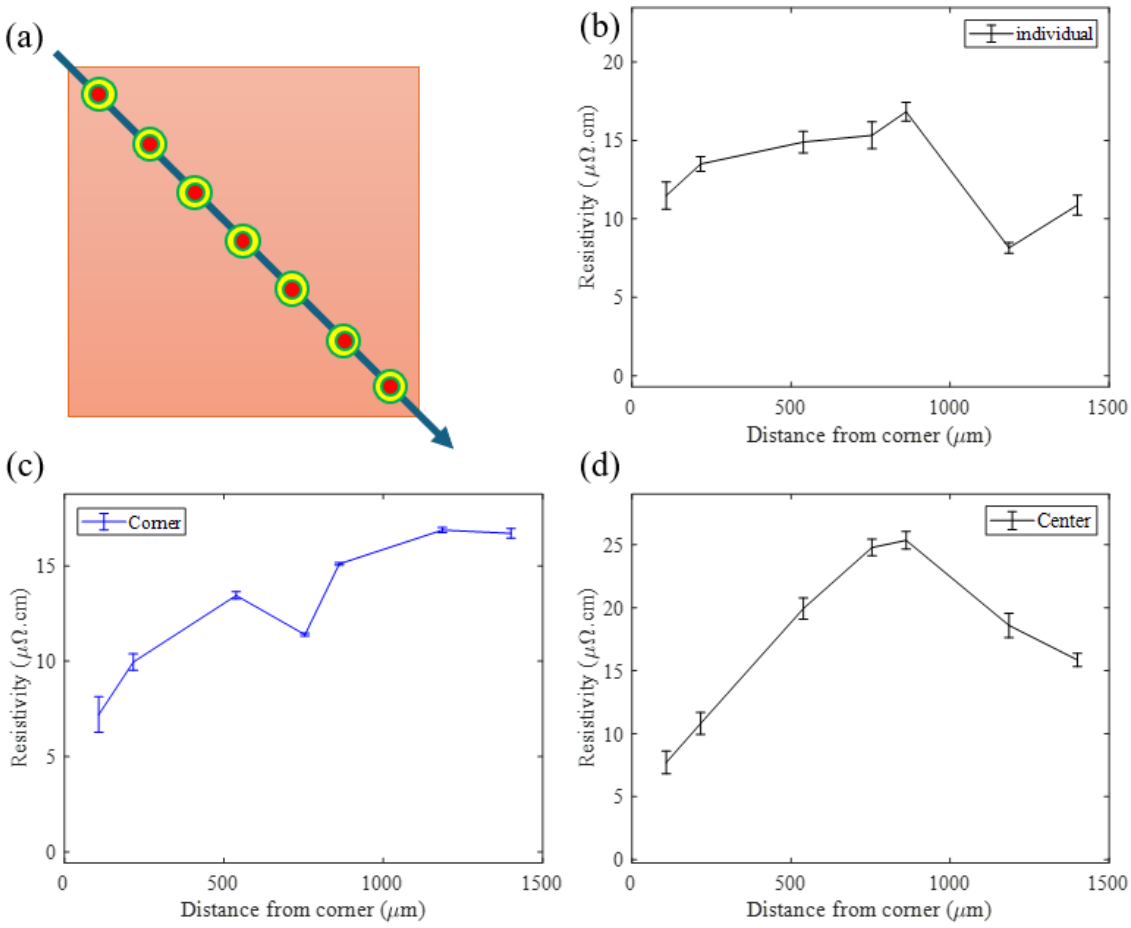

Figure 4-7 Resistivity measurement using FDTR within a square electrode, a) the schematic path of FDTR measurements, b) resistivity variation within an individual electrode, c) corner of an electrode array, and d) center of an array (the error bar represents standard deviation for 5 samples)

4.4 Conclusions

In conclusion, this chapter has studied the relationship between pattern geometry, drying, and sintering processes and their impact on the electrical resistivity of inkjet-printed silver nanoparticle-based patterns. The systematic examination of various pattern geometries, such as square wave shapes, U shapes, and spirals, has demonstrated that local densities and the number of corners significantly influence both drying behaviors and resistivity outcomes. It has been established that pattern complexity and density are defining the effectiveness of the drying process, subsequently affecting the sintering efficacy and the electrical resistivity.

The utilization of the FDTR method has been applied in providing a high-resolution mapping of resistivity variations within patterns, offering a powerful tool for analyzing the behaviors of these complex geometries. Through FDTR measurements, it has been possible to correlate increased pattern densities with slower drying rates and higher resistivity post-drying, as well as with greater reductions in resistivity following IPL sintering. The findings presented in this chapter offer vital insights for optimizing fabrication processes. It has been shown that despite uniform ink deposition and linewidth, patterns' inherent geometric characteristics affect drying and sintering behaviors, necessitating careful consideration during the design and post-treatment phases of electronic devices. This understanding allows for the enhancement of electrical performance and

reliability through pattern design and process parameter optimization. Moving forward, these results show a limitation of sintering methods that uniformly sinter patterns. To have better control over patterns with different resistivity variations, selective sintering is required. In the next chapter, a selective laser sintering is studied as a promising method for uniform resistivity of inkjet printed electrodes on a glass substrate.

Chapter 5 Laser Sintering

5.1 Introduction

The relevance of Chapter 5 to the overall theme of this thesis is the exploration of laser sintering methods, specifically using diode and CO_2 lasers, to enhance resistivity uniformity across printed electrodes. Laser sintering allows for selective and precise adjustments of parameters, critical for achieving uniform sintering without the risk of oversintering. This chapter aims to optimize laser sintering settings such as power and scan rate based on the spatial variations in pattern density of printed electrodes. In the previous chapters, conventional thermal sintering and IPL sintering were studied, and their limitations were highlighted in controlling localized heating and achieving uniform resistivity. The focus in this chapter shifts to a detailed examination of diode and CO_2 laser sintering. Through experimental analysis, including four-point probe measurements on electrode arrays and FDTR assessments on spiral configurations, this chapter demonstrates how tailored adjustments to laser parameters can reduce resistivity variations, thereby enhancing the performance of printed electronic components.

5.2 Diode Laser

To determine the optimal settings for a 5 W continuous diode laser (LA5-808) from Hyrel 3D (Atlanta, GA), experiments were conducted on square-shaped individual electrodes (1 mm × 1 mm) printed on a glass substrate. These electrodes were pre-dried at 60 °C for 30 minutes to prepare them for sintering. The sintering process was controlled using G-code to guide multiple parallel line scans over the electrode area in vector mode. The diode laser, with a wavelength of 808 nm, a spot size of approximately 250 μm and raster spacing of 100 μm, was focused from a distance of about 100 mm. During the experiments, the laser operated at 100% power with varying scan rates from 2 to 60 mm min^{-1} (shown in Figure 5-1) To explore efficient sintering times while achieving low resistivity, the number of sintering passes per electrode was varied between 1 to 10. Pulse spacing orthogonal to the laser scan direction was maintained at 10 μm. All experiments were conducted under ambient conditions. The resistivity outcomes of these square-shaped electrodes at different scan rates and number of passes are illustrated in the Figure 5-2.

An individual electrode, post-drying, exhibits significantly higher resistivity compared to one that has undergone diode laser sintering. For a scan rate of 2 $mm.min^{-1}$ with 10 scans, the reduction factor is 16.39. At a scan rate of 60 $mm.min^{-1}$ with 3 scans, the reduction factor is 8.62. This data

indicates that lower scan rates combined with a higher number of scans result in a greater reduction in resistivity but require increased sintering time.

Furthermore, the impact of the number of scans on resistivity becomes more pronounced at higher scan rates. For instance, at a scan rate of 60 $mm.min^{-1}$, a single pass results in a resistivity of 8.12 μΩ.cm, which decreases to 7.09 μΩ.cm after three scans—a 14.5% reduction. In contrast, at the slower scan rate of 2 $mm.min^{-1}$, three scans yield only a 5.3% reduction in resistivity compared to one scan. These observations suggest that the effectiveness of the 5W diode laser is constrained in the sintering of silver-based printed patterns, pointing to its limitations in achieving optimal sintering outcomes without significant time investment. To enhance the sintering energy while maintaining selectivity across different parts of a printed pattern, the use of a higher power CO_2 laser sintering was investigated.

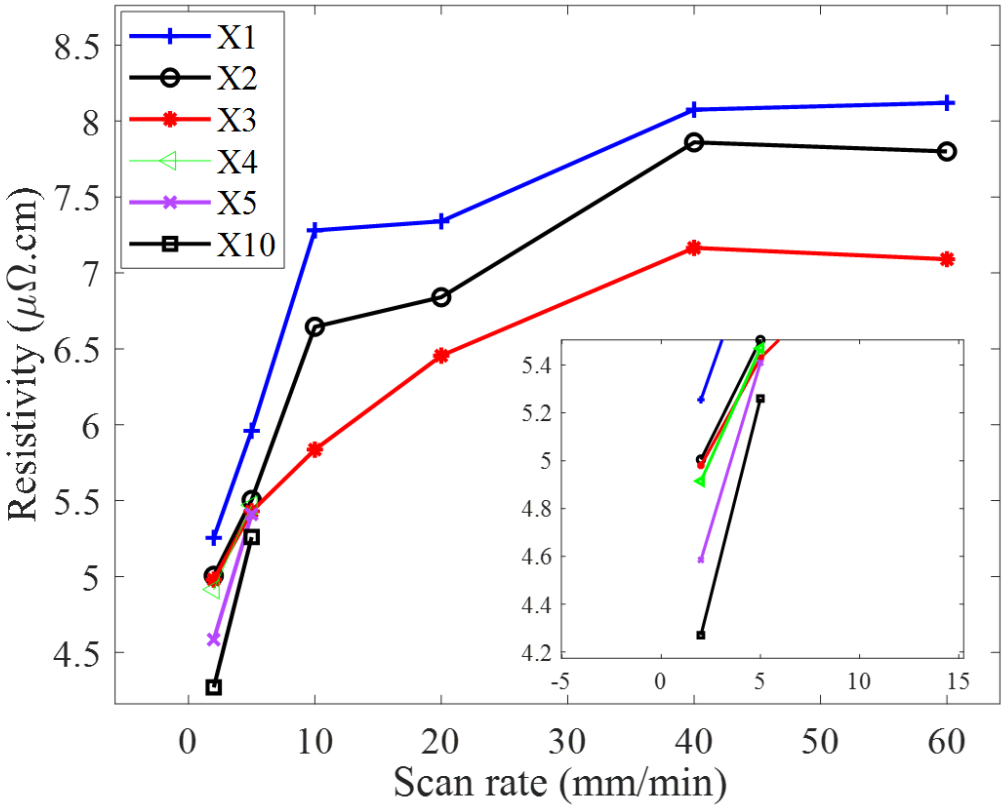

Figure 5-1 Resistivity of square-shaped electrodes versus scan rate, using a diode laser at constant 100% power (5 W).

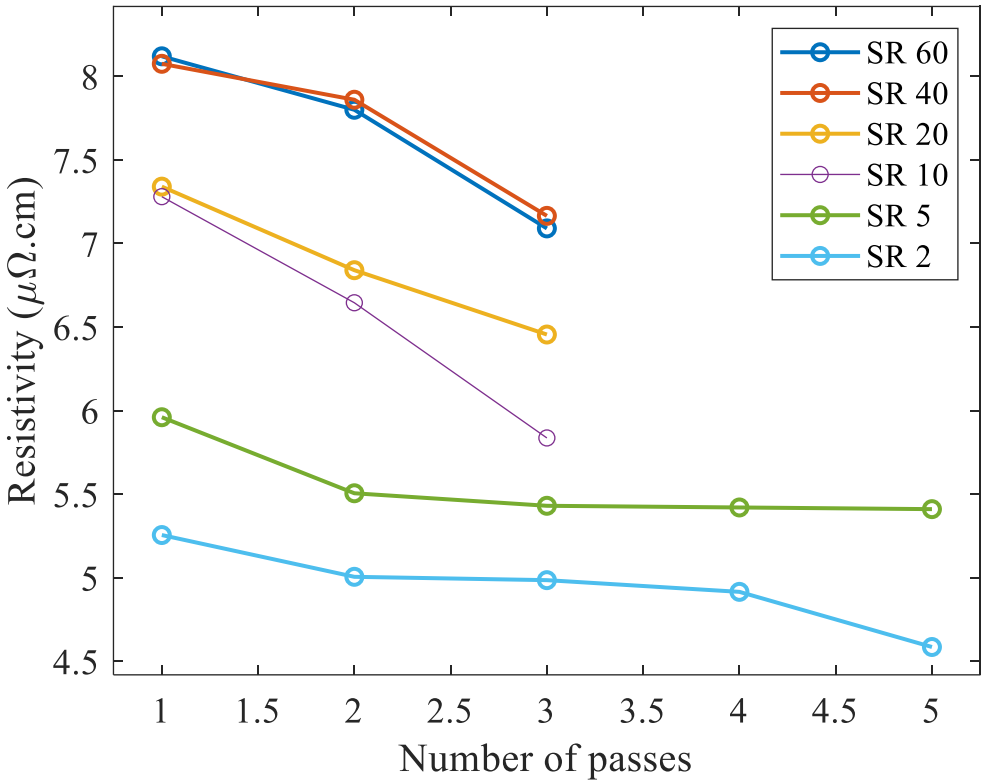

Figure 5-2 Resistivity of square-shaped electrodes versus the number of passes, using a diode laser at constant 100% power (5 W).

5.3 CO_2 Laser Sintering

For the sintering process of inkjet-printed electrode arrays, we utilized a 40W CO_2 laser cutter (Hydra 16A) with a spot size of 400 µm and raster spacing of 100 µm from Hyrel 3D, (Atlanta,

GA). This system was operated in vector mode employing line and spiral sintering patterns. To optimize the scan rate and power settings, preliminary tests were conducted on individual electrodes. The laser power was set at a constant 33%, and four different scan rates ranging from 1600 $mm.min^{-1}$ to 1900 $mm.min^{-1}$ were evaluated. Given the electrodes' dimensions of approximately 1 mm by 1 mm, and a laser spot size of 400 μm at a focal distance of 8 mm, the pulse spacing orthogonal to the laser scan direction was maintained at 100 μm. Each electrode underwent ten passes to ensure complete coverage.

Our findings indicate a significant variation in resistivity dependent on the scan rate. Resistivity decreased from 22.05 μΩ·cm at the lowest scan rate of 1600 $mm.min^{-1}$, to a minimum of 1.72 μΩ·cm at 1800 $mm.min^{-1}$. This suggests that lower scan rates lead to oversintering, while an increase in scan rate to 1900 $mm.min^{-1}$ resulted in insufficient energy density for effective sintering. This experimental setup established an optimal window for the power and scan rate parameters, crucial for achieving the lowest resistivity in the electrode arrays.

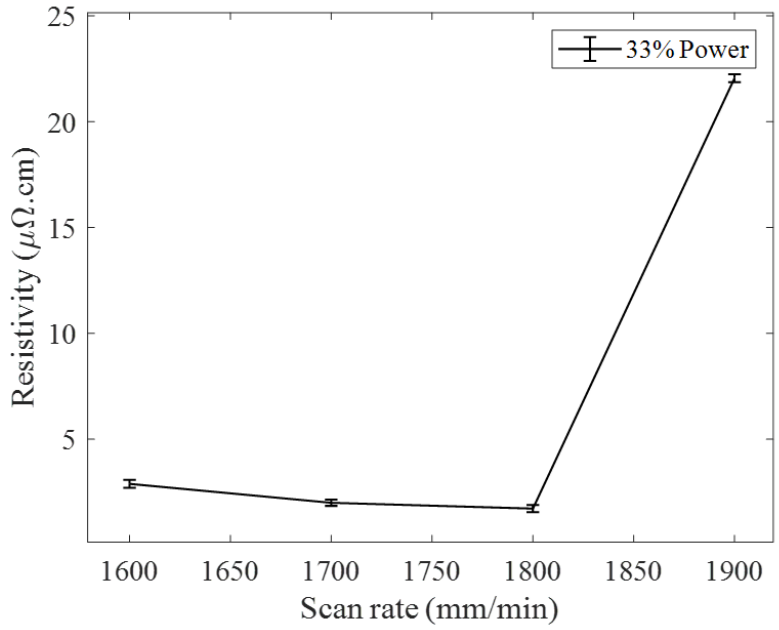

Figure 5-3 Variation in resistivity with scan rate for a CO_2 laser operating at a constant power of 33%.

In the optimization of the sintering process for 7x7 electrode arrays, we employed the previously developed line pattern, programmed through G-code, with a consistently maintained scan rate of 1800 $mm.min^{-1}$. The laser power was varied within a range from 30% to 35% shown in Figure 5-4. A significant observation was a 25.7% decrease in resistivity among the corner electrodes as the power was increased from 30% to 34%, yielding a resistivity of 1.73 μΩ·cm. This conductivity approaches 95% of the value of bulk silver, which stands at 1.65 μΩ·cm. However, a further increase in power to 35% resulted in a 9% increase in resistivity, indicative of oversintering. The resistivity variation between corner electrode and center electrode after

sintering with parallel line method is around 70%, which is worse than thermal and IPL sintering with this laser sintering scheme. Although laser sintering is intended to improve resistivity and uniformity, the method of sintering plays a crucial role. Specifically, the parallel line sintering method has proven to be less effective in enhancing uniformity. This data led us to infer that the optimal laser power to prevent excessive resistivity while maintaining efficient sintering lies close to 34%.

In contrast, the center electrode displayed a different response to the same power adjustments. Their resistivity decreased from 4.84 μΩ·cm to 2.96 μΩ·cm—a reduction of approximately 29%—as the power increased from 30% to 34%. Moreover, a subsequent increase in power to 35% still resulted in a decrease in resistivity for the center electrode, underscoring an insufficient sintering power for the central region relative to the peripheral areas, which is also obvious in the optical micrograph, where the center shows a darker color compared to the corners (as an inset in Figure 5-4) of the sintered sample at a power of 34%. This variation underscores the inherent challenge of achieving uniform energy distribution across the electrode array with uniform adjustments in power and scan rate settings.

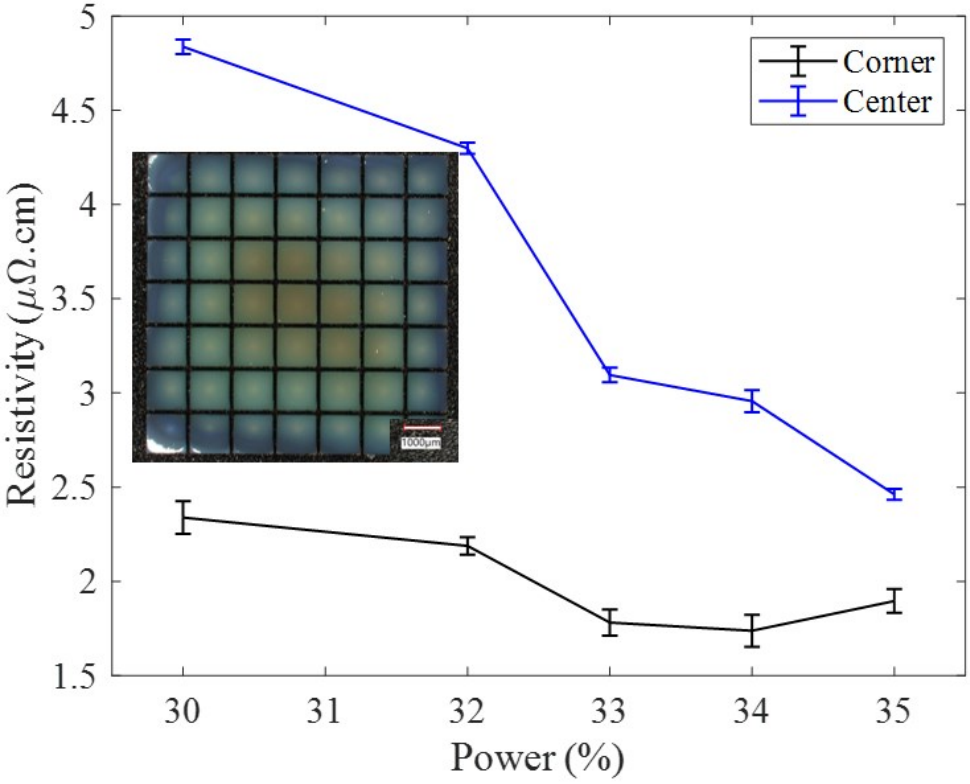

Figure 5-4 Resistivity variation with power at a fixed 1800 mm.min^{-1} scan rate for corner and center electrode of a 7x7 electrode array.

To address this challenge and enhance uniformity in sintering results, a novel approach involving a spiral G-code design was implemented. This method strategically scans from the outer electrodes inward, ending at the central electrode, while adapting the scan rates and power settings according to specific positional requirements within the array. Specifically, the initial two loops

of the electrode array are sintered at a higher scan rate of 1800 $mm.min^{-1}$ as they have lower resistivity and lower energy density is required to sinter, and subsequently, the remaining electrodes, including the center, are treated at a reduced scan rate of 900 $mm.min^{-1}$. To further tailor the energy delivery, four distinct power settings ranging from 50% to 80% are applied, reflecting the varied energy requirements across different sections of the array. In the pursuit of achieving uniform resistivity across a 7x7 electrode array during CO_2 laser sintering, varying power settings were examined. Initial tests at a 50% power setting revealed a substantial resistivity variation of approximately 26.5% between the corner and center electrodes, indicating that this power level was insufficient for uniform sintering across the array. By increasing the power to 60%, the variation in resistivity notably decreased to 3.4%. However, this condition still resulted in an overall higher resistivity compared to other sintering methods such as thermal and IPL sintering, suggesting that while the uniformity improved, the absolute resistivity values were not optimal.

Further adjustments were made by increasing the power to 70% (power density of 2.229×10^7 W/cm^2), which effectively reduced both the absolute resistivity values and the variation between the corner and center electrodes to 1.84 μΩ·cm and 1.9 μΩ·cm, respectively, with a closely matched variation of 3.2%. This setting approached an ideal balance between uniformity and low resistivity, demonstrating the effectiveness of precise power modulation. Exploring the effects of

an even higher power setting, the power was increased to 80%. This adjustment, however, led to an undesirable increase in resistivity for both the center and corner electrodes, a clear indication of oversintering. These findings underscore the critical balance required in power settings to optimize sintering outcomes without compromising the structural integrity of the electrodes.

This systematic control of power and scan rate at different locations within the electrode array represents a novel approach in the field of CO_2 laser sintering of printed electronics. It is the first time such a differentiated strategy has been applied, aiming to simultaneously optimize both resistivity and uniformity across an electrode array. This innovation not only enhances the functional attributes of the electrodes but also contributes significantly to the advancement of fabrication techniques in printed electronics.

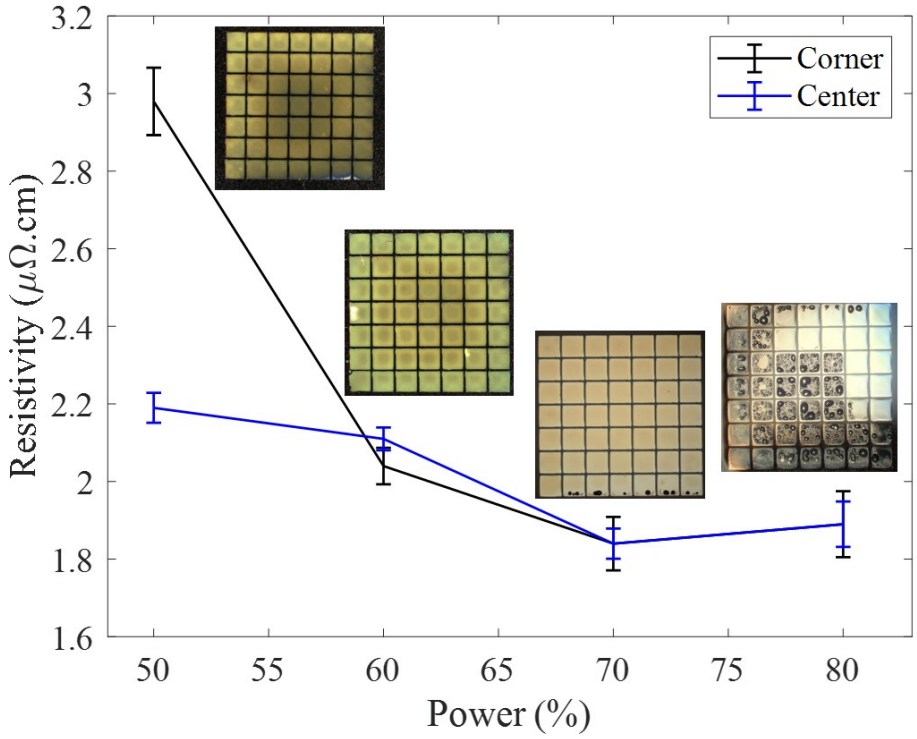

Figure 5-5 Resistivity variation with power (20, 24, 28, and 32 W) during CO_2 laser sintering of a 7x7 electrode array using a spiral sintering pattern with two different scan rates (half way with 1800 and the rest 900 $mm.min^{-1}$).

5.4 Conclusions

In this chapter, we investigated selective sintering methods employing diode and CO_2 lasers to optimize resistivity across electrode arrays, aiming to minimize variations in resistivity between corner and center electrodes. Our initial experiments with a diode laser, which operates at a low power of 5W and power density of 10185 W/cm^2, demonstrated its inadequacy for effective sintering. Even with a reduced scan rate of 2 mm.min^{-1}, the resistivity achieved was approximately 4.27 μΩ·cm for individual electrodes—about 2.6 times higher than that of bulk silver. Given these results, we focused on CO_2 laser sintering with a higher power density (15912.93, 19095.5, 22278.10, and 25460.68 W/cm^2), testing two different sintering patterns across 7x7 electrode arrays: parallel lines and a spiral shape. The parallel line approach, even when optimized for scan rate and power, resulted in significant resistivity variation—approximately 70% between the corner and center electrodes. In contrast, the spiral pattern approach, starting from the outer electrodes at a higher scan rate of 1800 mm.min^{-1} and decreasing to 900 mm.min^{-1} towards the center, proved more effective. This method, at a constant power setting of 70%, not only achieved the lowest observed resistivity of 1.84 μΩ·cm but also reduced the resistivity variation to 3.2%. These findings underscore the importance of the spiral sintering pattern with a variable scan rate in achieving uniform sintering across electrode arrays. This approach significantly enhances the

consistency of electrical properties throughout the array, making it a promising technique for optimizing the performance of printed electronics.

Chapter 6 Conclusions and Future Works

6.1 Conclusions

The primary focus of this thesis is to achieve low and uniform resistivity in inkjet-printed silver nanoparticle patterns. Resistivity uniformity in adjacent printed patterns is crucial. However, non-uniform drying of printed patterns with less than 1 mm gap distance due to high vapor pressure density in higher pattern densities, and lower vapor pressure density around lower pattern densities, poses challenges. This drying inconsistency led to resistivity variations across patterns. Non-uniform drying and resistivity variation post-drying were systematically studied across different electrode arrays, varying in the number of electrodes and gap distances. The sooner an electrode dries, the lower resistivity it achieves. In a 7x7 electrode array with a 250 μm gap distance, significant resistivity differences were noted between corner and center electrodes after drying at 60 °C for 30 minutes. The center electrode displayed a resistivity (1433 ± 208 μΩ.cm) 21 times larger than individual electrodes (66.19 ± 4.27 μΩ.cm) and 19 times larger than corner electrodes (71.99 ± 4.33 μΩ.cm).

The electrical resistivity of a 7x7 electrode array with a 100 μm gap distance was also sintered using a hot plate at varying temperatures (60 °C–160 °C) with a 30-minute sintering time. Resistivity measurements across different electrode locations (individual, corner, and center) post-thermal sintering showed improved resistivity with increasing sintering temperature and reduced variation from the center to corners compared to pre-sintering. After sintering at 160 °C, a 17% resistivity variation remained between center and corner, and 27% between individual and center.

IPL sintering was applied as a rapid method where the light from a xenon flash lamp is selectively absorbed by silver, preventing substrate heating. However, the heat distribution was non-uniform, resulting in higher temperatures around the center electrode than at the corners. This phenomenon was also simulated using COMSOL, illustrating temperature distribution over electrode arrays with varying gap distances. Printed electrodes with smaller gap distances showed higher resistivity after drying than those with larger gaps, but IPL temperature distribution led to a higher resistivity reduction factor for smaller gaps. Additionally, electrodes with smaller gaps oversintered at lower energy densities compared to larger gaps due to the higher and longer-lasting temperature differences.

Selective sintering using a laser was identified as a solution, providing location control with better resolution. After optimizing CO_2 laser sintering parameters, the lowest electrical resistivity was achieved in both corner and center electrodes with only 3.2% variation (1.84 and 1.9 μΩ.cm, respectively).

In summary, non-uniform drying and resistivity variations were systematically analyzed, and selective laser sintering proved to be a promising method for reducing resistivity and ensuring uniformity. In Table 6-1 an overview of different sintering methods and the resistivity variations between the corners and the center for each method is presented. The analysis highlights that the best resistivity and minimal variation are achieved using laser sintering with a power of 28 W. The optimal sintering pattern follows a spiral shape, with the first half of the path sintered at a speed of 1800 $mm.min^{-1}$ and the second half at 900 $mm.min^{-1}$. This method demonstrates superior performance compared to other techniques due to a higher power density compare to the diode laser.

Table 6-1 Overview of different sintering methods results for a 7x7 electrode array with 100 μm gap distance.

	Thermal Sintering	IPL Sintering (510000 W/cm^2)	Laser Sintering (2.229 × 10^7 W/cm^2)
Individual	5.35 μΩ·cm	1.84 μΩ·cm	1.73 μΩ·cm
Corner	5.73 μΩ·cm	2.05 μΩ·cm	1.84 μΩ·cm
Center	6.51 μΩ·cm	2.16 μΩ·cm	1.9 μΩ·cm
Variation (Corner to Center)	17%	5.4%	3.2%
Variation (Center to Individual)	27%	17.4%	9.8%

6.2 Future Work

Looking forward, there is a wealth of opportunity to expand on the foundations laid by this research. One promising direction is the development of predictive models for printing parameters such as gap distance between printed features and pattern density. Such models could significantly

enhance the ability to predict optimal sintering parameters that achieve the lowest possible resistivity, tailored to specific design requirements.

An AI-based predictive model could estimate the resistivity of inkjet-printed designs based on various parameters, including design, drying, and sintering conditions. Future research in this direction could empower circuit designers to optimize printed circuits effectively, considering parameters such as feature spacing, shape, gap distances, and sintering settings, ensuring the desired electrical performance in various printed electronic applications and advancing the field of printed electronics. Simulating the drying process of inkjet-printed patterns could provide valuable insights into how different designs affect evaporation rates and vapor pressure. Future work could also explore convection drying and the effects of airflow during drying to control resistivity variations.

Furthermore, investigating the impact of pattern density on specific applications, such as antennas, could yield insights into the performance enhancements and limitations imposed by current fabrication techniques. This research would extend the practical applications of printed electronics and contribute to a deeper theoretical understanding of material science in thin-film technology. In addition, further refinement of sintering parameters, particularly with selective laser sintering, can reduce resistivity variations across different patterns. Tailoring sintering conditions

to specific design requirements will enable the achievement of the lowest possible resistivity. These future research directions will empower the field of printed electronics by providing circuit designers with advanced tools and methodologies to optimize their designs. By considering parameters such as feature spacing, shape, gap distances, and sintering settings, they can ensure optimal electrical performance across a range of printed electronic applications. Ultimately, this will advance the field both theoretically and practically, bridging the gap between fundamental research and industrial application.

References

[1] M. Gao, L. Li, and Y. Song, “Inkjet printing wearable electronic devices,” *J. Mater. Chem. C*, vol. 5, no. 12, pp. 2971–2993, 2017.

[2] G. Grau, “Low-cost fabrication of paper-based systems: Microfluidics, sensors, electronics and deployment,” in *2017 IEEE 60th International Midwest Symposium on Circuits and Systems (MWSCAS)*, 2017, pp. 84–87.

[3] A. Kamyshny and S. Magdassi, “Conductive nanomaterials for printed electronics,” *Small*, vol. 10, no. 17, pp. 3515–3535, 2014.

[4] E. Sowade, H. Kang, K. Y. Mitra, O. J. Weiß, J. Weber, and R. R. Baumann, “Roll-to-roll infrared (IR) drying and sintering of an inkjet-printed silver nanoparticle ink within 1 second,” *J. Mater. Chem. C*, vol. 3, no. 45, pp. 11815–11826, 2015.

[5] S. Chandrasekaran, A. Jayakumar, and R. Velu, “A Comprehensive Review on Printed

Electronics: A Technology Drift towards a Sustainable Future," *Nanomaterials*, vol. 12, no. 23. 2022.

[6] N. Zavanelli and W.-H. Yeo, "Advances in screen printing of conductive nanomaterials for stretchable electronics," *ACS omega*, vol. 6, no. 14, pp. 9344–9351, 2021.

[7] G. Grau and V. Subramanian, "Fully high-speed gravure printed, low-variability, high-performance organic polymer transistors with sub-5 V operation," *Adv. Electron. Mater.*, vol. 2, no. 4, p. 1500328, 2016.

[8] G. Grau, J. Cen, H. Kang, R. Kitsomboonloha, W. J. Scheideler, and V. Subramanian, "Gravure-printed electronics: recent progress in tooling development, understanding of printing physics, and realization of printed devices," *Flex. Print. Electron.*, vol. 1, no. 2, p. 23002, 2016.

[9] H. J. Kwon *et al.*, "Overview of recent progress in electrohydrodynamic jet printing in practical printed electronics: Focus on the variety of printable materials for each component," *Mater. Adv.*, vol. 2, no. 17, pp. 5593–5615, 2021.

[10] G. Cummins and M. P. Y. Desmulliez, "Inkjet printing of conductive materials: a review,"

Circuit world, vol. 38, no. 4, pp. 193–213, 2012.

[11] H. Abdolmaleki, P. Kidmose, and S. Agarwala, "Droplet-Based Techniques for Printing of Functional Inks for Flexible Physical Sensors," *Adv. Mater.*, p. 2006792, 2021.

[12] O. Reynolds, "XXIX. An experimental investigation of the circumstances which determine whether the motion of water shall be direct or sinuous, and of the law of resistance in parallel channels," *Philos. Trans. R. Soc. London*, no. 174, pp. 935–982, 1883.

[13] V. Bergeron, D. Bonn, J. Y. Martin, and L. Vovelle, "Controlling droplet deposition with polymer additives," *Nature*, vol. 405, no. 6788, pp. 772–775, 2000.

[14] G. H. McKinley and M. Renardy, "Wolfgang von ohnesorge," *Phys. Fluids*, vol. 23, no. 12, p. 127101, 2011.

[15] J. E. Fromm, "Numerical calculation of the fluid dynamics of drop-on-demand jets," *IBM J. Res. Dev.*, vol. 28, no. 3, pp. 322–333, 1984.

[16] N. Reis and B. Derby, "Ink jet deposition of ceramic suspensions: Modeling and experiments of droplet formation," *MRS Online Proc. Libr.*, vol. 625, 2000.

[17] D. Jang, D. Kim, and J. Moon, “Influence of fluid physical properties on ink-jet printability.,” *Langmuir*, vol. 25, no. 5, pp. 2629–2635, Mar. 2009.

[18] D. Zhu and M. Wu, “Highly conductive nano-silver circuits by inkjet printing,” *J. Electron. Mater.*, vol. 47, no. 9, pp. 5133–5147, 2018.

[19] D. Soltman and V. Subramanian, “Inkjet-printed line morphologies and temperature control of the coffee ring effect,” *Langmuir*, vol. 24, no. 5, pp. 2224–2231, 2008.

[20] A. L. Yarin, “Drop impact dynamics: splashing, spreading, receding, bouncing…,” *Annu. Rev. Fluid Mech.*, vol. 38, pp. 159–192, 2006.

[21] J.-C. Lin, P. Liatsis, and P. Alexandridis, “Flexible and stretchable electrically conductive polymer materials for physical sensing applications,” *Polym. Rev.*, vol. 63, no. 1, pp. 67–126, 2023.

[22] S. K. Garlapati, M. Divya, B. Breitung, R. Kruk, H. Hahn, and S. Dasgupta, “Printed electronics based on inorganic semiconductors: From processes and materials to devices,” *Adv. Mater.*, vol. 30, no. 40, p. 1707600, 2018.

[23] Y. Z. N. Htwe and M. Mariatti, “Printed graphene and hybrid conductive inks for flexible,

stretchable, and wearable electronics: Progress, opportunities, and challenges," *J. Sci. Adv. Mater. Devices*, vol. 7, no. 2, p. 100435, 2022.

[24] D. Zhao, H. Zhou, Y. Wang, J. Yin, and Y. Huang, "Drop-on-demand (DOD) inkjet dynamics of printing viscoelastic conductive ink," *Addit. Manuf.*, vol. 48, p. 102451, 2021.

[25] H. Shahariar, I. Kim, H. Soewardiman, and J. S. Jur, "Inkjet printing of reactive silver ink on textiles," *ACS Appl. Mater. Interfaces*, vol. 11, no. 6, pp. 6208–6216, 2019.

[26] Y. H. Wang *et al.*, "Printability and electrical conductivity of silver nanoparticle-based conductive inks for inkjet printing," *J. Mater. Sci. Mater. Electron.*, vol. 32, no. 1, pp. 496–508, 2021.

[27] H. Wijshoff, "The dynamics of the piezo inkjet printhead operation," *Phys. Rep.*, vol. 491, no. 4–5, pp. 77–177, 2010.

[28] J. C. Miers and W. Zhou, "Inkjet Printing at Megahertz Frequency," 2015.

[29] M. Chopra, L. Li, H. Hu, M. A. Burns, and R. G. Larson, "DNA molecular configurations in an evaporating droplet near a glass surface," *J. Rheol. (N. Y. N. Y).*, vol. 47, no. 5, pp. 1111–1132, 2003.

[30] W. Wang, J. Lin, and D. C. Schwartz, “Scanning force microscopy of DNA molecules elongated by convective fluid flow in an evaporating droplet,” *Biophys. J.*, vol. 75, no. 1, pp. 513–520, 1998.

[31] B. De Gans, P. C. Duineveld, and U. S. Schubert, “Inkjet printing of polymers: state of the art and future developments,” *Adv. Mater.*, vol. 16, no. 3, pp. 203–213, 2004.

[32] T. Kawase, H. Sirringhaus, R. H. Friend, and T. Shimoda, “Inkjet printed via-hole interconnections and resistors for all-polymer transistor circuits,” *Adv. Mater.*, vol. 13, no. 21, pp. 1601–1605, 2001.

[33] A. Abd El-Rahman, E. Saad, C. Aydemir, S. A. Özsoy, and S. Yenidoğan, “Drying methods of the printing inks,” *J. Graph. Eng. Des.*, vol. 12, no. 2, p. 29, 2021.

[34] G. Grau, R. Kitsomboonloha, S. L. Swisher, H. Kang, and V. Subramanian, “Printed transistors on paper: Towards smart consumer product packaging,” *Adv. Funct. Mater.*, vol. 24, no. 32, pp. 5067–5074, 2014.

[35] Y. Dong, B. Wang, H. Ji, W. Zhu, Z. Long, and C. Dong, “Effect of papermaking conditions on the ink absorption and overprint accuracy of paper,” *BioResources*, vol. 15, no. 1, pp.

1397–1406, 2020.

[36] H. Zheng, S. Gao, K. Ngo, and G. Q. Lu, "'Processing and Properties of Chip-bonding on Copper by Low-temperature Sintering a Nanosilver Paste,'" *CIPS 2016 - 9th Int. Conf. Integr. Power Electron. Syst.*, no. February, 2019.

[37] K. S. Bhat, R. Ahmad, Y. Wang, and Y.-B. Hahn, "Low-temperature sintering of highly conductive silver ink for flexible electronics," *J. Mater. Chem. C*, vol. 4, no. 36, pp. 8522–8527, 2016.

[38] C.-T. Chen, "Inkjet Printing of Microcomponents: Theory, Design, Characteristics and Applications," *Featur. Liq. Cryst. Disp. Mater. Process.*, 2011.

[39] C.-T. Chen, "Inkjet printing of microcomponents: theory, design, characteristics and applications," in *Features of liquid crystal display materials and processes*, IntechOpen, 2011.

[40] M. P. Howard, A. Nikoubashman, and A. Z. Panagiotopoulos, "Stratification in drying polymer–polymer and colloid–polymer mixtures," *Langmuir*, vol. 33, no. 42, pp. 11390–11398, 2017.

[41] C. Bourges-Monnier and M. E. R. Shanahan, “Influence of evaporation on contact angle,” *Langmuir*, vol. 11, no. 7, pp. 2820–2829, 1995.

[42] R. D. Deegan, O. Bakajin, T. F. Dupont, G. Huber, S. R. Nagel, and T. A. Witten, “Capillary flow as the cause of ring stains from dried liquid drops,” *Nature*, vol. 389, no. 6653, pp. 827–829, 1997.

[43] E. Adachi, A. S. Dimitrov, and K. Nagayama, “Stripe patterns formed on a glass surface during droplet evaporation,” *Langmuir*, vol. 11, no. 4, pp. 1057–1060, 1995.

[44] L. Janßen and U. Jung, “Influence of drying conditions on the uniformity of inkjet printed structures,” in *European Coating Symposium*, 2015, p. 77.

[45] P. J. Yunker, T. Still, M. A. Lohr, and A. G. Yodh, “Suppression of the coffee-ring effect by shape-dependent capillary interactions,” *Nature*, vol. 476, no. 7360, pp. 308–311, 2011.

[46] J. Park and J. Moon, “Control of colloidal particle deposit patterns within picoliter droplets ejected by ink-jet printing,” *Langmuir*, vol. 22, no. 8, pp. 3506–3513, 2006.

[47] S. Magdassi, *The chemistry of inkjet inks*. World scientific, 2009.

[48] D. Brutin, *Droplet wetting and evaporation: from pure to complex fluids*. Academic Press, 2015.

[49] L. Janssen and U. Jung, "Influencing the profile of an inkjet printed layer on glass by using optimized solvent mixtures," *Int. Circ. Graph. Educ. Res.*, no. 10, pp. 27–33, 2017.

[50] E. Sowade, H. Kang, K. Y. Mitra, O. J. Weiß, J. Weber, and R. R. Baumann, "Correction: Roll-to-roll infrared (IR) drying and sintering of an inkjet-printed silver nanoparticle ink within 1 second," *J. Mater. Chem. C*, vol. 3, no. 45, p. 11974, 2015.

[51] A. Denneulin, A. Blayo, C. Neuman, and J. Bras, "Infra-red assisted sintering of inkjet printed silver tracks on paper substrates," *J. Nanoparticle Res.*, vol. 13, no. 9, pp. 3815–3823, 2011.

[52] M. C. Lopes, E. Bonaccurso, T. Gambaryan-Roisman, and P. Stephan, "Influence of the substrate thermal properties on sessile droplet evaporation: Effect of transient heat transport," *Colloids Surfaces A Physicochem. Eng. Asp.*, vol. 432, pp. 64–70, 2013.

[53] R. G. Picknett and R. Bexon, "The evaporation of sessile or pendant drops in still air," *J. Colloid Interface Sci.*, vol. 61, no. 2, pp. 336–350, 1977.

[54] M. A. Saada, S. Chikh, and L. Tadrist, “Evaporation of a sessile drop with pinned or receding contact line on a substrate with different thermophysical properties,” *Int. J. Heat Mass Transf.*, vol. 58, no. 1–2, pp. 197–208, 2013.

[55] G. Strotos, M. Gavaises, A. Theodorakakos, and G. Bergeles, “Numerical investigation on the evaporation of droplets depositing on heated surfaces at low Weber numbers,” *Int. J. Heat Mass Transf.*, vol. 51, no. 7–8, pp. 1516–1529, 2008.

[56] E. Bormashenko, A. Musin, and M. Zinigrad, “Evaporation of droplets on strongly and weakly pinning surfaces and dynamics of the triple line,” *Colloids Surfaces A Physicochem. Eng. Asp.*, vol. 385, no. 1–3, pp. 235–240, 2011.

[57] D. Orejon, K. Sefiane, and M. E. R. Shanahan, “Stick–slip of evaporating droplets: substrate hydrophobicity and nanoparticle concentration,” *Langmuir*, vol. 27, no. 21, pp. 12834–12843, 2011.

[58] M. E. R. Shanahan, “Simple theory of" stick-slip" wetting hysteresis,” *Langmuir*, vol. 11, no. 3, pp. 1041–1043, 1995.

[59] D. Khilifi, W. Foudhil, K. Fahem, S. Harmand, and J. S. Ben, “Study of the phenomenon

of the interaction between sessile drops during evaporation," *Therm. Sci.*, vol. 23, no. 2 Part B, pp. 1105–1114, 2019.

[60] A. Apostolakis *et al.*, "Resistivity study of inkjet-printed structures and electrical interfacing on flexible substrates," *Micro Nano Eng.*, vol. 15, p. 100129, 2022.

[61] G. Xiao, Z. Zhang, H. Fukutani, Y. Tao, and S. Lang, "Improving the ${Q} $-Factor of Printed HF RFID Loop Antennas on Flexible Substrates by Condensing the Microstructures of Conductors," *IEEE J. Radio Freq. Identif.*, vol. 2, no. 2, pp. 111–116, 2018.

[62] Y. Sui and C. A. Zorman, "Inkjet printing of metal structures for electrochemical sensor applications," *J. Electrochem. Soc.*, vol. 167, no. 3, p. 37571, 2020.

[63] J. Mendel and D. Bugner, "Particle generation and ink particle size effects in pigmented inkjet inks–Part I," *J. Nanoparticle Res.*, vol. 1, p. 419, 1999.

[64] S. K. Sarkar, H. Gupta, and D. Gupta, "Flash Light Sintering of Silver Nanoink for Inkjet-Printed Thin-Film Transistor on Flexible Substrate," *IEEE Trans. Nanotechnol.*, vol. 16, no. 3, pp. 375–382, 2017.

[65] D. Mitra, K. Y. Mitra, V. Dzhagan, N. Pillai, D. R. T. Zahn, and R. R. Baumann, "Work

function and conductivity of inkjet-printed silver layers: Effect of inks and post-treatments," *J. Electron. Mater.*, vol. 47, no. 3, pp. 2135–2142, 2018.

[66] J. Niittynen, R. Abbel, M. Mäntysalo, J. Perelaer, U. S. Schubert, and D. Lupo, "Alternative sintering methods compared to conventional thermal sintering for inkjet printed silver nanoparticle ink," *Thin Solid Films*, vol. 556, pp. 452–459, 2014.

[67] Y. Galagan *et al.*, "Photonic sintering of inkjet printed current collecting grids for organic solar cell applications," *Org. Electron.*, vol. 14, no. 1, pp. 38–46, 2013.

[68] W.-H. Chung, H.-J. Hwang, S.-H. Lee, and H.-S. Kim, "In situ monitoring of a flash light sintering process using silver nano-ink for producing flexible electronics," *Nanotechnology*, vol. 24, no. 3, p. 35202, 2012.

[69] Y.-R. Jang, C.-H. Ryu, Y.-T. Hwang, and H.-S. Kim, "Optimization of intense pulsed light sintering considering dimensions of printed Cu nano/micro-paste patterns for printed electronics," *Int. J. Precis. Eng. Manuf. Technol.*, pp. 1–15, 2020.

[70] J. Kwon *et al.*, "Low-temperature oxidation-free selective laser sintering of Cu nanoparticle paste on a polymer substrate for the flexible touch panel applications," *ACS Appl. Mater.*

Interfaces, vol. 8, no. 18, pp. 11575–11582, 2016.

[71] Y. Son *et al.*, "Nanoscale electronics: digital fabrication by direct femtosecond laser processing of metal nanoparticles," *Adv. Mater.*, vol. 23, no. 28, pp. 3176–3181, 2011.

[72] J. Noh and D. Kim, "Femtosecond laser sintering of silver nanoparticles for conductive thin-film fabrication," *Appl. Phys. A*, vol. 126, no. 2, pp. 1–7, 2020.

[73] S. Liu, M. C. Yuen, and R. Kramer-Bottiglio, "Reconfigurable electronic devices enabled by laser-sintered liquid metal nanoparticles," *Flex. Print. Electron.*, vol. 4, no. 1, p. 15004, 2019.

[74] Y. Bougdid, F. Chenard, J. Sugrim, R. Kumar, and A. Kar, "CO2 laser-assisted sintering of TiO2 nanoparticles for transparent films," *J. Laser Appl.*, vol. 35, no. 1, 2023.

[75] J. F. Mousumi, T. Li, G. Kulkarni, A. Kar, R. Kumar, and K. O. Davis, "Localized laser printing and sintering of silver nanoparticles for silicon solar cell metallization," in *2021 IEEE 48th Photovoltaic Specialists Conference (PVSC)*, 2021, pp. 2544–2546.

[76] M. Reveil, V. C. Sorg, E. R. Cheng, T. Ezzyat, P. Clancy, and M. O. Thompson, "Finite element and analytical solutions for van der Pauw and four-point probe correction factors

when multiple non-ideal measurement conditions coexist," *Rev. Sci. Instrum.*, vol. 88, no. 9, p. 94704, 2017.

[77] M. S. Rahman, M. Shahzadeh, M. Rahman, S. Pisana, and G. Grau, "High-speed contactless sintering characterization for printed electronics by frequency-domain thermoreflectance," *Flex. Print. Electron.*, vol. 5, no. 3, p. 35006, 2020.

[78] M. S. Rahman, M. Rahman, S. Pisana, and G. Grau, "Effect of sintering conditions on the thermal properties of printable metal nanoparticle ink studied by thermoreflectance," in *Nanoengineering: Fabrication, Properties, Optics, Thin Films, and Devices XVI*, 2019, vol. 11089, p. 110890U.

[79] J. H. Choi, K. Ryu, K. Park, and S.-J. Moon, "Thermal conductivity estimation of inkjet-printed silver nanoparticle ink during continuous wave laser sintering," *Int. J. Heat Mass Transf.*, vol. 85, pp. 904–909, 2015.

[80] D. Kim, I. Lee, Y. Yoo, Y.-J. Moon, and S.-J. Moon, "Transient variation of a cross-sectional area of inkjet-printed silver nanoparticle ink during furnace sintering," *Appl. Surf. Sci.*, vol. 305, pp. 453–458, 2014.

[81] M. Rahman, M. Shahzadeh, P. Braeuninger-Weimer, S. Hofmann, O. Hellwig, and S. Pisana, “Measuring the thermal properties of anisotropic materials using beam-offset frequency domain thermoreflectance,” *J. Appl. Phys.*, vol. 123, no. 24, p. 245110, 2018.

[82] M. Ghalamboran, M. Nazeri, and G. Grau, “Pattern-dependent resistivity variations in inkjet-printed conductors due to non-uniform ink drying,” *Flex. Print. Electron.*, 2024.